N64 33176

FINAL AND SUMMARY REPORT

DEVELOPMENT OF IMPROVED THERMOELECTRIC MATERIALS FOR SPACECRAFT APPLICATIONS

CONTRACT NO. NAS8-11075
TP3 - 85484 (IF)
CPB-02-1525-63

for the period

Apr. 29, 1964 to July 29, 1964

to

George C. Marshall Space Flight Center
National Aeronautics and Space Administration
Huntsville, Alabama

by

Tecumseh Products Company
Ohio Semiconductors Division
1205 Chesapeake Avenue
Columbus, Ohio 43212

(Report Prepared by A. E. Middleton)

Contributors to Report A. E. Middleton
F. J. Celli
J. W. Harpster
F. N. Lancia
J. R. Chabria

FOREWORD

This report was prepared by Ohio Semiconductors Division of Tecumseh Products Company, Columbus, Ohio to meet the requirements for the FINAL SUMMARY REPORT on NASA Contract NAS8-11075 administered by George C. Marshall Space Flight Center, Huntsville, Alabama. Ray Gause is Project Engineer for NASA.

The work was administered by W. E. Bulman, Vice President, Tecumseh Products Company. Technical direction, planning, coordination and theory were provided by A. E. Middleton, Chief Scientist. Chief technical and professional contributors to the effort and their fields of performance were F. J. Celli, and J. R. Chabria, Material Research, and J. W. Harpster and F. N. Lancia, Materials Evaluation Research. The technicians who contributed were J. Sanborn, J. Bosley, R. Jackson and G. Minton.

SUMMARY

Accomplishments during this year of project effort include:

1. A detailed identification of the nature of the problems faced in improving Z_p beyond that achieved in present day production and laboratory materials. This effort culminated in proposing the interdisciplinary molecular well model for high Z materials which provides the materials developer with an atomic model for high Z materials which is correlated with band structure and transport theory.

2. Development of suitable wide temperature range evaluation facilities to give Z_p, S, k_T, σ, R_H, and μ as a function of temperature over the range from 78°K to 560°K, for experimental materials.

3. Preparation and evaluation of BiSb alloy crystals and $AgSbTe_2$ alloys nearly representative of the state-of-the-art for thermoelectric cooling, and Bi crystals nearly representative of the state-of-the-art for thermomagnetic cooling.

4. Initiation of alloy modification studies in the $AgSbTe_2$ alloy system using the selection principles evolved in the interdisciplinary identification studies. These investigations included preparation and evaluation of alloys representing Tl, Au and Fe substitutions in the $AgSbTe_x$ system and specific studies of $AgSbTe_2$, $TlSbTe_2$, Sb_2Te_3, Tl substitution for Bi in the p type OSD standard Bi_2Te_3 alloy, $Au_xSb_4BiTe_{7.5}$ (where x = 0 to 1), TlBiTe and $AgFeTe_2$. $TlSbTe_2$ with approximately a C_{33} type structure was made and two effects associated with Tl in the D^5_{3d}-$R\bar{3}m$ structure were discovered, namely, its contribution via empty p orbitals to hole states in the valence band at low temperature and introduction of ionized impurity centers at higher temperatures via s orbital excitation. The interdisciplinary molecular well model was applied in explaining the thermoelectric characteristics of several of these alloys.

Although a new higher Z thermoelectric cooling material has not been revealed in this period, major and vital steps toward this objective are represented by the above accomplishments.

ABSTRACT

The status of thermoelectric and thermomagnetic cooling development is reviewed and the highest Z thermoelectric extrinsic semiconductors and intrinsic semimetals covering the range from 573°K to 50°K are identified chemically, structurally and thermoelectrically.

The nature of the interdisciplinary difficulties plaguing the prediction of new and higher Z thermoelectric materials are critically, theoretically, and analytically assessed.

A method is outlined for obtaining a detailed interdisciplinary characterization of high Z thermoelectric materials, which can reveal chemical and structural situations for which high Z can be obtained. Factors controlling the value of Z as revealed by considerations of band and transport theory, structural analysis, chemical bonding theory and principles, and relationships between charge transport parameters and chemical correlation parameters for a large number of chemical compounds and elements, are specifically identified.

Based on the results ofthese introspective analyses and a specific consideration of the crystal structure, chemical bonding, band structure generation and determination for Bi_2Te_3, an interdisciplinary molecular well model, believed to have far reaching significance in future thermoelectric material development, was developed. This model provides a connecting link between chemical bonding and band structure for high Z materials and reveals the structural and chemical factors which are required to achieve band structure and charge and phonon transport characteristics which are necessary for high Z. Approximate formulae for expressing the thermoelectric properties, which determine Z, are presented and applied to the case of Bi_2Te_3 alloys. Results of these calculations are self consistent. The band structure predictions of the model compare favorable with band structure information obtained by galvanomagnetic coefficient analyses on Bi_2Te_3.

Methods of preparing high Z thermoelectric and thermomagnetic materials are discussed and the methods used to prepare single crystal Bi and Bi alloys and polycrystalline materials in the $AgSbTe_2$ and Bi_2Te_3 alloy systems are described.

Equipment, techniques and methods for evaluating Z_p, S, k_T, σ, R_H, and μ over the temperature range of interest are described.

Efforts to reproduce the state-of-the-art type of thermoelectric BiSb crystals, and $AgSbTe_2$ alloys and thermomagnetic Bi crystals are discussed, and extensive thermoelectric and transport property evaluations of these materials are presented. A brief summary of thermoelectric properties vs. temperature of standard OSD n and p type alloys is provided. Also, a brief summary of preliminary work on thermomagnetic cooling using Bi crystals is given.

Research efforts on alloy modifications of D^5_{3d}-$R\bar{3}m$ or related structures, inclusive of studies of $AgSbTe_2$, $TlSbTe_2$, Tl in standard p type Bi_2Te_3 alloy, Au in $AgSbTe_2$ and $Sb_4BiTe_{7.5}$, Fe in $AgSbTe_2$, and TlBiTe, are summarized and discussed in terms of the interdisciplinary molecular well model. $TlSbTe_2$ with approximately a C_{33}, D^5_{3d}-$R\bar{3}m$ structure was made.

Two new effects, characteristic of Tl in D^5_{3d}-$R\bar{3}m$ C_{33} structure, were discovered. These were generation of hole states in the valence bands via missing p orbital bonds and ionized impurity production via excitation of non bonding s orbitals to p orbital states in the valence band.

In general, the use of the interdisciplinary molecular well model has allowed considerable clarification in regard to possibilities of developing improved Z materials.

LIST OF TABLES

LIST OF FIGURES

FIGURE 14 Relationship of charge carrier mobility to electronegativity difference for Group IV elements and III-V and II-VI compounds.

FIGURE 15 Relationship of charge carrier mobility to electronegativity difference for other compounds.

FIGURE 16 Relationship of principal quantum number, $\bar{n}$, to electronegativity, ΔX, for structures with cubic close-packed anion substructures and tetrahedral and octahedral coordination (after Mooser[28]).

FIGURE 17 Relationship between work function of elements and their electronegativity.

FIGURE 18 Relationship of ionicity parameter, λ, and ΔX, for many compounds with different bond schemes.

FIGURE 19 Relationship of ionicity parameter, λ, and mean atomic weight for many compounds with different bond schemes.

FIGURE 20 Dependence of electron mobility on the polarity parameter, $\frac{e^*}{c}$ for elements and compounds with several types of bond schemes.

FIGURE 21 Dependence of the lattice thermal conductivity on the polarity parameter, $\frac{e^*}{c}$, for elements and compounds with various bond schemes.

FIGURE 22 Dependence of effective mass ratio, $\frac{m_l}{m}$, on the polarity parameter, $\frac{e^*}{c}$, for compounds and elements with various bond schemes.

FIGURE 23 Variation of $\frac{\mu_a}{k_{ph}}$ with the polarity parameter for compounds and elements representing various bond schemes.

FIGURE 24 Relationship between energy gap, E_g, and mean atomic weights for Group IV elements and Group III-V, and II-VI Compounds.

FIGURE 25 E_g vs mean atomic weight for other compounds and elements.

FIGURE 52 Resistivity ratio, $\rho_{33}(H)/\rho_{33}(o)$, versus magnetic field at 80°K for OSD $Bi_{(94)}Sb_{(6)}$ and Bi compared to Lockheed Group's[40] $Bi_{97}Sb_3$, $Bi_{95}Sb_5$, and $Bi_{88}Sb_{12}$ crystals.

FIGURE 53 Comparison of literature data and OSD alloy data on resistivity, ρ, relative resistivity, $\rho_{33}(H)/\rho_{33}(o)$ and Hall coefficient (80°K and 300°K) versus antimony content for $Bi_{1-x}Sb_x$ alloy crystals.

FIGURE 54 Z_p, S, k_T, and σ vs temperature for OSD standard n and p type Bi_2Te_3 alloys.

FIGURE 55 Z_p, S, k_T, and σ vs temperature for OSD $AgSbTe_2$.

FIGURE 56 Comparison of Z_p values vs temperature for OSD $Bi_{94}Sb_6$ crystals (zero H field), n and p type Bi_2Te_3 alloys, and $AgSbTe_2$ with maximum Z_p values revealed in the literature for $Bi_{88}Sb_{12}$ crystals, n and p type Bi_2Te_3 alloys, $(AgSbTe_2)_{0.4}(PbTe)_{0.2}$ and p type PbTe alloys.

FIGURE 57 Relation between ordered $AgSbTe_2$ rhombohedral (idealized) and cubic lattice of the disordered NaCl structure.

FIGURE 58 Pictorial representation of a possible molecular net structure for $AgSbTe_2$ crystals.

FIGURE 59 R_H vs $\frac{1}{T}$ for $AgSbTe_2$, $AgFeTe_2$ and TlBiTe compared to OSD standard n type Bi_2Te_3 alloy.

FIGURE 60 σ vs $\frac{1}{T}$ for $AgSbTe_2$, $AgFeTe_2$ and TlBiTe compared to OSD standard n type Bi_2Te_3 alloy.

FIGURE 61 μ vs T for $AgSbTe_2$, $AgFeTe_2$, and TlBiTe compared to OSD standard n type Bi_2Te_3 alloy.

FIGURE 62 Z_p, S, k_T and ρ vs temperature for $AgSbTe_2$ compared to standard p type Bi_2Te_3 alloy.

FIGURE 63 R_H vs $\frac{1}{T}$ for $TlSbTe_2$, Tl in place of Bi in p type Bi_2Te_3 standard alloy, Sb_2Te_3, and $AuSb_4BiTe_{7.5}$ compared to OSD standard p type Bi_2Te_3 alloy.

FIGURE 64 σ vs $\frac{1}{T}$ for $TlSbTe_2$, Tl in place of Bi in p type Bi_2Te_3 standard alloy, Sb_2Te_3, and $AuSb_4BiTe_{7.5}$ compared to OSD standard p type Bi_2Te_3 alloy.

FIGURE 65 μ vs T for $TlSbTe_2$, Tl in place of Bi in p type Bi_2Te_3 standard alloy, Sb_2Te_3, and $AuSb_4BiTe_{7.5}$ compared to OSD standard p type Bi_2Te_3 alloy.

FIGURE 66 Z_p, S, k_T and ρ vs temperature for $TlSbTe_2$ compared to OSD standard p type Bi_2Te_3 alloy.

FIGURE 67 Z_p, S, k_T, and ρ vs temperature for Tl substitution for Bi in p type Bi_2Te_3 standard alloy compared to p type standard Bi_2Te_3 alloy.

FIGURE 68 Z_p, S, k_T, and ρ vs temperature for Sb_2Te_3 compared to standard p type Bi_2Te_3 alloy.

FIGURE 69 Z_p, S, k_T and ρ vs temperature for $AuSb_4BiTe_{7.5}$ compared to standard p type Bi_2Te_3 alloy.

FIGURE 70 Z_p, S, k_T, and ρ vs temperature for $AgFeTe_2$ compared to standard n type Bi_2Te_3 alloy.

TABLE OF CONTENTS

PURPOSE

Thermoelectric cooling has merit for space application as a means of transferring heat from one point to another in a space vehicle. However thermoelectric cooling materials and devices for this purpose must be available which will perform over a wide range of ambient temperature and pressures. Available thermoelectric and thermomagnetic materials do not meet the temperature range or maximum figure-of-merit requirements. In addition, it appears likely that their stability under low ambient pressures encountered in space may be unsatisfactory.

Specifically, it is expected that thermoelectric and thermomagnetic materials with figures-of-merit greater than $4 \times 10^{-3}/^{\circ}C$ at $25^{\circ}C$ will be required for continuous operation at ambient temperatures from $-250^{\circ}C$ to $+300^{\circ}C$ under environmental pressures as low as 1×10^{-8} mm Hg.

OBJECTIVES

The objectives of this project are to:

1). theoretically and analytically evaluate the possibilities of developing thermoelectric and thermomagnetic cooling materials and devices which will meet the above general specifications.

2). make and evaluate any materials which show potential promise of meeting the basic requirements for high figure-of-merit and environmental stability.

3). design and fabricate exemplary modules containing any materials which pass evaluation tests.

INTRODUCTORY INFORMATION ON THE PRESENT STATUS OF THERMOELECTRIC AND THERMOMAGNETIC COOLING

The present state of development of thermoelectric and thermomagnetic cooling hardware directly reflects the figures-of-merit which characterize the available thermoelectric materials.

For thermoelectric coolers the figure-of-merit is given by:

$$Z_p = \frac{S^2}{k\rho} \qquad 1)$$

where

Z = Peltier-Seebeck Figure-of-Merit $(^{\circ}C)^{-1}$ in the direction parallel to current flow

S = Thermoelectric power in $\mu V/^{\circ}C$

k = Thermal conductivity in watts/cm $^{\circ}C$

ρ = electrical resistivity in ohm-cms

For thermomagnetic coolers, the figure-of-merit is given by:

$$Z_{xy} = \frac{S_{xy}^2}{k_y \rho_x(B_z)} \qquad 2)$$

where

Z_{xy} = Nernst-Ettingshausen Figure-of-Merit $(^{\circ}C)^{-1}$

S_{xy} = the thermoelectric power in $\mu V/^{\circ}C$ developed in the y direction by current flowing in the x direction

k_y = the thermal conductivity in y direction

$\rho_x(B_z)$ = the resistivity in the x direction as a result of application of a magnetic field B in the z direction

A thermoelectric cooling couple consists of an n-type and a p-type leg, each leg of which has a figure-of-merit, Z_p, defined as above. The n-type has a negative and the p-type positive thermoelectric power. If we assume that both legs have equal S, k, and ρ values, we only need to consider the figure-of-merit of one, since under these conditions, the figure-of-merit of the couple is the same as that of a single leg. In contrast, a thermomagnetic cooling element consists of one shaped crystal which conducts almost equally by electrons and holes.

Z_p is related to ΔT_{max} for thermoelectric coolers by the relationship:

$$\Delta T_{max} = \frac{1}{2} Z_p T_c^2 \qquad 3)$$

where

T_c = temperature of cold junction

The ΔT_{max} achieved for $T_h = 303^{\circ}K$ is 74° to $80^{\circ}C$ using p and n type bismuth telluride alloys with maximum Z_p values at room temperature of approximately $3 \times 10^{-3}/^{\circ}C$. Under these conditions the minimum cold junction temperature is $\sim 225^{\circ}K$. At $T_h = 373^{\circ}K$; $T_c \cong 290^{\circ}K$. When T_h is held at a temperature about $450^{\circ}K$, the ΔT_{max} shows a marked decrease.

Using a p-type bismuth telluride alloy with an n-type bismuth antimony alloy, Wolfe[1] has reported that cooling modules with higher Z values between $225^{\circ}K$ and $100^{\circ}K$ can be made, than by coupling of p and n-type bismuth telluride alloys.

Thermoelectric coolers can be cascaded. A cascade cooler involving seven stages was constructed from bismuth telluride alloys by Beosen [2]. With T_h = 298°K, a ΔT_{max} of 142°C was obtained giving T_c = 156°K. By setting the hot junction at 373°K, it is expected that ΔT_{max} of such a cooler could exceed 150°C.

Z_{xy} or Z_{NE} is related to ΔT_{max} for thermomagnetic coolers by:

$$\Delta T_{max_{NE}} = \frac{1}{2} Z_{xy} T_h^2 \quad 4)$$

where

T_h is the base or hot side temperature

Such coolers have been built using oriented Bi crystals and $Bi_{97}Sb_3$ alloy crystals. Kooi and coworkers [3] demonstrated a ΔT_{max} of 62°C for T_h = 195°K and B = 30 Kg using a 5 to 1 ratio shaped cooler, thus giving a T_c of 133°K. More recently Harman and Honig et al [4] demonstrated a ΔT_{max} of 101°C for $T_h \cong$ 302°K and B = 110 Kg and a current of 55 amperes, thus giving a T_c = 201° K.

A hybrid Peltier-Ettingshausen cooler was very recently designed by Madigan [5] using a Peltier cascade as a variable temperature heat sink for a shaped Ettingshausen cooler. With T_h of the Peltier cascade at 300°K, T_c of the Peltier unit will be 190°K. Using a shaped $Bi_{97}Sb_3$ Ettingshausen cooler with I = 7: 6 amps and B = 8 Kg, he has designed to obtain a ΔT_{max} of 43°C with T_h at 190°K, giving a T_c of 147°K.

Whereas Peltier cascade coolers require stacking of modules, the Ettingshausen cooler can be cascaded by shaping one element. A major disadvantage of the Ettingshausen cooler may be the excessively high value of magnetic field required to operate it at higher temperatures than 200°K.

THERMOELECTRIC AND THERMOMAGNETIC COOLING MATERIALS STATE-OF-THE-ART

During the last sixteen years much effort [6-9] has been expended in developing p and n-type extrinsic semiconducting materials with high Figures-of-Merit in the range from room temperature and up. The Bismuth telluride alloys have been developed since 1954 [7] to their presently optimized Z_p level of ~3 x 10^{-3}/°C at room temperature (See Figure 1).

Attempts to find extrinsic semiconductors which show higher Z_{max} values at temperatures much below room temperatures have been unsuccessful in the past. Recently Smith and Wolfe [10] found that intrinsic anisotropically conducting Bi-Sb alloy semimetal crystals will exhibit Z_{Pmax} values at 90°K as high as 6x10^{-3}/°C without magnetic field and at 100°K as high as 8.6x10^{-3}/°C in a 1700 gauss magnetic field applied || to the bisectrix axis with current || to the trigonal axis. Only n-type Bi alloys with these striking properties have been developed. The approximate temperature dependency of Z_p for $Bi_{88}Sb_{12}$ alloys is shown in Figure 1.

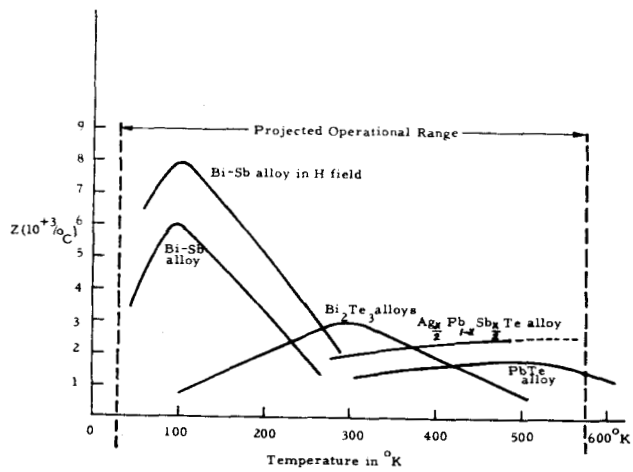

Fig. 1. Comparison of the variation in Z_p with temperature for thermoelectric materials with optimized Z_p at one temperature.

In the highest temperature range (up to 600°K), beyond the 150 to 200°K limit of bismuth telluride alloys, the n and p-type PbTe alloys, [6] well known in the thermoelectric power generation field, have shown the highest Z_p values (See Figure 1) until the discovery of $AgSbTe_2$ in 1958 by Wernick et al [11]. Although $AgSbTe_2$ is not satisfactory by itself, a p-type alloy, $Ag_{.4}Pb_{.2}Sb_{.4}Te$, was shown by Fleischmann [12] to exhibit a Z_p value up to near 3 x 10^{-3}/°C at 500-600°K. An n-type alloy with Z_p of this value in this temperature range is not known.

PRELIMINARY IDENTIFICATION OF HIGH Z THERMOELECTRIC AND THERMOMAGNETIC COOLING MATERIALS

It is helpful to characterize the highest Z thermoelectric materials before a detailed analysis of the problem of developing higher Z thermoelectric materials is considered.

In Table 1 are listed the compositions by chemical formula of the highest Z thermoelectric and thermomagnetic materials along with other information.

TABLE 1

PRELIMINARY IDENTIFICATION OF BEST THERMOELECTRIC AND THERMOMAGNETIC COOLING MATERIALS FOR -250°C to +300°C TEMPERATURE RANGE

Material System	Useful Form of Material	Melting Point Range °C	Comments
Thermoelectric			
Bi_xSb_y alloys with x=97-88 y= 3-12	Single crystal; oriented with current parallel to trigonal axis	271-350	Intrinsic semimetal with energy gap of up to ~.02 ev at R.T.; crystal orientation and purity very important; n-type conduction predominates due to $\frac{\sigma_e}{\sigma_p} \cong 10$
Bi-Te compounds alloyed with Se and Sb-Te compounds plus other minor constituents	Cast and oriented; powder pressed and sintered is relatively poorer but useful	550-600°C	Extrinsic semiconductor; orientation is of some importance; both p and n-type second phase is often present and is tolerable and sometimes desirable. Eg~.2-.3 ev
$AgSbTe_x$ alloyed with PbTe	Cast and zone leveled alloys	575-625	Extrinsic semiconductors; always p-type in research samples made to date; tends to have a second phase in cast alloys which causes analytical problems. Eg~.6 ev
Thermomagnetic			
Bi_xSb_y alloys with x=99-96 y=1-4	Single crystal oriented with current parallel to trigonal axis and B parallel to bisectrix axis	271-290	Intrinsic semimetal energy band overlap of ~.007 ev; n-type conduction slightly predominant

Those with highest Z_{max}, namely, Bi alloy semimetals, have the lowest melting points, ~300°C, while the bismuth telluride and silver antimony telluride alloys have melting points near 600°C.

TABLE 2

MAINLY CHEMICAL IDENTIFICATIONS OF BEST THERMOELECTRIC AND THERMOMAGNETIC COOLING ALLOYS

	Bonding	Lattice Spacing	Ionicity $\frac{e^*}{c}$	Atomic Ionicity λ_o	Electronegativity Difference ΔX	Mean At Wt	Diel Const
Thermoelectric (Seebeck-Peltier)							
$Bi_{88}Sb_{12}$	p orbital 1/2 bond and resonance bond	anisotropic along trigonal axis	0	~0	~0	200	~100
$Bi_{95}Sb_5$	"	"	0	~0	~0	205	~100
Bi_2Te_3-Bi_2Se_3 alloy	"	"	~0	~.2	.2	~155	~80
Bi_2Te_3-Sb_2Te_3 Sb_2Se_3 alloy	"	"	~0	~.2	.2	~150	~80
$Ag_{\frac{x}{2}}Pb_{1-x}Sb_{\frac{x}{2}}Te$	p orbital 1/2 bond + S 1/2 bond + resonance bond	"	~0	~.5	.2	135	--
Thermomagnetic (Nernst-Ettingshausen)							
Bi	p orbital 1/2 bond + resonance bond	"	0	0	0	209	100
$Bi_{97}Sb_3$	"	"	0	~0	~0	206	~100

As shown in Tables 1 and 2, Bi and Bi alloys must be used in single crystal form with the current parallel to the trigonal axis. They are intrinsic semimetals and have a very small energy gap or overlap, exhibit anisotropic lattice spacing in the direction $\parallel$ to the trigonal axis, and show predominately electronic conduction in this direction because of a rather large anisotropy of $\frac{\sigma_e}{\sigma_p} \cong 10$ (σ_e, electron conductivity and σ_p, hole conductivity).[3] In addition, they are chemically bonded by both p-orbital covalent half bonds and resonance bonds. The Bi and Sb of the alloys are characterized by a very small electronegativity difference. The alloys cleave readily in a plane $\perp$ to their trigonal axis.

The bismuth telluride alloys are used in polycrystalline form. The thermoelectric properties of the n-type alloys are sensitive to orientation of the crystals in the extrinsic range[13]. Both the electrical conductivity and thermal conductivity are anisotropic, the larger values being observed perpendicular to the trigonal axis. These alloys also have anisotropic lattice spacings in the direction of the trigonal axis and cleave readily in a plane $\perp$ to the trigonal axis. They are p-orbital bonded and resonance bonded and have a distinct molecular net type of structure with five atoms in a molecule. The electronegativity difference between the major atom constituents of the alloys is small, 0.2, and the calculated ionicity, $\frac{e^*}{c}$, is approximately zero. Their dielectric constants are large (~ 80). They are extrinsic semiconductors with a small apparent energy gap ranging from 0.16-0.3 ev.

Not as much can be said about the silver antimony telluride alloy because of its complex nature. It does show anisotropy of lattice spacings. It is p-orbital bonded and s-orbital bonded and exhibits resonance bonding tendencies. The electronegativity difference of its constituent atoms is low (~ 0.2), its atomic ionicity, 0.5, and its polar ionicity $\frac{e^*}{c} \cong 0$. However its alloying material, PbTe, is p-orbital-resonance bonded, has a high dielectric constant, shows slight anisotropy of lattice spacing and has large piezoresistance.

As shown in Table 3, all these materials have rhombohedral lattices except the silver antimony telluride allloy which is cubic with rhombohedral tendencies. They all belong to the D^5_{3d}-$R\bar{3}m$ space group except the silver antimony telluride alloy which is apparently a mixture of O^5_h-$Fm3m$ and D^5_{3d}-$R\bar{3}m$.

In Table 3, the sign of the thermoelectric power, conductivity type, Z_{max}, and the Z_{max} temperature are given.

The above identifications can be noted to be comprehensive and interdisciplinary.

TABLE 3

STRUCTURAL NATURE OF BEST KNOWN CANDIDATES FOR THERMOELECTRIC AND THERMOMAGNETIC COOLING MATERIALS FOR WIDE TEMPERATURE RANGING OF ENVIRONMENT

Material	"Strukturbericht" Structure Type	Lattice Type	Space Group	Conductivity Type	S Type Values	Z_{max} at $T^{\circ}K$
Thermoelectric (Seebeck-Peltier)						
$Bi_{88}Sb_{12}$	A_7	Rhombohedral	D^5_{3d}-$R\bar{3}m$	n-type; Neg. intrinsic; Large $\frac{\mu_e}{\mu_p}$	6×10^{-3}	$80^{\circ}K$
					8.6×10^{-1}	$80^{\circ}K$
$Bi_{95}Sb_5$	A_7	"	"	n-type; intrinsic; Large $\frac{\mu_e}{\mu_p}$	5×10^{-3}	$90^{\circ}K$
Bi_2Te_3-Bi_2Se_3 alloy	C_{33}	"	"	n	2.8×10^{-3}	$300^{\circ}K$
Bi_2Te_3-Sb_2Te_3	C_{33}	"	"	p	Pos 3.2×10^{-3}	$300^{\circ}K$
Sb_2Se_3 alloy	Some superlattice (hexagonal)					
$Ag_xPb_{1-x}SbTe_2$	B_1 NaCl (disordered)	Cubic with rhombohedral tendencies	O^5_h-F_{m3m} with D^5_{3d}-$R\bar{3}m$ tendencies	p	3×10^{-3}	$600^{\circ}K$
Thermomagnetic (Nernst-Ettingshausen)						
$Bi_{97}Sb_3$	A_7	Rhombohedral	D^5_{3d}-$R\bar{3}m$	intrinsic; n-type; $\frac{\mu_e}{\mu_p}$	S_{xy} up to $3400\mu v/^{\circ}C$ at $90^{\circ}K$; 6×10^{-3} $6000\mu v/^{\circ}C$ at $30^{\circ}K$	Z^a_{ji} $130^{\circ}K$

INTERDISCIPLINARY APPROACH TO IDENTIFICATION AND UNDERSTANDING OF HIGH Z THERMOELECTRIC MATERIALS

Interdisciplinary Definitions of Crystals-Applicable to Thermoelectric Materials

Thermoelectric materials are crystalline solids. Crystal structures are geometrical three dimensional arrangements of atoms. Such an array of atoms assumes a structure which represents a minimum energy orientation of the atoms in space satisfying a particular bonding scheme. The bond scheme is determined by the interaction of the electron energy levels characterizing the bonding or valence electrons of the particular types of atoms present in the array. The bonding forces are electrostatic in nature arising because of the relationship of forces exerted by the electronic and nuclear charges of the participating atoms. The electron shell structure of the valence electrons of the participating atoms and the bond scheme assumed in such an array of atoms determines the distribution of bound, quasi-free and free electrons between and around the atoms in the crystal. This same electron distribution determines the electron energy band structure and therefore the relative energy positions of the extrema characterizing the valence and conduction bands. The total density of allowed electron states in any one band is two electrons of opposite spin per unit cell of the crystal.

The electrons in the allowed states at the bottom of the conduction band or holes among the allowed states at the top of the valence band participate in determining the charge carrier transport properties characterizing the crystal.

The minimum energy orientation of the atoms in space, being a direct result of the valence electron bond scheme, which is in turn determined by the nature and type of interaction of the valence electron shell structure of the participating atoms, can assume several types of symmetrical periodic configurations in space, recognized by crystal lattice indices which reveal the interatomic spacings, within the limits imposed at one extreme by the radii ratio of the atoms and the general principle of geometrical closest packing of atoms, and the weakest directional bonding at the other extreme.

The latter limits and the nature of the atoms in the atomic table constrict the arrays possessing symmetry observed in crystals to one of fourteen lattice types (See Table 4) defined by its primitive vectors and by the character of its unit cell, the latter being the parallopiped formed by the three translations selected as units.

Table 4. The Fourteen Lattices[14]

System	Axes	Angles	Unit cells	Symbols: Schoenflies	Symbols: Hermann
Triclinic	$a \neq b \neq c$	$\alpha \neq \beta \neq \gamma$	Primitive	Γ^1_w	P
Monoclinic	$a \neq b \neq c$	$\alpha = \gamma = 90^{\circ}$ β obtuse	1 Primitive 2 1 face centred	Γ^2_m Γ^3_m	P C*
Orthorhombic ...	$a \neq b \neq c$	$\alpha = \beta = \gamma = 90^{\circ}$	1 Primitive 2 Face centred 3 All faces centred 4 Body centred	Γ^1_v $\Gamma^2_v(c)$ Γ^3_v $\Gamma^4_{v'''}$	P C† F† I
Tetragonal	$a = b \neq c$	$\alpha = \beta = \gamma = 90^{\circ}$	1 Primitive 2 Body centred	Γ^1_t Γ^2_t	P I
Cubic	$a = b = c$	$\alpha = \beta = \gamma = 90^{\circ}$	1 Primitive 2 All face centred 3 Body centred	Γ^1_c $\Gamma^2_{c'}$ $\Gamma^3_{c''}$	P F I
Rhombohedral ...	$a = b = c$	$\alpha = \beta = \gamma \neq 90^{\circ}$	Primitive	Γ^1_h	R
Hexagonal	$a = b \neq c$	$\alpha = \beta = 90^{\circ}$ $\gamma = 120^{\circ}$	Primitive	Γ^1_h	C‡

* By choosing different a and b axes the c-centred monoclinic cell will be seen to be equivalent to a primitive cell in which $a = b \neq c$, $\alpha = \beta = 90^{\circ}$, $\gamma \neq a$. Even if these axes are selected, the symbol C is retained for this cell.
† By suitable change of axes it is possible to convert the orthorhombic C and F cells into primitive and body centred cells respectively having $a = b \neq c$, $\alpha = \beta = 90^{\circ}$, γ obtuse. The symbols for these alternative settings remain C and F.
‡ This is a special form of the alternative setting described in the preceding note for the orthorhombic C cell. It is therefore given the symbol C.

Crystals can also be characterized by types of chemical bonds. A strong degree of electrostatic interaction between certain atoms of the atomic table gives rise to ionic bonding. Exchange interaction between directional p-orbital electrons results in covalent bonding. Hybridization of electrostatic and exchange interactions gives the sp^3 hybrid bond. A more complex hybridization is the resonance bond. And of course, there are the extreme types of bonds, metallic (strong) and Van der Waals (weak).

The Specific Nature of the Problem of Improving Z of Thermoelectric Materials

One can describe this problem in a stereotyped fashion as consisting of the following steps:

1). selecting atoms
2). bonding them together

3). obtaining a crystal structure
4). identifying the crystal structure
5). identifying the band structure
6). determining the electron and phonon transport properties which characterize the band structure
7). determining the figure-of-merit

Although these are the steps, the order in which they can be performed is not as indicated. Also the difficulties confronted in predicting higher Z material must be considered.

Limitations Imposed on Predicting Higher Z Thermoelectric Materials

It would appear that since the chemistry discipline deals with selecting atoms and bonding them together, basic chemistry theories and principles can be used to advantage. The bond approximation is basic in this area.

The crystallography discipline deals with structures which can be described by geometrical transformations using primitive vectors.

The physics discipline deals with band structure and theories of transport. The band approximations have had considerable success in solving problems of crystals.

Superficially, it appears that a coupling of bonding theory and principles with structure analysis and band theory should lead to predicting materials with improved thermoelectric properties.

Band Theory and Its Limitations

The band theory of solids[15] which has been successfully used to explain an impressive list of electronic and phonon transport phonomena in crystalline solids arises from solutions of the Schroedinger wave equation. An exact solution of this equation for a many-electron system (e. g. any crystalline solid) is impossible. Therefore all quantitative theories of electron and phonon transport rest on approximations.

In the simplest form of the band theory of electron transport, the crystalline lattice is considered as a region in which the electrostatic potential varies with the periodicity of a simple isotropic lattice. The solution of the Schroedinger wave equation for one electron at a position $\vec{r}$ for this extremely simple case is:

$$\Psi_r = u_k(\vec{r})\, e^{i\vec{k}\cdot\vec{r}} \qquad 5)$$

where

$u_k(\vec{r})$ is a function periodic in three dimensions depending on the wave vector $\vec{k}$

It can easily be shown that the plane wave $e^{ik\cdot r}$ is modulated by the period of the lattice and has a momentum $p = \frac{hk}{2\pi}$ and a de Broglie wave length $\lambda = \frac{2\pi}{k}$. Further the energy of the electron is given to a first approximation in the assumed isotropic lattice by:

$$E_k = \frac{h^2 k^2}{8\pi m^*} \qquad 6)$$

This means that E_k has the form of a quasi-free electron with an effective mass, m*. The allowed values of k and therefore E_k are grouped into bands containing two electrons of opposite spin per unit cell of the crystal. The occupied bands may or may not overlap and may or may not be completely filled, thus giving rise to categories like insulators, semiconductors, semimetals and metals among the various possible crystalline structures assumed by the atoms of the atomic table.

Application of this so called "band approximation" starts with X-ray crystallographic data from a specific crystal lattice and rests on assumptions about the periodicity and uniformity of the periodicity of the electron distribution through the lattice.

By considering many types of perturbations of the periodicity of the electrostatic field and using the principle of the self consistent field and a feed back procedure requiring additional assumptions about the average field distribution in the specific crystal lattice, it is possible to obtain an average but accurate description of the electrostatic potential and with it a detailed description of electron wave functions and energies for the specific crystal lattice.

Band approximations, however, cannot predict the exact chemical composition which will give the particular crystal structure nor the nature of the atoms required and the type of chemical bonding which would give the average electrostatic field distribution that generates the electron wave functions and energies in the band structure of the crystal lattice.

Further, it is apparent that, starting with measurements of the transport properties, band theory provides no way of predicting the crystal structure in which these are observed.

Bond Theory and Principles and Their Limitations

Chemical bonding theory[16] is not founded on first principles and hence is not able to be quantitatively connected to band theory. That is, although the bond scheme assumed in an array of atoms in a crystal is directly related to the distribution in space of electrons between and around its atoms and the bonding forces are electrostatic in nature, arising because of the electronic and nuclear charges of the participating atoms, bonding theory does not involve any proposals about moving electrons and hence the laws of conservation of momentum and energy are not part of its foundation as is the case with band theory. The theory is semiempirical in nature and is therefore called the bond approximation.

In employing the bond approximation, one considers two (nearest) neighboring atoms in a crystal lattice whose natures are known. Hence, its starting point is the fund of knowledge available on each of the atoms in the atomic table including nuclear charge, arrangement of the electrons in the electron shell structure, ionization potentials, the degree of filling of the outermost principal shell, and observed chemical valence properties of the atoms. The bond approximation directs attention at the resultant distribution of electronic charge between neighboring atoms and essentially neglects the effects of next nearest neighbors. This is an inherent weakness not easily amenable to quantitative refinements.

The strength of a bond can be directly correlated to the natures of the participating atoms and the types of bonds they can make.

The types of bonds formed between two atoms determines their effective radii. The sum of the effective radii gives the interatomic spacing. Thus, one must know the bond type before assigning the radius.

In general it is characteristic of the atoms of the atomic table with principal quantum numbers greater than one that their outer shells consist of 4 orbitals; one s and three p, each orbital being capable of accomodating two electrons of opposite spin. Further, the s orbitals are non directional in bonding, while the p orbitals (6 possible lobes) are directional, at 90^{o} with one another.

Application of quantum mechanics to the case of a diatomic molecule shows that if one such orbital overlaps a similar orbital of a neighboring atom, the two are transformed into two new orbitals. As shown in Figure 2a, one of these is called a bonding molecular orbital or simply a "valence bond" while the other is called an "antibonding" orbital. The valence bond has a lower energy than its parents and the antibond a higher energy. By themselves, the two parent orbitals involved require two electrons of opposite spin each for maximum stability. When combined, they require only two electrons of opposite spin between them to acquire a stable configuration.

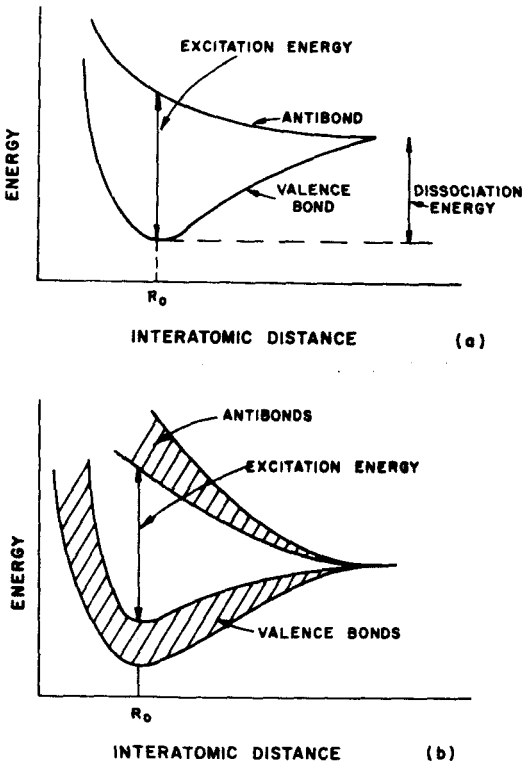

Fig. 2. Representation of the valence bonds and antibonds (a) in a hydrogen molecule, and (b) in a solid.

If an atom attempts to bond to another and there is an excess of electrons greater than the allowed two opposite spins per valence bond, they must go into the antibond, which destabilizes the system and counteracts the energy of bond formation.

Since each filled bonding orbital cannot have the same energy as other ones in the same system (Pauli exclusion principle) the bonds become a band of energy bonds in a polyatomic system as shown in Figure 2b.

In general, we see therefore, that the energies of the valence and antibonds are a function of the degree of overlap of bonding orbitals which in turn depends on the atom separation. For a system of two bonded atoms, there is a minimum energy at an atom separation r_o for which the bond is most stable. At closer than

this separation coulombic repulsion forces the atoms apart. At this distance, the excitation energy ΔE is a maximum and E_d is the energy of dissociation or energy of formation.

For any diatomic molecule the wave function for the valence bond can be separated into covalent and ionic terms

$$\Psi_{bond} = \Psi_{cov} \text{ and } \Psi_{ion} \qquad 7)$$

It can be shown that Ψ_{cov} concentrates the electrons in the region between the nuclei and Ψ_{ion} concentrates them around the nuclei. Associated with Ψ_{ion} is an energy E_{ion} and with Ψ_{cov}, an energy E_{cov}.

Although the theory of bonding for a diatomic molecule can only qualitatively be applied to a polyatomic system, the principle of directed valence for p orbitals and sp^3 hybridized orbitals is valid for polyatomic systems. This principle, through quantum mechanics, imposes the requirement on polyatomic systems that the several atomic orbitals employed by one atom in covalent bonding must have certain orientation bond angles relative to one another.

Crystal Structure Analysis and its Limitations

Identification of crystal structure[17] by recording the destructive and constructive interferences of X-rays incident on a periodic array of atoms characterizing the structures provides direct information on the relative position of the atoms in space and thus yields information on interatomic distances and the arrangement of atoms in the structure.

Any periodic anisotropy of interatomic spacings is revealed. Thus in the cases of structures containing mixed bonding, X-ray and associated types of identification of the crystal structure provide the only way of determining interatomic spacings, bond angles, etc.

Although all structures determined by the crystallographic method fall into one of 14 lattice types, as pointed out previously, (See Table 4), many structures with various degrees of distortion from these lattice types are recognized. Exact identification of aperiodicities in a specific lattice structure is not easily revealed.

Crystallographic identification only reveals the result of the vector sum of forces acting on the electron distribution in placing the atoms in a crystal lattice and will reveal distortion only if sufficient periodicity of aperiodicities is present.

Method of Approach to the Problem

The deficiencies in the foregoing theories rules against quantitative couplings. Nevertheless, it is apparent from the integrated interdisciplinary description of crystalline solids that important qualitative associations of fundamental significance can be made between the nature of the atoms and their bonding characteristics and the transport properties of the resultant crystals.

Specifically, it appears feasible at this time to do the following in view of accumulated data and interpretations of these data toward isolating the required nature of improved Z_p, thermoelectric cooling materials.

1). Select a known high Z material and independently describe its chemical bonding, crystal structure and transport properties.
2). Roughly generate its band structure from its crystal structure.
3). Interpret Z_p, thermoelectric, and related transport properties in terms of the bond structure and the apparent band structure derived from accumulated data obtained from sophisticated experiments on magnetoresistance and various other oscillatory effects.
4). Classify the known types and occurrence of chemical bonding in solids and identify the bonding in the selected high Z material within this classification.
5). Classify the types of crystal structures found in solids and identify the high Z material in this classification.
6). Using correlation parameters obtained from chemical bonding and crystallographic disciplines, graphically relate basic transport and band structure properties with these correlation parameters for compounds and elements representative of what the atomic table has to offer.
7). Identify the position of the selected high Z material in each correlation plot of 4, 5, and 6 above.
8). Within the limits possible, attempt an interdisciplinary interpretation of the selected high Z material to reveal the most significant features controlling its properties.
9). Examine the possibilities of developing improved high Z materials in the light of the interdisciplinary specifications deduced for the high Z material.

Besides providing the classification and correlation plots indicated in 4, 5, and 6, it is vitally important to recognize how the nature of the band structure is related by band theory to the mathematical formulations commonly used to analyze the dependence of parameters of the

thermoelectric Z on band transport properties.

In the following sections the important aspects of band theory, bond classification, and structure classification, and also graphical correlations using various correlation parameters are presented.

Band Structure and its Relationship to Expressions for the Figure-of-Merit Z_p

In application of band theory[18] to determining the transport parameters of solids, one is first concerned with the degree of occupancy of the valence bands and the Brillouin zone representation of these bands.

If the outermost band or zone is only partly filled, the Fermi level is located part way up the band and electrons near the Fermi level can take part in conduction. If it is filled to capacity, no electrons are available for conduction and the material is classified as follows. If the energy gap between the top of the full valence band and the bottom of the next higher allowed band is large, the material is an insulator. If it is relatively small, it is an intrinsic semiconductor. If it is near zero or there is an overlap, the material is an intrinsic semimetal. If there is a major overlap, the material is a metal.

It is important to note that all band theory generated expressions for transport properties and thermoelectric properties reflect assumptions about the nature of the band structure.

Case of a Simple Band

A simple band is characterized by the energy of an electron at its single extremum in $\vec{k}$ space varying as k^2 (parabolic law). For this case, the constant energy surfaces are spheres centered at $\vec{k} = 0$.

The energy states of this band are distributed over a permitted range of energies and one can speak of the density of states per unit energy interval at any energy and the spherical constant energy surfaces are given by:

$$E = E_c + \frac{h^2 k^2}{2m_c^*} \qquad 8)$$

where

E = allowed energy of states
E_c = energy at the extremum of the band
k = wave vector
m_c = effective mass of electron with energy E_c

Density of States in a Simple Band

The density of states is then given by

$$g(E) = 4\pi \left(\frac{2m_c^*}{h^2}\right)^{\frac{3}{2}} \left(E-E_c\right)^{\frac{1}{2}} \qquad 9)$$

When a band includes a small range of energy

1. contours corresponding to successive energies are widely spaced in the Brillouin zone
2. The density of states/unit energy interval as described by the above expression is high and the effective mass is large and the velocity and acceleration of an electron are small.

It follows that electrons with large effective mass have small mobility in the band. Conversely, highly mobile charge carriers of low effective mass are to be found in a band spread over a wide range of energy to keep the density of states small.

Density of States in Complex Bands

As long as the energy increases in the band as k^2, the energy surfaces can be far from spherical (e.g., prolate or oblate ellipsoidal) and still the density of states will be expressed as above, provided recognition is given to modified expressions for the effective mass.

Examples of specific expressions for effective mass, of significance in our later interpretations, are as follows:

1. If the band has one minimum and spherical constant energy surfaces:

$$m_c^* = m^* \qquad 10)$$

2. If the band has one minimum and ellipsoidal constant energy surfaces:

$$m_c^* = (m_x m_y m_z)^{\frac{1}{3}} \qquad 11)$$

3. If the band has N minima at symmetrical points in the Brillouin zone:

$$m_c^* = N^{\frac{2}{3}} (m_x m_y m_z)^{\frac{1}{3}} \qquad 12)$$

4. If two or more separate bands, each with a single extremum, having masses m_1, and m_2 etc. are degenerate in energy at their extrema, the total density of states can be expressed in terms of the above equation for g (E) with:

$$m_c^* = \left[m_1^{*\frac{3}{2}} + m_2^{*\frac{3}{2}} + \cdots m_i^{*\frac{3}{2}} \right]^{\frac{2}{3}} \quad 13)$$

As we will see later, the differentiation between case (4) and case (1) is of great significance in characterizing high Z thermoelectric and thermomagnetic cooling materials.

Concept of Fermi Level and Degeneracy for Case of a Simple Band

In order that we can deal with charge transport in bands of electron states occurring in crystalline solids, the position of the Fermi level, E_f, relative to E_c, the bottom of the conduction band or E_v, the top of the valence band is of great significance.

If a band containing electrons (e. g., by thermal excitation) with minimum energy E_c is well above E_f, then the density of electrons in this band will be given by:

$$n = \frac{2}{\sqrt{\pi}} N_c F_{\frac{1}{2}}(\xi) \quad 14)$$

where

$\xi = \frac{E_f}{kT}$; the reduced Fermi level of the crystal for E_c assumed to be the zero energy reference

$N_c = 2\left(\frac{2\pi m^* kT}{h^2}\right)^{\frac{3}{2}}$; the "effective" density of states in the conduction band

m^* = density of states effective mass

$F_{\frac{1}{2}}(\xi)$ = Fermi integral

In the case where the Fermi level is sufficiently far below the conduction band extremum, E_c, $\xi \leq -2$ and the Fermi Integral can be replaced by a simple approximation and then (case of non-degeneracy).

$$n_e = N_c e^{\xi} \quad 15)$$

On the other hand, if the charge carrier concentration, n_e, increases in the conduction band, ξ becomes less negative, zero and then positive valued. For such cases, the expression for n containing the Fermi integral must be used. (case of degeneracy).

In regard to hole conduction in the top of the valence band, it can be shown that

$$n_p = \frac{2}{\sqrt{\pi}} N_c F_{\frac{1}{2}}(-\epsilon - \xi) \quad 16)$$

where

$\epsilon = \frac{E_g}{kT}$ reduced energy gap

$\xi = \frac{E_f}{kT}$ reduced Fermi level

Examination of the effect of degeneracy on the transport parameters characterizing the electrons in the conduction band or holes in a valence band is highly significant in later interpretations.

In general if the density of states effective mass is small and therefore the mobility is large in the conduction band, the n_e/cc, density, at which $\xi > -2$, will be a lower value at a given temperature than if the effective mass is large and the mobility is small in the conduction band.

The effect of degeneracy is to reduce the average electron mobility of the electrons in the conduction band.

At a constant value of n_e/cc in the conduction band, we expect to find that there will be a specific temperature below which the electron energy distribution in the conduction band will be degenerate. This temperature, characterizing the onset of degeneracy, will be lower, the higher the effective mass of the band, and therefore the lower the mobility.

Of significant importance is the occurrence of degeneracy in a group of separate conduction bands with the same value of E_c at the extrema. We note that a condition for their being separate and having the same E_c is that the Fermi level is the same for all of them. However, the condition for degeneracy applies to each band separately. This recognition is of greatest importance in interpretation of transport data on high Z materials with Z_{max} at relatively low temperatures.

Transport Equations for Conduction and Valence Bands

In general the transport equations applying to a simple band are all that is basically necessary for our considerations, assuming E vs. k^2

applies and conduction is either by electrons or holes, providing we (1) insert the proper expression for m_T^*, the total effective mass in the equations which apply to the conduction band structure of the measured material, (2) make any other adjustments which are demanded by the m_T^* expression and (3) observe the use of $F_{\frac{1}{2}}(\xi)$ or e^{ξ} when respectively in the degeneracy or non degeneracy range of temperature for the particular value of charge carrier concentration in each band.

Briefly the transport equations of interest to us are as follows for a single simple band, (although we consider electrons, these equations apply equally well to holes).

Electrical Conductivity σ

$$\sigma_e = n_e e \mu_e \qquad 17)$$

μ_e is the mobility of electrons in the band.

Mobility, μ_e

$$\mu_e = \frac{e\bar{\tau}}{m^*} \qquad 18)$$

$\bar{\tau}$ is the average relaxation time of electrons due to whatever scattering occurs

Relaxation time, τ

$$\tau = \tau_o E^s \qquad 19)$$

τ = relaxation time of an electron assuming a rigid lattice and scattering of electrons by it

τ_o = coefficient which is independent of energy of the electron and is only dependent on temperature

E^s = the power dependency of τ on electron energy which reflects the type of scattering

The values of s applying to the three types of electron scattering commonly encountered are:

acoustic mode	$s = -\frac{1}{2}$
optical mode	$s = +\frac{1}{2}$
ionized impurity	$s = +\frac{3}{2}$

When $\xi < -2$ (non-degeneracy), $\bar{\tau}$ approaches a constant value as mentioned previously; μ decreases when $\xi > -2$ and the Fermi level comes closer to the bottom of the conduction band. The latter is a direct result of the fact that $\bar{\tau}$ decreases as degeneracy sets in.

Thermoelectric power, S

$$S = -\frac{k}{e}(\delta - \xi) \qquad 20)$$

where

$\delta = s + \frac{5}{2}$

if τ is given by $\tau = \tau_o E^s$ and $\xi < -2$

or

$$S = -\frac{k}{e}\left(\frac{(s+\frac{5}{2})\,F_{s+\frac{3}{2}}(\xi)}{(s+\frac{3}{2})\,F_{s+\frac{1}{2}}(\xi)} - \xi\right) \qquad 21)$$

where

$$\delta = s + \frac{5}{2}, \quad \tau = \tau_o E^s$$

and

$$\xi > -2$$

Hall constant, R_H

$$R_H = \frac{r}{n_e e} \quad \text{(general case)} \qquad 22)$$

$$= \frac{1}{n_e e} \qquad \xi >> -2$$

$$= \frac{3\pi}{8}\,\frac{1}{ne} \qquad \xi < -2$$

Electron thermal conductivity, k_e

$$k_e = \delta\left(\frac{k}{e}\right)^2 \sigma_e T \qquad 23)$$

where

$$\delta = s + \frac{5}{2} \text{ if } \xi < -2$$

or

$$\delta = \frac{(s+\frac{5}{2})\,F_{s+\frac{3}{2}}(\xi)}{(s+\frac{3}{2})\,F_{s+\frac{1}{2}}(\xi)} \text{ if } \xi > -2 \qquad 24)$$

Lattice thermal conductivity, k_{ph}

This transport parameter is a result of phonon transport. Just as there are electron bands in a crystal lattice there also are allowed phonon bands or modes.

Two expressions are given here. The first is a generally applicable one and the second was derived quantum mechanically by Lawson[28] in terms of measurable parameters of the structure.

$$k_{ph} = \frac{1}{3} C v l \qquad 25)$$

C = lattice specific heat

v = velocity of sound waves in the lattice

l = phonon mean free path

$$k_{ph} = \frac{r_o}{3d^{\frac{1}{2}} \chi^{\frac{3}{2}} \gamma^2 T} \quad 26)$$

r_o = distance between nearest neighboring atoms

d = density - average mass per atom divided by average volume occupied per atom

γ = Gruneisen parameter for a solid - obtainable from thermal expansion data - contains effect of anharmonic forces in the lattice

χ = compressibility of the crystal

If simultaneous conduction occurs in a simple valence and conduction band the following modifications apply.

$$\sigma = n_e e\mu_e + n_p e\mu_p \quad 27)$$

$$S = \frac{S_e \sigma_e + S_p \sigma_p}{\sigma_e + \sigma_p} \quad 28)$$

where

S_e has a negative sign and S_p a positive sign and S_e and S_p are both given by the expression for S of a single band with appropriate substitution of (ξ) and $(-\epsilon - \xi)$

$$R_H = \frac{n_p \mu_p^2 - n_e \mu_e^2}{(n_e \mu_e + n_p \mu_p)^2} \quad 29)$$

$$k_T = k_e + k_{ph} + k_{amb} \quad 30)$$

where

k_{amb} = ambipolar contribution due to electron-hole pairs

$$= \left(\frac{k}{e}\right)^2 T \left(\frac{\sigma_e \sigma_p}{\sigma_T}\right) \left[\frac{E_g}{kT} + 4\right]^2$$

where

$\frac{E_g}{kT}$ = energy gap ϵ

Expression for Figure of Merit, Z_p

We know that the Figure-of-Merit of a thermoelectric material is given by:

$$Z = \frac{S^2 \sigma}{k_e + k_{ph}} \quad 31)$$

From the foregoing discussion we see that if a simple band characterizes conduction in the material and $\xi \leq -2$.

$$Z = \frac{\left(\frac{k}{e}^2 N_c \frac{\mu_e}{k_{ph}} T\right) \left[(\delta - \xi)^2 e^{\xi}\right]}{T\left[1 + (s + \frac{5}{2})\left(\frac{k}{e}^2 N_c \frac{\mu_e}{k_{ph}} T\right) e^{\xi}\right]} \quad 32)$$

Examination of this expression reveals that ξ, the reduced Fermi energy, is the factor which must be maximized in order to maximize Z.

By taking the derivative of Z in respect to ξ, and setting it equal to zero, the ξ value for Z_{max} can be found.

$$(s + \tfrac{1}{2} - \xi)\, e^{\xi} = (2s + 5)\left(\frac{k}{e}^2 N_c \frac{\mu_e}{k_{ph}} T\right) \quad 33)$$

From this expression we can further deduce that at maximum ξ, the highest Z should be obtained if the following expression is maximized.

$$A \propto (m^*)^{3/2}_e \, s + 1/2 \, \frac{\mu}{k_{ph}} \quad 34)$$

Discussion of Maximizing Z_p

In Figure 3 the relationship, for the case of one simple band, of trends of S, σ, k_e, k_{ph}, and Z_p, as a function of increasing charge carrier concentration is given. It is important to recognize that these relationships represent the case of the Fermi level, $E_f \cong E_c$. In other words the Z_p in Figure 3 is not only maximized in regard to concentration of electrons but also in regard to the temperature at which the Fermi level is nearly coincident with the bottom of the conduction band.

As shown in Figure 3, at one charge carrier concentration, Z_p will increase if S and σ both increase or one of these increases and the other stays constant, providing k_{ph} stays constant and $k_{ph} \geq k_e$. Another variation of interest is to maintain $S^2 \sigma$ constant and decrease k_{ph}.

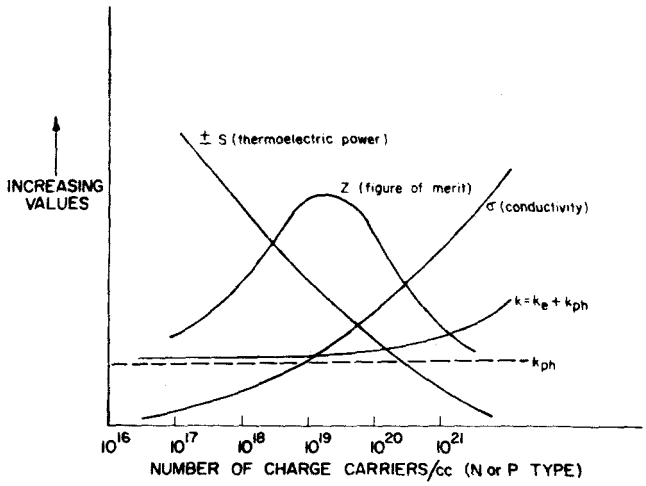

Fig. 3. Relationship of Z_p, S, k_T and σ trends as a function of number of extrinsic charge carriers for a given material at a constant temperature.

Because of the interlocking relationships between band structure parameters, concentration of charge carriers, and temperature at which degeneracy occurs for the maximized concentration of charge carriers we appear to have a way to deduce the maximum Z for a selected temperature for the case of a simple band. This requires setting the charge concentration at 10^{19}/cc and finding the mobility when the Fermi level is at the bottom of the simple conduction band. Although this answer is very desirable, unfortunately it precludes that we know the range of band structure parameters for all the simple band crystals which the atomic table could ever offer. That is, the effective mass for a simple band with spherical constant energy surfaces in the case of one hypothetical crystal is different than another, since actually the simple band parameters change with interatomic spacing.

This specific discussion emphasizes the theoretical difficulty of determining via band theory the Z_{max} for even a simple band.

Despite the indeterminacy of Z_{max} for an optimized simple band, we can conclude in a relative fashion that the highest Z material will be one having a low k_{ph} for which m_T^* is maximized by increasing, to the largest possible value, the number of separate bands characterized by ellipsoidal constant energy surfaces which have the same extrema energy.

Types of Chemical Bonding in Solids

There are four main classifications of bond types between atoms of the periodic table. These are ionic, covalent, metallic, and Van der Waals. They can be distinguished as follows

Ionic

No sharing of electrons between adjacent atoms; - no directional characteristics of the bond. Atom packing arrangement in crystal is determined by the radii and geometrical principles of ionic closest packing.

Valence electrons are transferred from atoms of one type to atoms of a second type to produce ions which are oppositely charged and which locate themselves in an array such that the attraction between oppositely charged ions counteracts the repulsion between ions with the same charge.

The NaCl cubic primitive lattice structure is usually assumed in such combinations.

Covalent

Valence electrons of neighboring atoms of different kinds are shared. Charge density is high between the atoms and has a distinctly directional character.
The directional character is determined by the nature of the atomic orbitals involved in bonding.
The radii of atoms bonded covalently depends on the type and strength of the bond. These radii are normally less than radii of electronegative ions and normally larger than those for electropositive ions.

Metallic

The overlap of bonding orbitals is so profuse, the valence electrons are shared by all the atoms of the crystal - effectively forming an array of positively charged ions in a "sea" of negative charge.

Van der Waals

This type is characterized by very weak interaction of valence electrons and is found to occur between molecules in molecular crystals.

Ionic bonds have an energy E_{ion} predominantly controlled by the difference in electronegativity of the atoms.

$$E_{ion}^{A-B} \propto (X_A - X_B)^2 \qquad 35)$$

where

X_A is electronegativity of atom A using Pauling's scale

X_B same as above for atom B

Covalent bonds have an energy E_{cov} primarily determined by the size of the atoms and their atomic weight in compounds where there is only one type of covalent bond. E_{cov} can be expressed as the arithmetic mean of the bond energies.

$$E_{cov}^{A-B} = (E_d^{A-A} E_d^{B-B})^{1/2} \quad (36)$$

where E_d^{A-A} and E_d^{B-B} are the experimentally determined dissociation energies of the bonds between similar atoms.

The dissociation energy or heat of formation, E_d^{A-B}, of a molecule A B is a measure of the covalent bond energy, E_{cov}^{A-B}, plus E_{ion}. E_d^{A-B} is called a single bond energy.

Covalent bonding is the most interesting form of bonding since it is directional in character. In Table 5 eight types of covalent bonds are listed. Also, their relative strengths, bond angles, and number of bonds are shown. The directional bonds shown here are either a p orbital 90° bond or some form of hybridized p orbital bond. Hybridization of p orbitals is possible with s and/or d orbitals.

TABLE 5

COVALENT BOND TYPES

No. of Bonds	Orbitals Used	Characteristic Bonding Angle	Relative Strengths
1	s	--------	1.000
3	p	Mutually perpendicular (90°)	1.732
4	sp^3	Tetrahedral (109°28')	2.000
3	hybrid s-p	Planar (120°)	1.991
2	s-p	Linear	1.932
6	d^2sp^3 or sp^3d^2	Octahedral	2.923
6	d-s-p	Trigonal Prism	2.983
4	dsp^2	Square	2.694

The p-orbital type of covalent bond is a 3 electron-pair bond and is especially interesting. It is expected for atoms with an outer shell configuration s^2p^3. Therefore, it is common to N, P, As, Sb, and Bi. In these cases, the s orbital is filled and the 3 p orbitals are half filled (one electron each). The condition of directionality for valence bonding requires that the three p orbitals be spatially oriented at right angles with one another.

In the "inert pair" group of elements on the right side of the atomic table, shown in Table 6, the s orbital electrons tend to become a part of the nucleus and only the p orbitals act in bonding. In this case, the s orbitals are nonbonding orbitals. The fourth ionization potential for atoms in this group, having an s^2p^3 configuration, is much larger than the first through the third. As, Sb, and Bi fall into this classification.

IA	IIA											IIIA	IVA	VA	VIA	VIIA
Li	Be											B	C	N	O	F
1.0	1.5											2.0	2.5	3.0	3.5	4.0
Na	Mg											Al	Si	P	S	Cl
.9	1.2											1.5	1.8	2.1	2.5	3.0
		IIIB	IVB	VB	VIB	VIIB		VIII B			IB	IIB				
K	Ca	Sc	Ti	V	Cr	Mn	Fe	Co	Ni	Cu	Zn	Ga	Ge	As	Se	Br
.8	1.0	1.3	1.5	1.6	1.6	1.5	1.8	1.8	1.8	1.9	1.6	1.6	1.8	2.0	2.4	2.8
Rb	Sr	Y	Zr	Nb	Mo	Tc	Ru	Rh	Pd	Ag	Cd	In	Sn	Sb	Te	I
.8	1.0	1.3	1.4	1.6	1.8	1.9	2.2	2.2	2.2	1.9	1.7	1.7	1.8	1.9	2.1	2.5
Cs	Ba	La	Hf	Ta	W	Re	Os	Ir	Pt	Au	Hg	Tl	Pb	Bi	Po	At
.7	.9	1.1	1.3	1.5	1.7	1.9	2.2	2.2	2.2	2.4	1.9	1.8	1.8	1.9	2.0	

-- Indicates demarcation between "inert pair" group to right and rest of table to left.

Table 6. ELECTRONEGATIVITY CHART OF THE ELEMENTS OF THE ATOMIC TABLE

If pure p-orbital bonding occurs, one expects an octahedral coordination but often one finds a trigonal configuration with the three bonds at right angles with one another. Evidence that such bonding occurs in As, Sb, and Bi is seen in the crystal structure of these elements. They form rhombohedral crystals with trigonal symmetry. Figure 4 illustrates this structure for As, Sb, and Bi.

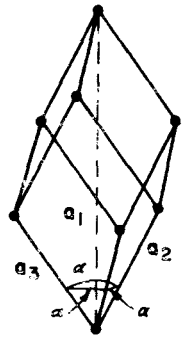

Fig. 4. Rhombohedral crystal structures characteristic of As, Sb, Bi.

Each pure p-orbital has two lobes, one on each side of the atom. Therefore, 3 p orbitals have 6 lobes extending out from the atoms at

right angles with one another. In the case of the "inert pair" s^2p^3 elements, the level of occupancy of these lobes will be one unpaired electron in three of the six lobes.

A stable valence bond is an electron pair bond involving two electrons of opposite spin. In order for pure p-orbital bonding "inert pair" elements to establish a stable valence bond, each bond between two atoms is a half bond containing one electron. Six half bonds are made in connecting one such atom to its neighbors to provide the equivalent of three electron pair bonds. Each pure p-orbital bond therefore only has half the strength of an electron pair bond.

In order for pure p orbital bonding to occur between two dissimilar atoms A and B, they must have a minimized small difference in electronegativity and a relatively large separation of s and p orbitals in both atoms.

Resonance Bonding

Resonance bonding is closely related to p-orbital bonding and is a special form of covalent bonding. Single bond energies can only be derived from molecules with simple electron pair bonds. Bond energies in a polyatomic molecule with coordinate links cannot be so determined. Furthermore even in the diatomic molecule case, the bond energy determination is limited to cases where there is no resonance between structures with different electron configurations.

Just as an atom has a number of discrete energy states, referred to as orbitals or eigenfunctions and distinguished by a set of quantum numbers, so also a molecule has a ground state and a system of orbitals. Each state of a molecule is represented by a wave function Ψ and associated with it an energy.

If a system of atoms has two possible structures, Y and Z, and wave functions Ψ_y and Ψ_z in the minimum energy state, then wave mechanics tell us

$$\Psi = a\Psi_y + b\Psi_z \qquad 37)$$

is a possible wave function of the system. The most stable configuration of the system could be obtained, if the ratio, b/a, giving the wave function corresponding to minimum energy, were known.

When coefficients a and b are comparable in value at minimum energy, the minimum energy state involves both structures and resonates between the two. The wave function corresponding to minimum energy is lower than the minimum energy of either structure.

This concept is not limited to two, but is applicable to any number of structures subject to the following important restrictions:

1. The same number of unpaired electrons are present in each structure
2. The structures have the same general configuration of nuclei

Organic chemistry tells us a resonant bonded molecular system is stronger, the longer the conjugated chain. Therefore we expect the valence and antibond energy bond widths to be greater than without resonant bonding since there are a greater number of electron pair bond states encompassed and because none of them can assume the same energy (Pauli Exclusion principle) in the resonant state. As a result of the fattening or broadening of the bands of bonds, the excitation energy can be expected to decrease. Further in a relative sense, the interatomic distance over which the resonance is occurring will decrease and the dissociation energy, E_d, will increase.

Considering the requirements for pure p-orbital bonding, there is a high probability of also finding resonance bonding in the same system. To meet bonding angle requirements and the establishment of a stable valence bond, the structures which are formed by elements able to make a pure p-orbital bond must necessarily contain highly directional complex molecules or special bonding characteristics.

Molecules bonded by resonance polymerize (cross-link) to pair up unpaired electrons.

P orbital bonding and resonance bonding between molecules is characteristic of Se, Te, and also I crystals. Between double layers such bonding is found in black phosphorus, As, Sb and Bi [19-21]. Figure 5 (after Krebs [19-20]) illustrates bonding, bonding angles, atomic arrangement, crystal axes, and the directions of resonance bond chains in As, Sb, and Bi crystals. Figure 6 (after Krebs [21]) does the same for hexagonal Se and Te.

A striking and important characteristic of the As, Sb, and Bi structure is the lattice builds up from discrete two dimensional double layer molecules, within which the atom separation is characterized by one distance, while between which the nearest atom separation is characterized by another longer distance. The Se and Te lattices build up by parallel alignment of one dimensional molecules. This leads in both cases

to anisotropic lattice spacings, as shown in Table 7. In Figure 7, we note that the $\frac{r_2}{r_1}$ ratios decrease with increasing atomic weight. This means that resonance bonds between planes and chains are becoming stronger with increasing atomic weight. This observation carries with it the expectation that as $\frac{r_2}{r_1}$ decreases, the crystals will show a change from insulating to semiconducting properties.

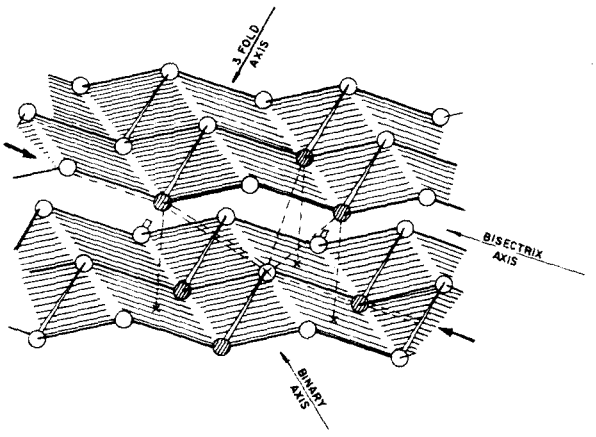

a) Representation of atomic arrangement, bonds, and resonance chains in double layers of As, Sb, and Bi crystals, showing 3 fold, binary, and bisectrix axes. (The resonance chain between layers is indicated by ⟶ --- ⟵; the degree of distortion of p orbitals between planes by ---; and the octahedral p-bonded atom by (x)) (after Krebs[20]).

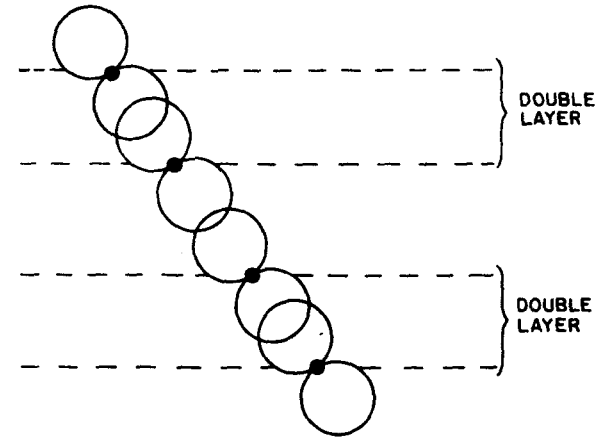

b) Two dimensional representation of resonance chain in As, Sb, or Bi crystals illustrating unsymmetrical overlap of p-orbitals (after Krebs[20]).

Fig. 5. Bonding, atomic arrangement, crystal axes and resonance bond chains in As, Sb and Bi crystals.

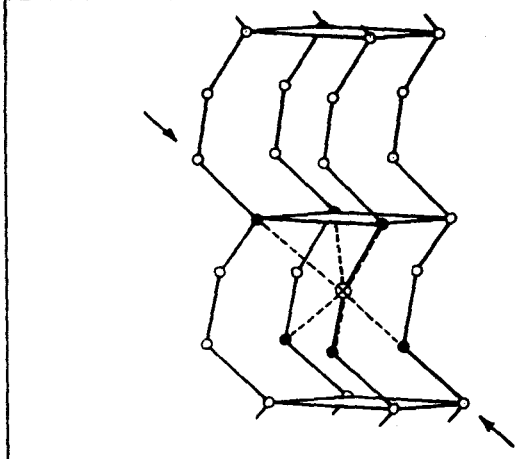

a). Hexagonal Se or Te structure showing resonance chain ⟶ --- ⟵ (The (x) and ---- illustrates p orbital octahedral bonds between chains) (after Krebs).

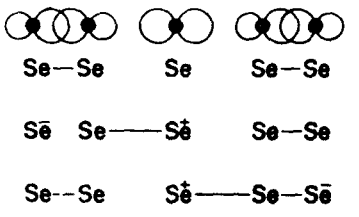

b). Chemical formula

Fig. 6. Krebs[21] representation of Se or Te structures (a) showing resonance chain and (b) formula for resonance chain.

TABLE 7

COMPARISON OF INTERATOMIC DISTANCES CHARACTERISTIC OF GROUP V and GROUP VI ELEMENTS

Name of Element	Atomic Weight	M. P. °C	Structure	Interatomic distance in A° within the plane or spiral chain r_1	Interatomic distance in A° between the planes or chains r_2	$\frac{r_2}{r_1}$	bonding angle ϕ
P	30.97	44	Rhombic	2.18	3.41	1.57	99° (103°)
As	74.92	817	Rhmdr.	2.51	3.15	1.25	97
Sb	121.7	660	Rhmdr.	2.87	3.37	1.17	96
Bi	208.98	271	Rhmdr.	3.10	3.47	1.12	94
Se	78.96	217	Hex.	2.30	3.48	1.51	103
Te	127.60	445	Hex.	2.86	3.46	1.22	102
Po	210	254	Cubic	3.34	3.34	1.00	90

Krebs[19-21] has found that superimposed resonance bonding not only occurs in the cases of pure p-orbital bonding but also in cases of various variations of hybridization of s and p orbitals. Resonance was investigated in PbS, PbSe, PbTe, Bi_2Se_3, Sb_2Te_3, Bi_2Te_2S, Sb_2S_3, Bi_2S_3, Sb_2Se_3, $Bi_2(SSe)_3$, GeS, SnS, $CuSbS_2$, HgS, TiS_2, NiAs type structures, Laves phases and various CdI_2

type structures. In general, resonance is retarded when light and heavy atoms are bonded as shown by the lack of crystal symmetry.

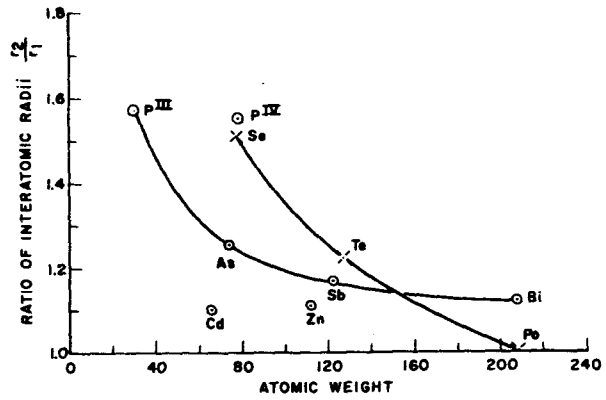

Fig. 7. Dependence of the ratio of interatomic distances for Group II, Group V, and Group VI elements on atomic weight.

Correlation Parameters

Although the theories of bonding and those of band structure and transport properties can not be connected quantitatively, semiempirical linkages between types of atoms and nature of bonding and the variations in Z and associated transport parameters of bands can be obtained via various correlation parameters.

Electronegativity

Electronegativity is one correlation parameter. Electronegativity, as defined by Pauling[16], is the ability of an atom to attract electrons to itself. Therefore the electronegativity X of a atom A is a chemical characteristic which reflects the difference of the energies of the reactions.

$$A + e^- \rightarrow A^- \qquad 38)$$

$$A \rightarrow A^+ + e^- \qquad 39)$$

The first reaction gives the electron affinity as the mean of the electron attraction of the atom and the negative ion. The second reaction gives the First ionization energy as the average of the electron attraction of the atom and the corresponding positive ion. Table 6 shows the electronegativity values in Pauling's units assigned to each of the elements. These electronegativity values are based on the average valence exhibited by the atoms. Many atoms can bond using various valences so for this reason electronegativity values must be carefully used.

In a compound, the difference in electronegativity of the elements composing it will control the degree of ionic character of the bonding.

Electronegativity values for the elements do not tell the role of polarizibility and polarizing powers of the individual atoms in unionized or ionized states.

Polarization and Polarizibilities

In general, the greater the principal quantum number, the larger the number of valence electrons, the greater the polarizibility and the smaller the polarizing power of the element.

When one combines a highly polarizable element with a less polarizable one, the driving electrostatic field will cause the electron structure of the highly polarizable atom to become distorted, thus tending to decrease the electronegativity difference, determined by Pauling's method.

It is expected that a specific percentage of psuedo-covalency of a bond, achieved by the presence of continuous polarization forces in the crystal lattice (common in cases of p orbital directional bonds) will influence the band structure and its transport properties in a manner such as to induce anisotropic mobilities whereas pure covalent bonding is expected to give isotropic electron and hole mobilities.

The percentage of psuedo-covalency could be estimated if a precise knowledge were available about the electrostatic potential as a function of the space coordinates in the whole lattice. This is equivalent to an exact identification of the charge disturbution in the whole lattice.

Ionicity

A method of separating out the ionic contribution to a bond and dealing directly with the psuedo-covalency of a mixed bond is provided through the concepts, proposed by Mooser and Pearson[22], and Folberth[23] of formal and effective ionicity. Formal ionicity of 100°/o refers to the charge configuration of the pure ionic state for a bond between two atoms. Zero percentage refers to the pure covalent state. Effective ionicity of 100°/o also describes the pure ionic state but zero percentage effective ionicity describes the neutral bond state.

Figure 8 pictorially shows Mooser and Pearson's[22] concept of the sp^3 tetrahedral bond scheme in Group IV elements and III-V, II-VI, and I-VII compounds. A comparison of this bond scheme for the cases of formal and effective ionicity is shown. Figure 9 illustrates idealized

bonding schemes for neutral, covalent and ionic bonds for III-V compounds.

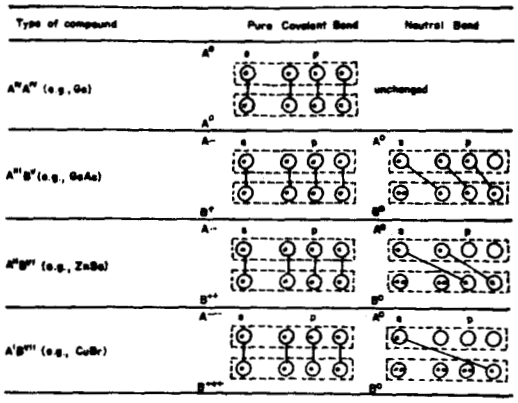

Fig. 8. Bond scheme for diamond-like semiconductors.

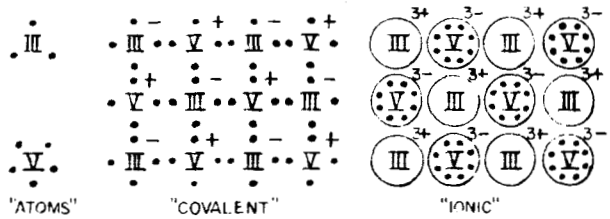

Fig. 9. Pictorial diagram of idealized bonding schemes.

The relationships between percentage formal and effective ionicity for GroupIV elements, and III-V, II-VI and I-VII compounds are shown in Table 8[23].

TABLE 8

FORMAL IONICITY AND EFFECTIVE IONICITY

OF DIAMOND-LIKE SEMICONDUCTORS (%)

Type of Compound	Effective Charge of the Lattice Sites							
	$A^{-3}B^{+3}$	$A^{-2}B^{+2}$	$A^{-1}B^{+1}$	O_A O_B	$A^{+1}B^{-1}$	$A^{+2}B^{-2}$	$A^{+3}B^{-3}$	Definition
$A^{IV}A^{IV}$ (e.g., Ge)				0				
$A^{III}B^{V}$ (e.g., GaAs)			0	25 0	50 33	75 67	100 100	formal ionicity effective ionicity
$A^{II}B^{VI}$ (e.g., ZnSe)		0	25	50 0	75 50	100 100		formal ionicity effective ionicity
$A^{I}B^{VII}$ (e.g., CuBr)	0	25	50	75 0	100 100			formal ionicity effective ionicity
	"Anti-ionic state"				"Ionic state"			

after Folberth[23]

We note

1. the effective ionicity scale does not contain the anti-ionic state
2. there is a different correlation between effective charge and ionicity on the formal ionicity scale as compared to the effective ionicity scale.

The electronic charge distribution in a compound crystal can thus be treated as a result of the separate bonding factors determining it. These are

1. the bond scheme which characterizes the binding of the atoms in the crystal
2. the relative polarizibility and polarizing powers of the cations and anions involved.
3. the influence of the radii ratio of the cations and anions

It can be shown[24, 25] that bonding in crystal compounds can be characterized by ionicity parameters as follows

$$\lambda = \lambda_o + \frac{e^*}{c} \qquad 40)$$

where

λ_o = atomic ionicity due to bond scheme

$\frac{e^*}{c}$ = polarity parameter, which is the residual ionicity remaining in the bonding after the polarizability and radii ratio effects are subtracted from the difference between atomic ionicity and the actual ionic contribution

Mean Atomic Weight

With increasing mean atomic weight of the cations and anions in compounds, the average atomic radii increase. In such a progression it is found that single bond energies, heat of formation, and excitation energy all decrease as shown in Figures 10 and 11.

Therefore, this characteristic of any material reflects the nature of the atoms involved and serves as a correlation parameter with band structure and transport parameters.

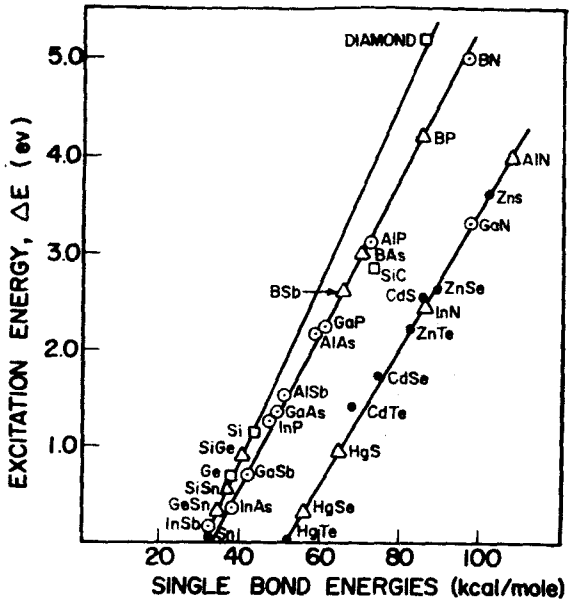

Fig. 10. Relationship of excitation energy, ΔE, in ev to single bond energy in kcal/mole. (After Gatos et al [26]).

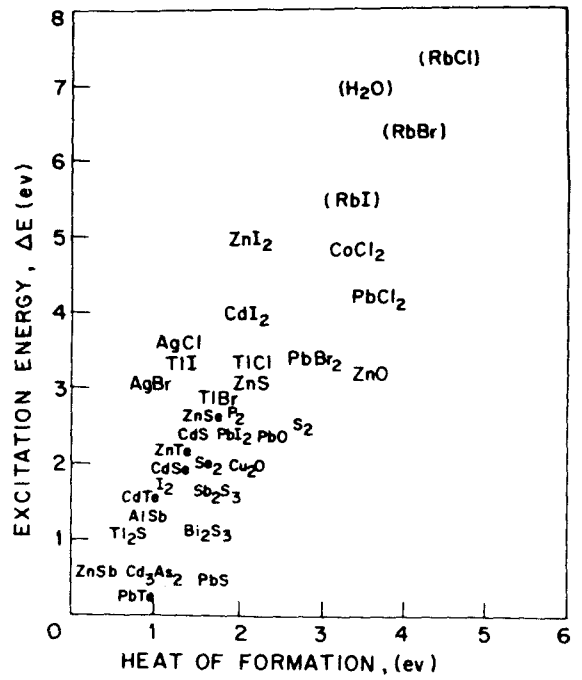

Fig. 11. Relationship between excitation energy, ΔE, in ev, and the heat of formation in ev (after Gatos et al [26]).

Bond Strength

In a more restricted sense, that is, among predominately covalent bonded materials, bond strength can be used as a correlation parameter. As shown in Table 5 the number of single covalent bonds made by an atom with nearest neighbor atoms is proportional to bond strength. Since both electron pair (full bond) and unpaired electron (half bond) bonds are known, the latter occurring along with variable strength resonance bonds, this variable is more qualitative but very significant.

Anisotropy Ratio $\frac{r_2}{r_1}$ of Interatomic Spacings

This parameter also has a limited application but is quite significant in regard to its degree of influence on band structure and transport properties.

The combination of the bond strength parameter and the anisotropy ratio parameter work together to impose major effects on the band structure and transport properties.

Application of Correlation Parameters

Electronegativity

Trends which are found in E_g, energy gap, μ_a, apparent mobility, $\bar{n}$, average principal quantum number among representative compound series as a function of the electronegativity difference parameter are shown respectively in Figures 12 and 13, 14 and 15, and 16 [27].

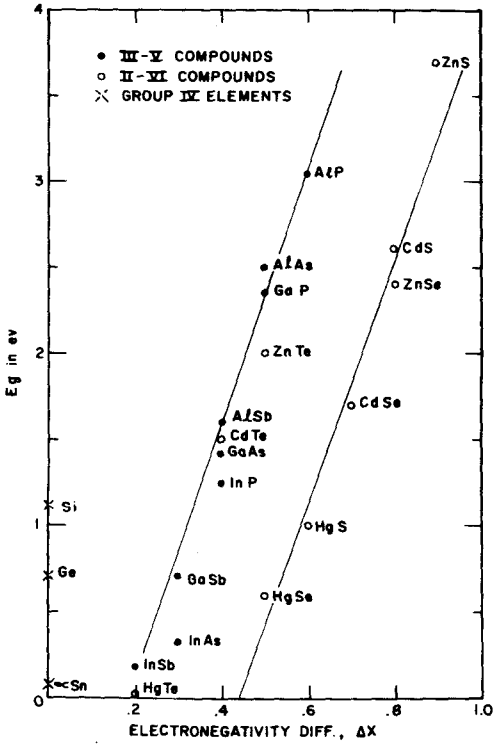

Fig. 12. Relationship of energy gap, E_g, to Electronegativity difference, ΔX, for Group IV elements and III-V and II-VI compounds.

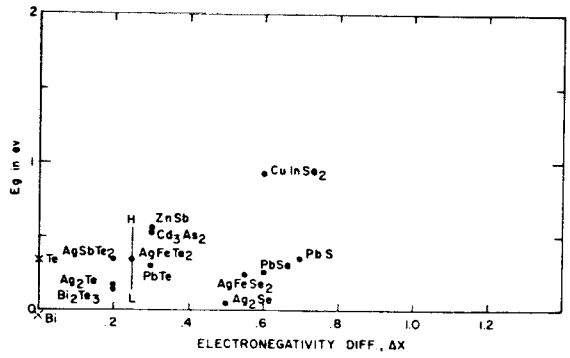

Fig. 13. E_g vs ΔX relationship for other compounds and elements.

Briefly these reveal the following. E_g increases with increasing ΔX in a linear fashion within any one series, III-V, II-VI, etc. Apparent charge carrier mobility generally decreases with increasing ΔX, beyond $\Delta X = .2$. However a definable peak value is reached at $\Delta X \cong .2$.

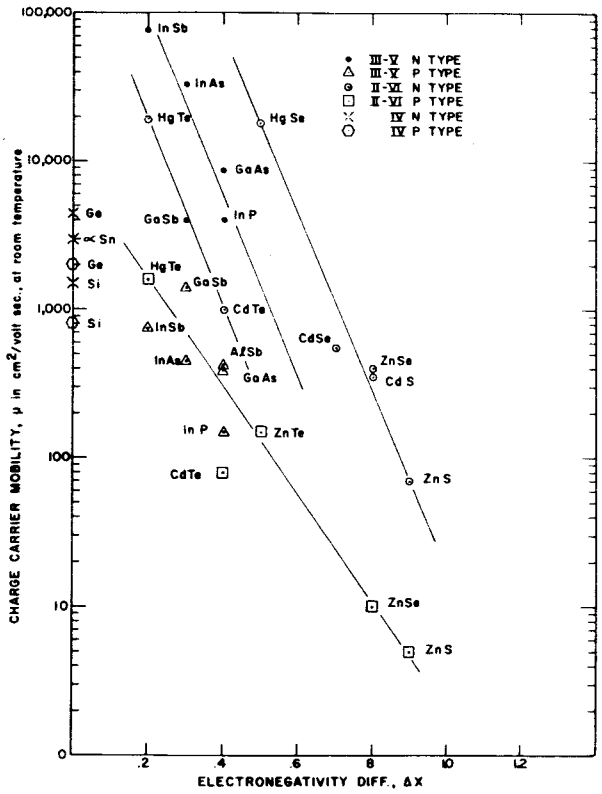

Fig. 14. Relationship of charge carrier mobility to electronegativity difference for Group IV elements and III-V and II-VI compounds.

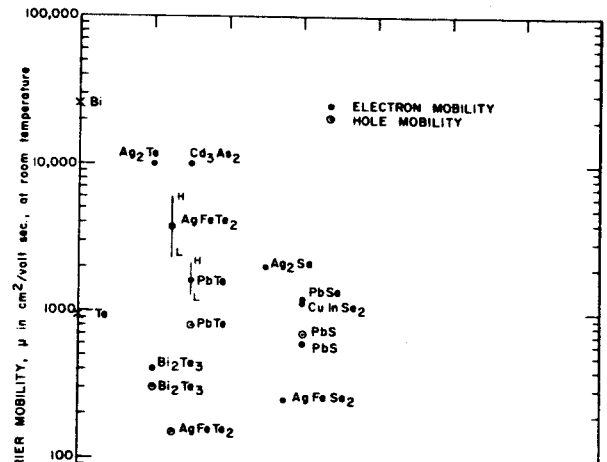

Fig. 15. Relationship of charge carrier mobility to electronegavity difference for other compounds.

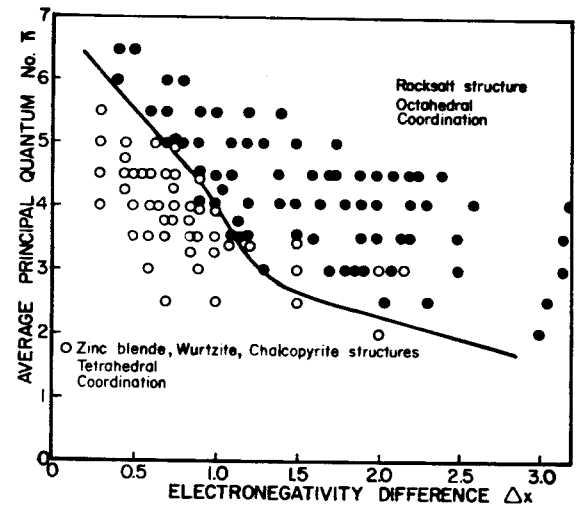

Fig. 16. Relationship of principal quantum number $\bar{n}$, to electronegativity, ΔX, for structures with cubic close-packed anion substructures and tetrahedral and octahedral coordination (after Mooser[28]).

Figure 17 shows the work function of the elements increases with increasing electronegativity X of the elements.

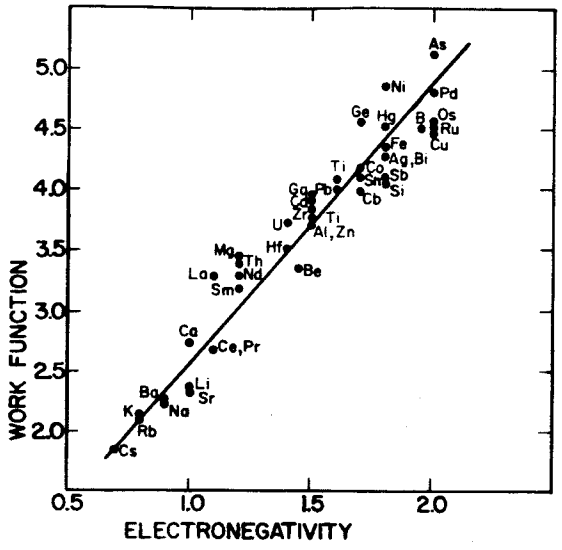

Fig. 17. Relationship between work function of elements and their electronegativity.

Ionicity Parameters

The electronegativity difference as a correlation parameter is not as revealing as the ionicity parameters λ, λ_o, and $\frac{e^*}{c}$. However, considering the problem in measuring $\frac{e^*}{c}$ and the limited validity of the "bond approximation" in calculating $\frac{e^*}{c}$, the degree of reliability which can be placed on the trends observed may be slightly less.

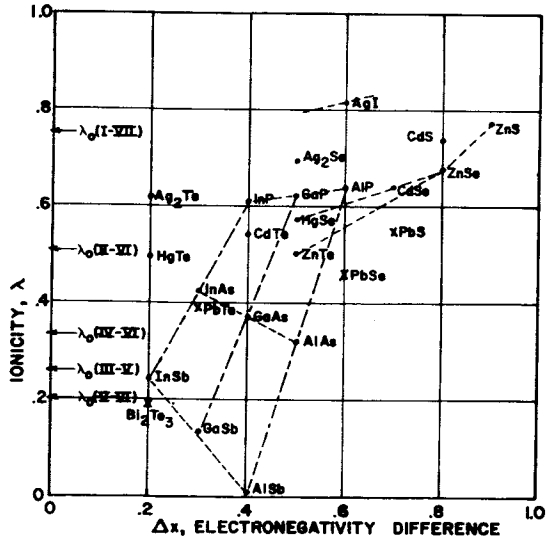

Fig. 18. Relationship of ionicity parameter, λ, and ΔX, for many compounds with different bond schemes.

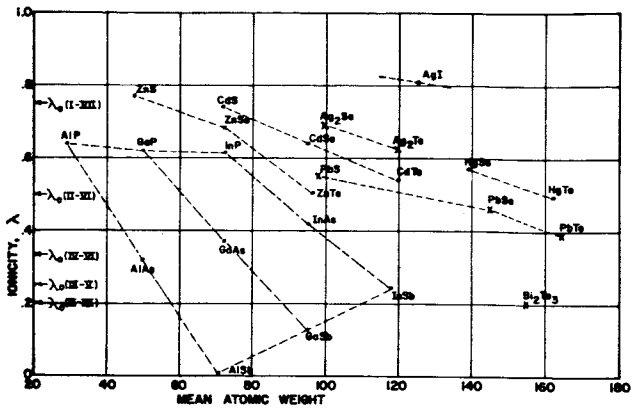

Fig. 19. Relationship of ionicity parameter, λ, and mean atomic weight for many compounds with different bond schemes.

In Figure 18 the correlation of the ionicity parameter, λ, with the electronegativity parameter, ΔX, is shown. This illustrates the relative influence of the λ_o, atomic ionicity, and $\frac{e^*}{c}$. In Figure 19, we note how λ and λ_o vary among various compounds with atomic weight. We note $\lambda - \lambda_o$ approaches zero for each series with increasing atomic weight.

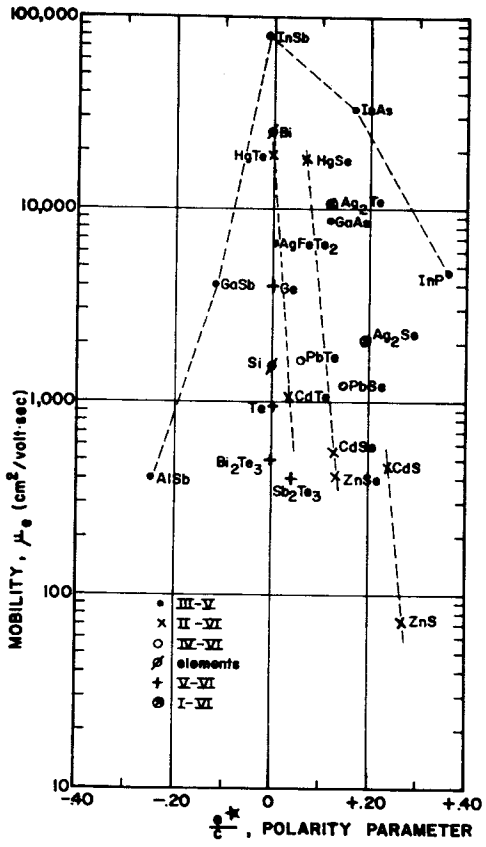

Fig. 20. Dependence of electron mobility on the polarity parameter, $\frac{e^*}{c}$ for elements and compounds with several types of bond schemes.

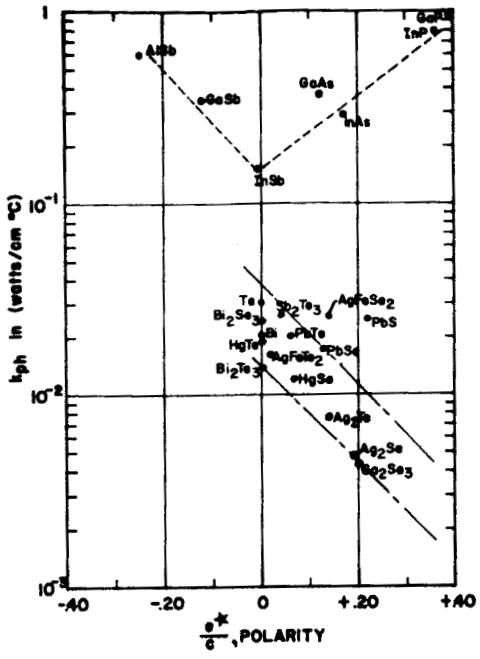

Fig. 21. Dependence of the lattice thermal conductivity on the polarity parameter, $\frac{e^*}{c}$, for elements and compounds with various bond schemes.

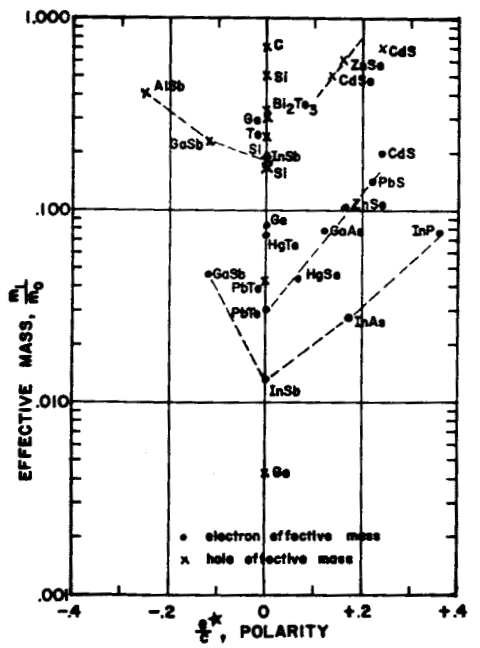

Fig. 22. Dependence of effective mass ratio, $\frac{m_1}{m_o}$, on the polarity parameter, $\frac{e^*}{c}$, for compounds and elements with various bond schemes.

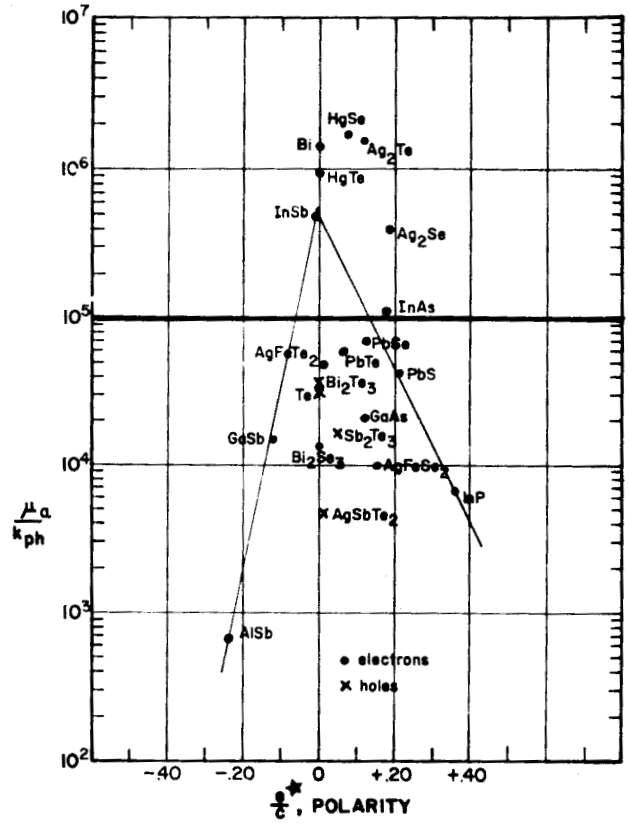

Fig. 23. Variation of $\frac{\mu_a}{k_{ph}}$ with the polarity parameter for compounds and elements representing various bond schemes.

Trends of μ_a, apparent mobility, k_{ph}, lattice thermal conductivity, effective mass ratio $\frac{m_1}{m_o}$, and $\frac{\mu_a}{k_{ph}}$, apparent mobility/thermal conductivity as a function of $\frac{e^*}{c}$ for representative groups of compounds are shown respectively in Figures 20, 21, 22 and 23.

The particular revelations obtained using this correlation parameter are the following

1. The highest electron mobility in any one compound group is observed at $\frac{e^*}{c}$ = 0, or zero effective ionicity of the bonds and this is found at the highest mean atomic weight.

2. The higher the atomic ionicity the lower the peak mobility reached and the more difficulty the specific compound series encounters in reaching $\frac{e^*}{c}$ = 0.

3. The lowest thermal conductivity is reached in the compounds with thelarg-

est atomic ionicity but lowest $\frac{e^*}{c}$, able to be reached as a function of increasing mean atomic weight and within the limits of stable crystal formation.

4. The density of states effective mass for electrons per conducting band within any one series of compounds or elements is lowest for that compound with $\frac{e^*}{c}$ closest to zero. There are other trends here but they are not meaningful because a relative consideration of all the effective mass values for the material has not been imposed in making this plot.

5. The highest $\frac{\mu_a}{k_{ph}}$ for electrons is achieved at $\frac{e^*}{c} = 0$ and a medium value of atomic ionicity, λ_o, for the highest mean atomic weight compounds characterized by this value of λ_o.

Mean Atomic Weight and Anisotropy Ratio $\frac{r_2}{r_1}$

Trends found between E_g, energy gap, μ_a, apparent mobility, k_{ph}, lattice thermal conductivity and $\frac{r_2}{r_1}$, the anisotropy ratio, and the mean atomic weight for a representative compound series are revealed respectively in Figures 24 and 25, 26 and 27, 28, and 7 [27].

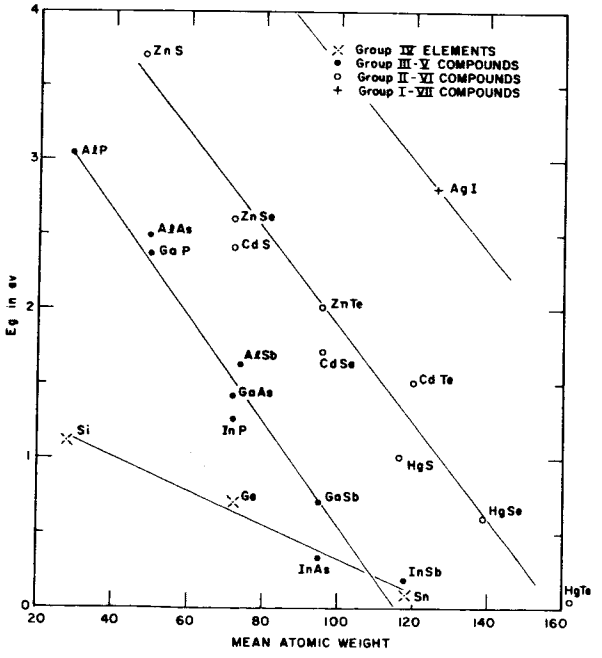

Fig. 24. Relationship between energy gap, E_g, and mean atomic weights for Group IV elements and Group III-V, and II-VI Compounds.

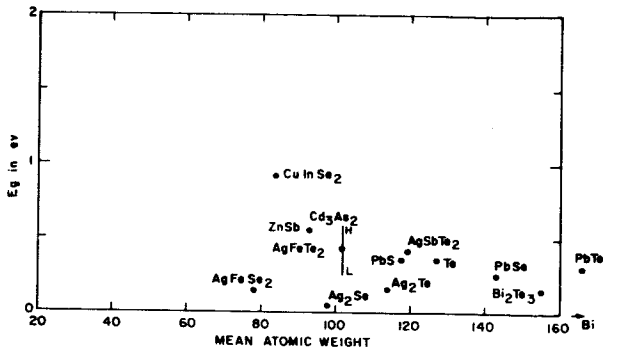

Fig. 25. E_g vs mean atomic weight for other compounds and elements.

Figures 24 and 25 reveal that E_g decreases with increasing atomic weight more or less uniformly within one compound series (except in the case of structure and bonding changes); with those series having higher λ_o, atomic ionicity, starting at larger energy gaps and decreasing at the same rate as those with lower λ_o. Within the limits of the atomic table, the II-VI and I-VI groups represent materials with highest λ_o that reach $E_g \approx 0$ at the highest mean atomic weights.

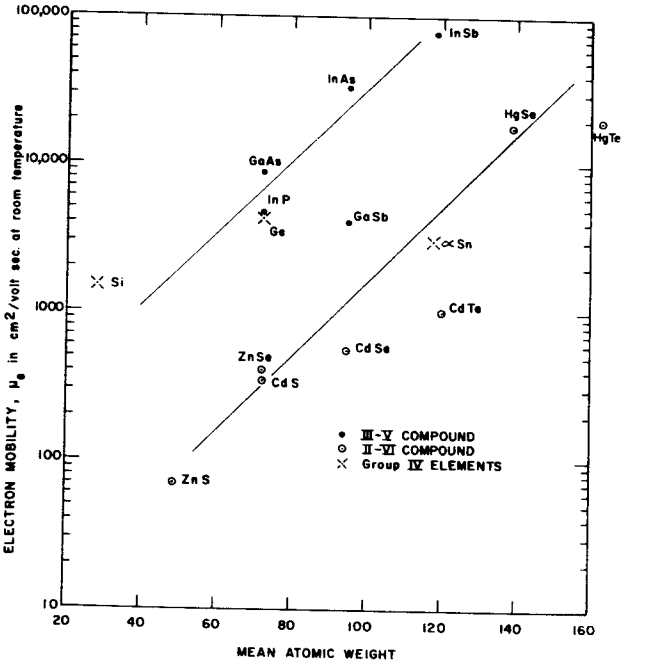

Fig. 26. Relationship of electron mobility to mean atomic weight for Group IV elements and Group III-V and II-VI compounds.

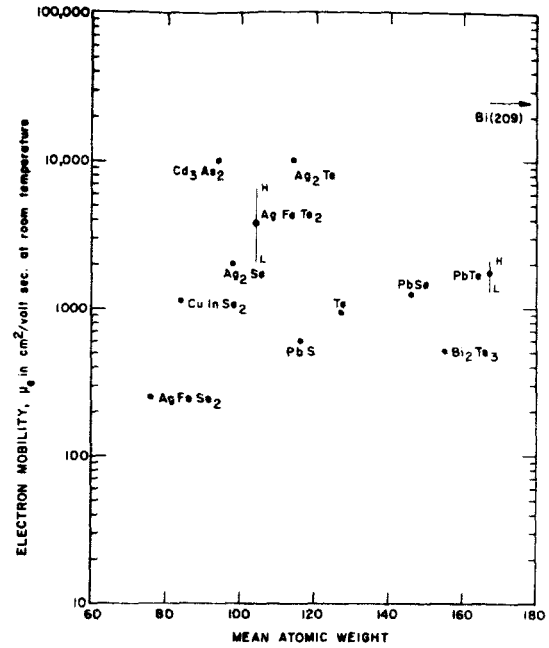

Fig. 27. Relationship of electron mobility to mean atomic weight for other elements and compounds.

Figures 26 and 27 indicate that electron mobility increases with mean atomic weight in each compound series. The higher the λ_o, characterizing the series, the lower the mobility reached at maximum mean atomic weight.

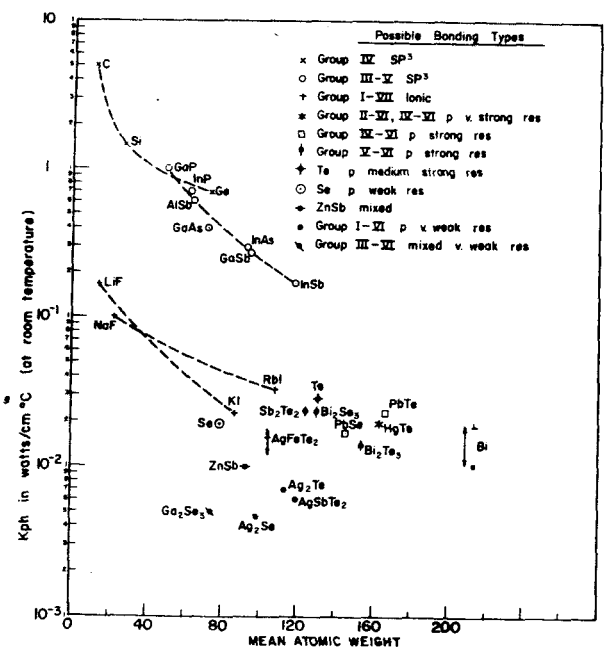

Fig. 28. The lattice thermal conductivity of selected compounds and elements as a function of mean atomic weight and classification of chemical bonds.

Figure 28 shows that k_{ph} the thermal conductivity, decreases with increasing atomic weight within any one compound series characterized by a specific value of λ_o, with the lowest k_{ph} found in the compound having the combination of the highest λ_o and highest mean atomic weight possibly reached within the limits of the atomic table.

Figure 7 reveals that the anisotropy ratio $\frac{r_2}{r_1}$ common to certain II, V, and VI group elements decreases within the latter two groups with increasing atomic weight and remains constant for Group II. This parameter can impose a modifying effect on how E_g, the energy gap changes with increasing atomic weight. Specifically it induces a band structure modification which induces an $E_g \neq 0$ in elements such as Bi of highest atomic weight. Table 9 shows the effect of the anisotropy ratio on the anisotropy of thermoelectric power, S_e and S_p, for II and V group elements and II-V compounds[29].

TABLE 9

COEFFICIENTS OF THERMO-EMF FOR ANISOTROPIC SUBSTANCES (after Gitsu et al[29])

Substance		t, °C	S ∥ μv/deg.	S⊥ μv/deg.	
		Metals			
Zn		0	+0.42	+2.16	
Cd		0	-0.04	+3.16	
Hg		-76	-2.2	-4.5	
		Semimetals			
Bi		18	-96.6	-58.0	
Sb		0	+20.6	+46.8	
		Semi-conductors	S_{11}	S_{33}	S_{22}
CdSb	Region of intrinsic conductivity	127	+75	-8	+190
	Region of impurity conductivity	-23	770	770	770
		-160	700	675	700

Bond Strength

The influence of decreasing bond strength and types of bonds on the lattice thermal conductivity is qualitatively shown in Figure 29. It should be noted that this trend also embodies in some cases, such as Bi and ZnSb, the effect of the anisotropy ratio, $\frac{r_2}{r_1}$, which introduces an anisotropy of bond strength.

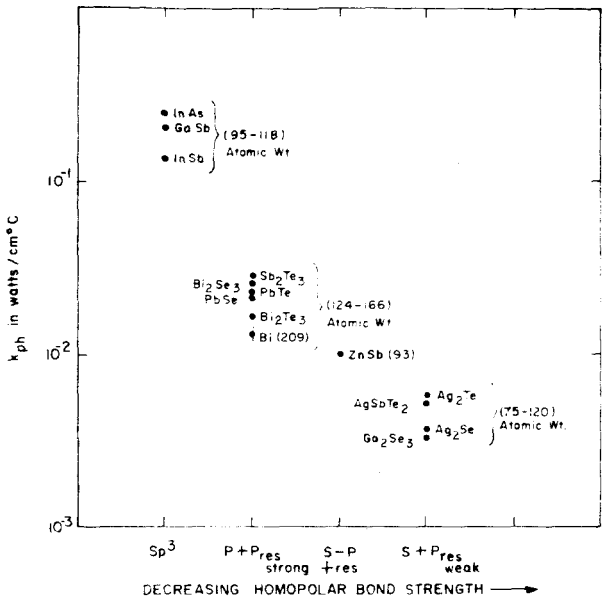

Fig. 29. Variation of k_{ph} with bond type for binary compounds with various mean atomic weights.

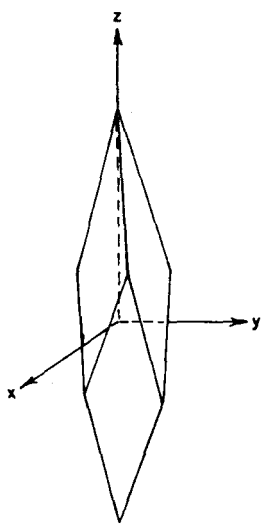

Fig. 30. The rhombohedral unit cell of the bismuth telluride lattice.

AN INTERDISCIPLINARY IDENTIFICATION OF Bi_2Te_3

To proceed any further on the problem of attempting to (1) predict higher Z materials and (2) selecting worthy materials systems for experimental study, an attempt at an interdisciplinary identification of what combination of factors allows the high Z values in the best available materials for the temperature range from 50 to 573°K is now necessary.

Crystal Structure

The crystal structure of Bi_2Te_3 was first reported by Lange[30]. The crystal has a trigonal lattice and therefore a rhombohedral unit cell. (See Figure 30). It can be described by one chemical formula and the space group is D_{3d}^5-R-3m.

If the axis of threefold symmetry is taken to be the z axis, the lattice can be described in terms of three primitive translations which make equal angles with this axis and with each other. These translations can be written

$$\vec{t}_1 = s\vec{j} + r\vec{k}$$

$$t_2 = \frac{1}{2}\sqrt{3}\ \vec{si} - \frac{1}{2}\ \vec{sj} + \vec{rk} \qquad 41)$$

$$t_3 = \frac{1}{2}\sqrt{3}\ \vec{si} - \frac{1}{2}\ \vec{sj} + \vec{rk}$$

where r = 10.18 A° and s = 2.53 A° and i, j, and k are unit vectors along the x, y, z axes respectively.

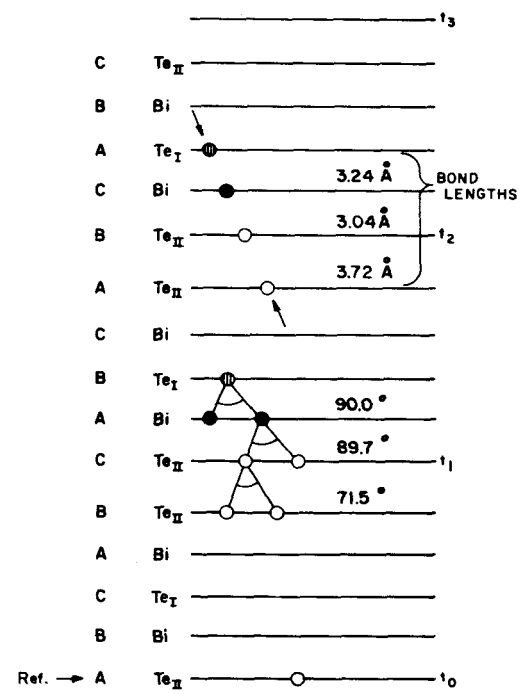

Fig. 31. Layer lattice arrangement in Bi_2Te_3 showing direction of bonding (⟶ ⟵).

The arrangement of the atoms in the lattice is a layered one stacked as CBA, CBA, CBA,

CBA, CBA, as shown in Figure 31. The layers are not quite equidistant. Taking the Te atom marked as reference in Figure 31 any one of the primitive translations takes one 5 layers up before an equivalent Te atom is encountered. However it is only in the 15th layer, that is, at the point $t_1 + t_2 + t_3$ from the original Te atom that one on the Z axis is encountered. These are the operations of the $R\bar{3}m$ space group.

Because repetition of Te on the Z axis occurs only after three translations, there are three axes of twofold symmetry and three reflection planes.

These symmetry operations of the Bi_2Te_3 lattice are summarized below

Translations: $lt_1 + mt_2 + nt_3$; l, m, n integers
Identity: E
Rotation about the Z axis to the left or to the right by $2/3\ \pi\ (120^\circ)$: $2C_3$
Reflection in any one of the three planes of symmetry containing the Z axis: $3\sigma_v$
Inversion I
Rotation of $1/3\ \pi\ (60^\circ)$ about Z axis followed by reflection in a plane perpendicular to the Z axis: $2S_6$
Rotation of 180° about any one of the three axes of two fold symmetry: $3C_2$

The effect of the rotations and reflections is summarized in Table 10. They are the operations of the point group D_{3d}^5. Neither glide planes nor screw axes are contained in these operations.

TABLE 10

EFFECT OF SYMMETRY OPERATIONS

Operation	Sends into	x	y	z
E		x	y	z
$2C_3$		$-1/2x-1/2\sqrt{3}y$	$-1/2y+1/2\sqrt{3}x$	z
		$-1/2x+1/2\sqrt{3}y$	$-1/2y-1/2\sqrt{3}x$	z
$3\sigma_v$		-x	+y	z
		$+1/2x+1/2\sqrt{3}y$	$-1/2y+1/2\sqrt{3}x$	z
		$+1/2x-1/2\sqrt{3}y$	$-1/2y-1/2\sqrt{3}x$	z
I		-x	-y	-z
$2S_6$		$1/2x+1/2\sqrt{3}y$	$1/2y-1/2\sqrt{3}x$	-z
		$1/2x-1/2\sqrt{3}y$	$1/2y+1/2\sqrt{3}x$	-z
$3C_2'$		x	-y	-z
		$-1/2x+1/2\sqrt{3}y$	$+1/2y+1/2\sqrt{3}x$	-z
		$-1/2x-1/2\sqrt{3}y$	$+1/2y-1/2\sqrt{3}x$	-z

By transformation of the axes, the unit cell can also be given alternatively as a hexagonal unit with three chemical formulae and $a_{hex} = 4.38$ and $c_{hex} = 30.497\ A^\circ$.

In the structure, the Te_{II} atom has three Bi atoms as nearest neighbors on one side and three Te atoms on the other side while the Te_I atom is surrounded by 6 Bi atoms; that is, two essentially different sites exist for Te atoms.

The shortest spacings between the Bi and Te planes of the structure are:

$$Te_{II} - Te_{II} = 2.63\ A^\circ$$
$$Te_{II} - Bi = 1.70\ A^\circ$$
$$Bi - Te_I = 2.03\ A^\circ$$

These are repeated in proceeding from the Te_I atom to the cleavage bond ($Te_{II} - Te_{II}$) in the other direction.

The a_{hex} lattice constant = $4.38\ A^\circ$ measures the distance between Bi atoms in Bi planes and Te atoms in Te planes.

The interatomic spacings between atoms in different layers are

$$Te_{II} - Te_{II} = 3.72\ A^\circ$$
$$Te_{II} - Bi = 3.04\ A^\circ$$
$$Bi - Te_1 = 3.24\ A^\circ$$

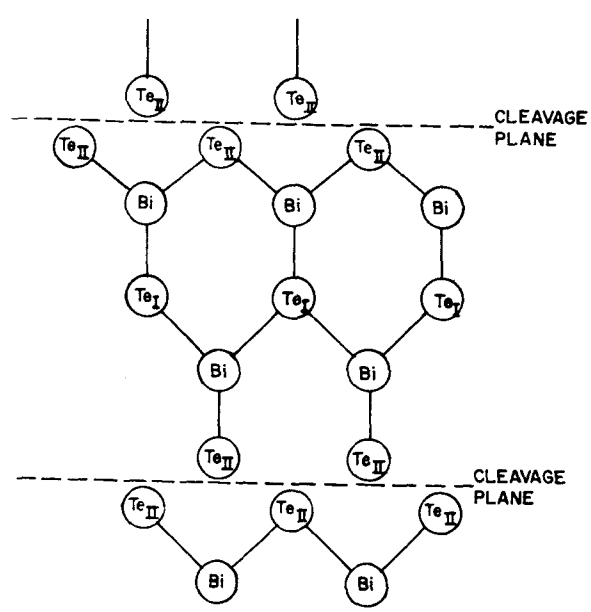

Fig. 32. Pictorial representation in two dimensions of the type of molecular building blocks in a Bi_2Te_3 crystal.

Chemical Bonding

The bonding angles, as illustrated in Figure 31, are approximately 90^{o} within the molecule but approximately 71^{o} between the molecular layers.

The bonding direction is in the direction as shown in Figure 31. Because of the lattice structure, there are three such bonding directions at 120^{o} apart about the c_{hex} axis. Figure 32 attempts a not-to-scale two dimensional representation of the molecular chains showing two bonding directions (at 180^{o} apart rather than the actual 120^{o} apart).

As shown by the fact that the bonding angles between atoms within the planes (Figure 31) are approximately 90^{o}, one expects primarily p orbital bonding (See Table 5) to be present. Further an assay of the atomic table (See Table 6) and consideration of the ionization potentials of the elements reveals that both Bi and Te are categorized as elements in the "inert pair" group. That is, they do not use their outermost s electrons in chemical bonding. As ionization potential tables show, the fourth and fifth ionization potentials attributed to these electrons of Bi, and the fifth and sixth for Te, have a much greater ev separation than the first 3 potentials attributed to the 3 p orbital electrons in Bi and 4 in Te. The ev difference between ionization potentials I and II and II and III, etc are about equal in both Bi and Te.

Qualitatively, it can be concluded that only p orbitals are used in bonding in Bi_2Te_3. Because the bond angles are $\sim 90^{o}$, the bonding is covalent. However, because the bond angles between Te_I-Bi, Bi-Te_{II} are slightly different, the latter having a bond angle slightly less than 90^{o} and the Te_{II}-Te_{II} bond angle is considerably different than 90^{o} ($\sim 71.^{o}$), one expects from considerations of the bond approximation theory and the principles of resonance bonding[16] that the electron distribution between Te_I-Bi is centered between the atoms, ($E_{ion} \approx 0$), while between Bi-Te_{II} the $E_{ion} \neq 0$. However, with due consideration to the large polarizibility of the Bi atom, it is expected that $E_{ion} \neq 0$ is compensated by $E_{cov.-res.}$ so actually the ionicity $\frac{e^*}{c}$ is equal to zero and the valence electron distribution between Bi-Te_I is polarization adjusted so as to maximize itself at the center between the atoms and spread out in the plane bisecting the binding between atoms.

The bond angle between Te_{II}-Te_{II} suggests a bond strength considerably greater than that of a Van der Waals bond. The three unsatisfied Te_{II} orbitals (See Figure 31) form nearly metallic resonance bonds with other Te_{II} atoms across the cleavage plane. Considerable distortion in the electron distribution between these atoms is expected.

However, in terms of the resonance bonding principles, 6 electrons are shared between 5 quantum states associated with 5 atoms in the 5 layers along each bonding line shown in Figure 31. Three equally probable resonance situations are pictured in Figure 33[20].

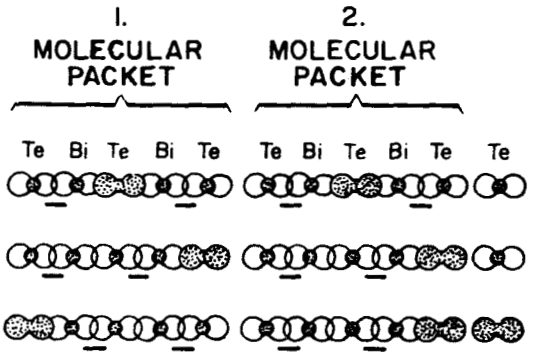

Fig. 33. Three equally probably resonance situations in Bi_2Te_3 (after Krebs[20]).

Band Structure Generation And Band Structure Determinations

In order to determine the band structure, the reciprocal lattice for the Bi_2Te_3 must be determined from the lattice structure definitions.

Carrying out this step, Lee and Pincherle[31] show that the reciprocal lattice is defined by the vectors

$$k_1 = 2\pi\left(\frac{2}{3s}\vec{j} + \frac{1}{3r}\vec{k}\right)$$

$$k_2 = 2\pi\left(\frac{1}{\sqrt{3}s}\vec{i} - \frac{1}{3s}\vec{j} + \frac{1}{3r}\vec{k}\right) \quad 42)$$

$$k_3 = 2\pi\left(-\frac{1}{\sqrt{3}s}\vec{i} - \frac{1}{3s}\vec{j} + \frac{1}{3r}\vec{k}\right)$$

These three vectors in k space, like the corresponding ones in the actual lattice, make equal angles with each other and with the z axis. In this case, however, the angles with the z axis are large while those in the actual lattice are small.

The first Brillouin zone is constructed from planes normally bisecting the first few reciprocal lattice vectors. This is pictured in Figure 34. The boundary planes above and below are those bisecting the vectors $\pm(\vec{k}_1 + \vec{k}_2 + \vec{k}_3)$; their faces are regular hexagons. The other six-sided faces

are perpendicular bisectors of the veetors $\pm\vec{k}_1$, $\pm\vec{k}_2$, and $\pm\vec{k}_3$. The remaining six four sided faces are determined by the vectors $\pm(k_1 + k_2)$, $\pm(k_2 + k_3)$, and $\pm(k_3 + k_1)$.

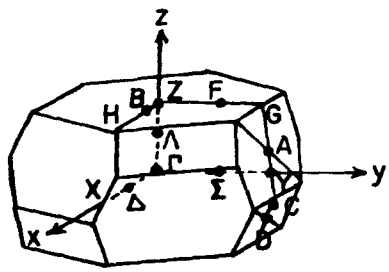

Fig. 34. Brillouin zone of bismuth telluride (after Lee and Pincherle [31]).

The faces of the surfaces correspond to actual crystallographic directions.

Since the region lying between the successive (such as the first and second) polyhedra in k space is known as the Brillouin zone; the relationship of the polyhedra are such that each Brillouin zone occupies the same volume of k space. This volume is sufficient to accomodate 2 N electron states where N is the total number of atoms in the crystal.

That each Brillouin zone should contain two states (one of each spin choice) for every atom is expected since the band system of a solid arises naturally from the direct energy levels of an isolated atom. Each electron-energy level becomes broadened through interaction between the closely spaced atoms of a solid in such a way that the energy range of a band is independent of the number of the atoms in the crystal but depends on their interatomic spacing and on the energy level from which the band arose.

In a real crystal where N is very large the 2N states in each band are exceedingly closely spaced in energy but the distribution of states in energy is still the same.

Considering the nature of the electron shell structure of atoms, one expects to see one zone arising from s valence states, 3 for p valence states and 5 zones for d valence states.

Electrons in the valence states belong to the crystal as a whole, rather than being identifiable with any one atom. These are the ones which can be involved in bonding and determine therefore the crystal structure.

When two such zones overlap, a band containing four N states arises. Considering the interatomic spacing of a silicon crystal and the 4 valence electrons (sp^3 hybrid bond), a certain periodic potential (found to fit this material) arises. It is found that the eight electron states (2 for each orbital and 2 in each of 4 electron-pair bonds) divides into a band of 4N states then a gap and an upperband containing 4 N states.

Returning to the Bi_2Te_3 reciprocal lattice and Brillouin zone shown in Figure 34, the electronic energy levels at any reciprocal lattice point $\vec{k}$ are classified according to the irreducible representations of the group of $\vec{k}$. The conventional notations for points and lines of symmetry in the Brillouin zone are given in Figure 34. Table II lists the symmetry operations for the corresponding k vectors, and the sub-group for these vectors.

TABLE II

POINT GROUPS OR PROMINENT POINTS AND LINES IN THE BRILLOUIN ZONE

Point or line	Symmetry Operations	Group
Γ, Z	full point group	D_{3d}
Δ, B, X, H	E, C_2'	C_2
Σ, F, G	E, σ_v	C_s
Λ	$E, 2C_3, 3\sigma_v$	C_{3v}
A, D	E, C_2', σ_v, I	C_{2h}

The free electron levels are given by

$$E_n = (\vec{k} + \vec{K}_n)^2$$

where

$$K_n = l\vec{k}_1 + m\vec{k}_2 + n\vec{k}_2$$

with l, m, n, positive or negative integers or zero.

Lee and Pincherle [31] have shown that considering the 28 electrons available (s and p outside the closed shells of the five atoms in the unit cell), then 14 non-degenerate bands must be filled at each k point and the top of the valence band and bottom of the conduction band traced throughout the zone (for nearly free electrons-small splitting case) would agree with a six valley model for the conduction band and a three valley one for the valence band.

DEVELOPMENT OF AN INTERDISCIPLINARY MODEL (IMWM) FOR Bi_2Te_3

The band structure characterizing Bi_2Te_3 crystals can be generated from its reciprocal lattice. Lee and Pincherle[31] have attempted this, as discussed in the last section. They started with the five atom molecular unit cell and by translation operations generated the rhombohedral unit cell from the three molecular unit cells characterizing the alternate hexagonal structure representation.

In view of the concepts of molecular resonance bonding and this type of characterization for Bi_2Te_3, the expectation that one molecular unit will resonate with the other two and produce new energy bands from those characteristic of each molecular unit requires consideration. Thus, it is necessary to impose an anisotropy parameter (perhaps as a psuedo-potential).

Lee and Pincherle[31] considered 28 electrons around 5 atoms of the molecular unit cell. In view of bonding data on Bi_2Te_3 only the 18 p-orbital electrons need be considered.

We now distinguish between individual groups of six of these electrons in the translation operations in generating the crystal structure. By tagging each atom of each molecular unit (e. g. consider one in each molecule, $-Bi_I^{1p}$, Bi_{II}^{2p}, Bi_{III}^{3p}), we note on completion of the translation operation that 3 p orbital electrons at one Bi position in the generated rhombohedral cell are from three Bi atoms; one from each of the three molecules. The same is true for the other four atoms. We note there are three p orbital electrons contributed by the 3 Te_I positions in the three molecules which are not yet accounted for. These effectively tend to fill up the bands generated by the p orbital half bonds.

These relationships allow treating each of the three p-orbital electrons of a Bi atom in the generated crystal structure as involved in independent bands of the band structure.

From bonding information we know the bonds made by Bi and Te in the Bi_2Te_3 structure are p-orbital half bonds. We interpret this as meaning the 6 bands generated in the crystal by the 6 p-orbital half bonds per Bi site are approximately half full. Since there are two Bi sites per molecule and three molecules represented in the rhombohedral cell, we expect that there will be six separate sources or "wells". Each well joins with all other like wells in the resonance bonded structure in developing valence and conduction bands.

Considering the whole crystal we can now concentrate our attention on the valence and conduction bands associated with all the wells, like one well of the six in the rhombohedral unit cell.

Considering each well in this framework, Figures 35 and 36 present, respectively, interdisciplinary correlation models for Bi_2Te_3 and Bi crystals.

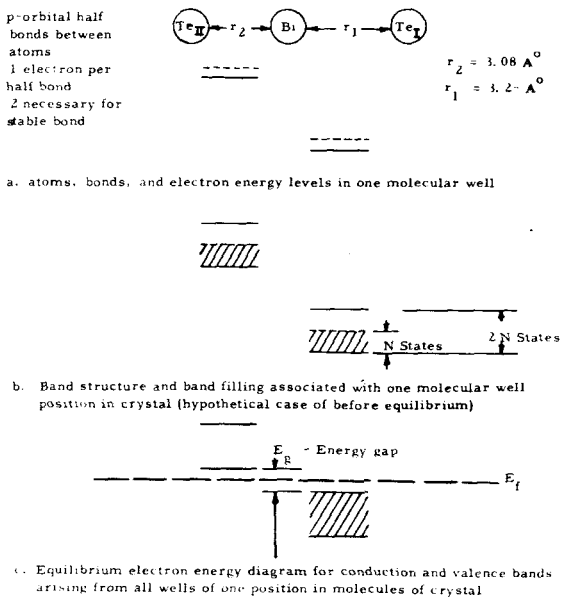

a. atoms, bonds, and electron energy levels in one molecular well

b. Band structure and band filling associated with one molecular well position in crystal (hypothetical case of before equilibrium)

c. Equilibrium electron energy diagram for conduction and valence bands arising from all wells of one position in molecules of crystal

Fig. 35. IMWM (Inderdisciplinary Molecular Well Model) for Bi_2Te_3.

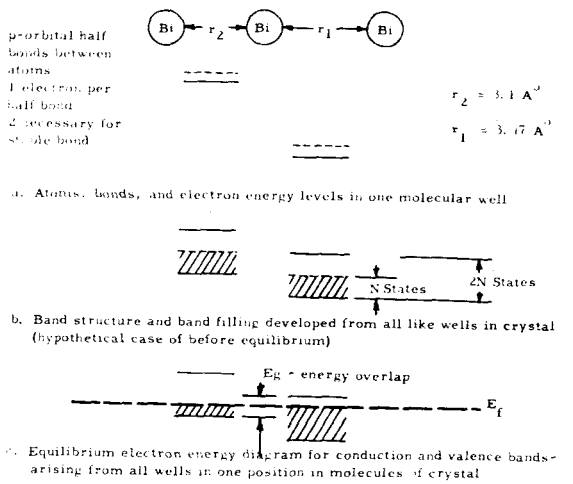

a. Atoms, bonds, and electron energy levels in one molecular well

b. Band structure and band filling developed from all like wells in crystal (hypothetical case of before equilibrium)

c. Equilibrium electron energy diagram for conduction and valence bands arising from all wells in one position in molecules of crystal

Fig. 36. IMWM (Interdisciplinary Molecular Well Model) for Bi.

In Figure 35a, the atom placements in a molecule, bond lengths and electron energy levels are shown.

In Figure 35b, the energy band structure

which develops from each of these bonds in the crystal is pictured in a hypothetical situation before equilibrium. We note each band associated with each bond has 2 N states with only N states full.

In Figure 35c, the actual case after equilibrium, is shown. We note E_f, the Fermi level lies between the top of the filled band associated with the Bi-Te_I and below that associated with Te_{II}-Bi. The electrons in the band associated with Te_{II}-Bi have emptied into the states in the band associated with Bi-Te_I. The separation between the position of the empty band and the top of the filled band determines the energy gap, E_g, for the crystal due to this well.

These models are named interdisciplinary molecular well models. (IMWM)*.

In Figures 36a, b, and c, the IMWM* for a Bi crystal is similarly presented.

We note here an overlap of the bands which result in simultaneous electron conduction in the band to the left and hole conduction in the band to the right.

Considering Bi_2Te_3 in Figure 35a, the p-orbital bonds between Te_{II}-Bi and Bi-Te_I for one molecule represent one well. The other end of each molecule can be similarly represented. As indicated, the Te_{II}-Bi bond has a length r_2 and Bi-Te_I a length r_1. As shown in Figure 31, $\frac{r_1}{r_2} = 1.05$. Each of the bonds contains one electron. Together they act as a pair to provide a chemically stable electron-pair bond. However, each of these half bonds is spatially separated from the other in the structure. As indicated by the dotted and filled lines, one orbital in each bond is not filled. Because the relative energies of the Te_{II} and Te_I positions in the molecule are different, the Te_I position having a higher bonding energy, and because $r_2 < r_1$, the relative energy levels of the electrons in the two bonds are separated as shown (Note these relative energy placements follow the same energy direction as for the band structure).

If an electron is missing in the Bi_2Te_3 well system, the crystal acts as a hole conductor. If there is an excess electron in the well system, the crystal acts as an electron conductor. Thus the presence of an excess or deficiency of electrons in the well determines in which of the two bands there are charge carriers.

The resonance bonding between the ends of the molecules and polarization overlap between the sides of the molecular chains provides the necessary coupling of the individual wells, (two of them per molecule) so wave functions characterizing the electrons or holes in the wells will interact to form bands throughout the crystal.

The geometrical nature and orientation of the constant energy surfaces of the conduction and valence bands will be a direct function of the anisotropy of the Te_{II}-Bi and Bi-Te_I lattice spacings and the relative bonding energies of the Te_{II} and Te_I in the molecular structure.

Data accumulated on "anti-structure" of Bi_2Te_3 and effects of substitutions in the Bi and Te sublattices on transport properties suggest that substitutions in the Te sublattice, which result in providing excess electrons, fill up the valence band and introduce electrons into the conduction band. Likewise substitutions in the Bi sublattice which give a deficiency of electrons in the well result in hole conduction in the valence band. Investigators[32] interpret their data on thermal and electrical conductivity, as a function of such substitutions, as indicating electrons flow in the Bi sublattice and holes in the Te sublattice. In view of the molecular well model, these observations and conclusions can be understood since the electron conduction bands are associated with the 6 independent Te_{II}-Bi bonds and the valence bands with the 6 independent Bi-Te_I bonds.

Because of the greater ionicity of the Bi-Te_I bond compared to that of the Te_{II}-Bi bond, the hole mobility will be less than the electron mobility. Therefore, substitutions in the lattice which change the relative bond ionicities will be expected to cause a change in the $\frac{\mu_e}{\mu_p}$ ratio. Further, the intimate relationship between the Te_{II}-Te_{II}, Te_{II}-Bi and Bi-Te_I bonds is expected to result in simultaneous changes of $\frac{\mu_e}{\mu_p}$, E_g and μ dependency on temperature.

For the Bi_2Te_3 crystal, the IMWM predicts 6 independently acting conduction bands and a similiar number of valence bands due to the 6 independent wells. Further, because of the requirements for resonance bonding and the identical structure of each of the six wells, the 6 conduction bands will have isoenergy extrema and likewise the 6 valence bonds will have isoenergy extrema. This means the Fermi level will be characteristic of any one of the 6 independent wells (relative to the states in the valence band if it is conducting, and conduction band, if it is active).

* IMWM will be used from here on as an abbreviation for Interdisciplinary Molecular Well Model.

Support for the Model

The IMWM is not inconsistent with deductions by Drabble, et al.[33-35] from their galvanomagnetic coefficient determinations on Bi_2Te_3. Drabble, et. al[33-35], deduced from their data that the conduction and valence bands might be characterized by six ellipsoidal isoenergetic surfaces centered in the reflection planes perpendicular to the binary axes as shown in Figure 37. As noted there, they placed these surfaces inclined at an angle θ with the cleavage plane. They also found that the ratio of effective masses was different for the conduction and valence bands.

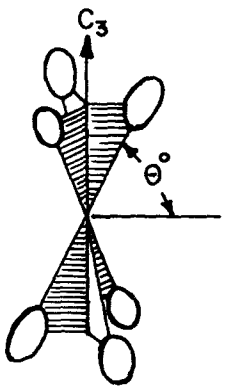

Fig. 37. The 6 ellipsoid energy surface positions in the crystal system for Bi_2Te_3 (θ is the angle with the cleavage plane; C_3 is the trigonal axis) (after Efimova et al[37]).

Efimova's[36-37] further examination of galvanomagnetic properties of Bi_2Te_3 also gives results quite compatible with the IMWM. Efimova[36-37] found he could:

1. describe the energy spectrum by a six valley model.
2. assign two regions of scattering-one for isotropic thermal scattering and one for anisotropic impurity scattering.
3. fit her values of galvanomagnetic coefficients to <u>two sets of</u> characterisitcs of energy spectra of each band corresponding to <u>two variations of a six valley model</u>.
4. almost exactly correlate the two sets of conduction band characteristics with the two sets of valence band characteristics.

It is proposed that Efimova's two sets of characteristics for the energy spectra are directly related to the valence band-conduction band structure associated with each of the wells.

If one spatially represents the 6 "well" positions in the coordinate system of a Bi_2Te_3 crystal cell and then compares their geometrical locations with those of the ellipsoidal isoenergy surfaces in Figure 37, it is noted that ellipsoids and wells have the same locations. We further note that the axis of each double well will be the resonance bonding direction. By comparison then, we place the axes of ellipsoid pairs and well pairs on the binary axes of the crystal.

Carrying this correlation further, the nature of the conduction and valence bands associated with each well at these positions corresponds with the placement of Efimova[36] of both conduction band and valence band ellipsoids at the same positions.

Using this correlation we can then assign different effective masses, determined by Drabble et al[33-35], to the valence and conduction bands associated with each well.

In this way we can interpolate that the mobilities related to these effective masses are determined by the relative lattice spacings of Te_{II}-Bi and Bi-Te_{II}.

Further the resonance bond strength between Te_{II}-Te_{II} is expected to be variable with temperature in a direction such that relaxation will occur with increasing temperature. This bond however directly controls the anisotropy of the Te_{II}-Bi and Bi-Te_{I} lattice spacings and the polarization overlap in the Bi planes and Te planes. Since the energy gap and by association the anisotropy of the mobilities of charge carriers in the conduction and valence bands are controlled by the anisotropy of the lattice spacings it is to be expected that with increasing temperature, the observed mobility of charge carriers will not follow a $T^{-\frac{3}{2}}$ acoustic scattering law expected for all resonance bonded crystals.

Rather, it is expected that a superimposed dependency of mobility of $\sim T^{-\frac{3}{2}}$ due to the relaxation of the resonance bond with increasing temperature, which causes the characteristic mobilities of the two bands to approach one another, will be observed.

Since only one band is active when the Bi_2Te_3 is conducting via one charge carrier, we therefore may expect that

$$\mu \alpha T^{\simeq 3}$$

As the literature reveals[6], this is the type of dependency which has been observed for Bi_2Te_3, Bi, and PbTe when impurity scattering was minimized.

Application of the Interdisciplinary Molecular Well Model (IMWM)

In considering transport properties and thermoelectric properties of Bi_2Te_3, according to this model, equations representing the current flow should be set up which take account of the oblateness and prolateness of the ellipsoidal energy surfaces and the angle of the axes of the ellipsoids with the direction of current flow. For the present an approximation will be made, since the angle θ with the cleavage plane is rather large for each ellipsoid.

With current flowing in the cleavage plane we expect that all six independent wells will contribute charge carriers in an additive sense so the total number of charge carriers will be observed via Hall constant measurement.

Since the Fermi-level is established in each system of wells and is common for all well systems, it is expected that the nature of the electron distribution (whether degenerate or non-degenerate) will be determined by the charge carrier density characterizing each well system at a given temperature.

Likewise we expect the influence of the degree of degeneracy of the electron distribution on the mobility of the charge carriers will be determined on an individual well system basis.

Consequently the approximate transport and thermoelectric property equations for use in roughly interpreting experimental data are:

$$R_{H_T} = \frac{1}{6n_i e} \qquad 43)$$

where

n_i = number of charge carriers/ well system

$$\sigma_T = (n_1 e\mu_1 \text{ --- } + n_6 e\mu_6) \qquad 44)$$

where

μ_i = mobility of charge carriers

$$S_T = \pm \frac{k}{e} \left[\delta + \ln \frac{2(2\pi m^*_1 kT)^{3/2}}{h^3 n_1}\right] \qquad 45)$$

$$\pm \text{ -------}$$

$$\text{---} \pm \frac{k}{e} \left[\delta + \ln \frac{2(2\pi m^*_6 kT)^{3/2}}{h^3 n_6}\right]$$

where

$m^*_{1_c}$ = the effective mass characteristic of a well system for case of conduction band operation

$m^*_{1_v}$ = the effective mass characteristic of a well system for case of valence band operation

$m^*_{1_c} \neq m^*_{1_v}$

similarly for m^*_2---m^*_6

It is illustrative to consider a specific experimental set of data for Bi_2Te_3 and interpret it in the light of the above formulations. Since it can be shown that the IMWM will apply equally well to Bi_2Te_3 n and p type alloys we will use data for room temperature, from the experimental data plots shown later in this report, in the present calculations.

The measured values for a p-type Bi_2Te_3 alloy at room temperature are:

$$Z_p = 2.85 \times 10^{-3}/^oC$$
$$S = +200\ \mu v/^oC$$
$$\sigma = 1 \times 10^3 \text{ohm}^{-1}\text{cm}^{-1}$$
$$k_T = 1.35 \times 10^{-2} \text{watts/cm}^oC$$
$$\mu = 255 \text{ cm}^2/\text{volt sec}$$
$$R_H = +.255 \text{ cm}^3/\text{coul}$$

From these data and the above formulae we find

$$n_i/\text{well} = 5.4 \times 10^{18}/\text{cc}$$
$$\mu_T = \mu_i = 255 \text{ cm}^3/\text{volt sec}$$
$$\sigma_i/\text{well} = 166 \text{ ohm}^{-1}\text{cm-1}$$
$$m^*_T = .605 m_o$$
$$m^*_1/\text{well} = .18\ m_o$$

The consistency of these calculated band and transport parameters with one another for room temperature in view of the limitations imposed by degeneracy of charge carrier distributions is very good.

The effective mass $m^*_{1\,well}$ agrees very well with the average value of effective mass/ ellipsoid determined by Drabble, et al[33-35] ($0.18m_o$ as compared to their $0.21m_o$).

The slightly modified IMWM shown in Figure 36 will apply to Bi and BiSb alloy crystals. The control of the transport, thermoelectric, and band structure parameters in both the Bi_2Te_3 and Bi cases is centered in the special characteristics of the p orbital half bonds in the presence of anisotropic lattice spacings and resonance bonding.

The combination of p orbital half bonds, and resonance bonding in the PbTe structure suggests that a similar type of model will be applicable to explaining its desirable thermoelectric properties at higher temperatures.

There seems little doubt that this type of model with certain modifications can explain the characteristics of $AgSbTe_2$ alloys. The application of the model will be discussed later relative to the experimental data.

This model for Bi_2Te_3 is consistent with the theoretical predictions regarding factors to maximize to achieve highest Z, namely

$$A \propto \left(m_T^{*\frac{3}{2}} \right) \left(\frac{\mu}{k_{ph}} \right) e^{s+\frac{1}{2}} \qquad 34)$$

The model reveals how high mobility is maintained and simultaneously $m_T^{*\frac{3}{2}}$ is able to be maximized to achieve maximum A. An improvement on the above expression for thermoelectric cooling materials is the following:

$$A \propto N_w \, m_i^{*\frac{3}{2}} \, \frac{\mu}{k_{ph}} \, e^{s+\frac{1}{2}} \qquad 46)$$

where

N_w = number of independent well systems

m_i^* = the average effective mass for one well system

SELECTION OF MATERIAL SYSTEMS IN WHICH TO SEARCH FOR IMPROVED Z MATERIALS FOR THE TEMPERATURE RANGE OF 50°K - 573°K

Characterization of Improved Z Thermoelectric Cooling Materials

1.) They must be materials characterized by molecular-net-structured, p orbital (half bond) bonds, resonance bonds, anisotropy of lattice spacings, high mean atomic weight, medium λ_o (atomic ionicity), zero $\frac{e^*}{c}$ (no effective ionicity), near zero electronegativity difference, and highly polarizable elements.

2.) They should have 6 or more independent "well systems".

3.) They should be able to be advantageously and preferrentially oriented relative to the direction of controlled anisotropic change in lattice spacings and imposition of polarization forces so as to obtain maximized electrical conductivity in the direction of minimum thermal conductivity, simultaneously with maximizing electrical conductivity.

4.) They should have predominantly a D_{3d}^5-R-$_{3m}$ structure with a superstructure lattice of hexagonal form having a c_{hex} of greater than 31 A^o. If a D_{3d}^7-R-$_{3m}$ structure with a superlattice can be found, this would be most interesting.

5.) They could be two phase compositions containing the above structure as a major phase and a compatible lower bond strength structure as a second phase.

6.) They must contain elements characterized by forming crystals with anisotropic lattice spacings (See Table 7).

Selected Systems for Experimental Study

After examining all the known types of chemical bonds and structures and their occurrence (summarized earlier in the report), considering the trends of correlations of a wide range of types of compounds with observed transport properties using many correlation parameters, and later specifically identifying the factors controlling Z in the highest known Z thermoelectric materials (resulting in the development of the IMWM), materials selected for study in attempting improvement of Z were Bi alloys and systems based on modification of $AgSbTe_2$. In addition (not on this project) further studies on improving Z of Bi_2Te_3 alloys were conducted concurrently.

The Bi alloys were selected for the low temperature range and the $AgSbTe_2$ system alloys were selected for the high temperature range.

From the standpoint of compatibility in a D_{3d}^5-R-$_{3m}$, C_{33}, or A_7 type of structure, the planned experimental attack was centered around a selected series of elements and combination of elements for introduction into the $AgSbTe_2$ system.

These elements included Fe, Tl, Au and a few others which we had no time to explore.

These choices were based on the following considerations:

1. Fe has an electronegativity very close to Sb, Ag and Te. It can show a valence of 3. It has a relatively low internal pressure of its unpaired d orbital electrons and its sublimation enthalpy is low. It appears to be able to contribute, alongside of Ag, in ternary tell-

urides to increasing electron mobility. Its lack of p orbitals and use of s orbitals in bonding was considered disadvantageous from the thermal conduction standpoint and therefore it was mostly examined as a partial substituent.

2. Tl was considered to have much to offer as a replacement for Ag in $AgSbTe_2$ because of its higher atomic weight, larger atomic radius, larger polarizibility, similar electronegativity, one p orbital and suppressed s orbitals. Because Tl can display either a 1 or 3 valence, it was also given some consideration as a replacement for Sb.
3. Au was considered to be of interest because of its higher atomic weight. Because its electronegativity is higher than that for Te, it was not expected to bond, but in small quantities, its presence as a well distributed second phase was considered of interest.

In the Bi alloy system, combinations of elements were selected for investigation once the crystal growth of Bi and BiSb alloys was brought under control. Since this stage was only approximately reached at the termination of this project, no discussion of these plans will be presented.

METHODS OF MATERIAL PREPARATION

Introduction

Since anisotropy of structure and transport parameters are expected and desired characteristics of improved high Z thermoelectric materials, the development of methods of preparation of D^5_{3d} - $R\bar{3}m$ and particularly C_{33} -like structures, capable of giving large crystals characterized by controlled anisotropies, is an ultimate materials processing objective.

Highest purity of starting elements and processing containers is a necessity to assure complete elimination of O, N, P, S, Cl, C etc. These anion types can interrupt development of the complex molecular structure of interest. The relatively powerful bonding forces they exert are incompatible with the relatively weak bonding forces in primarily p-orbital bonded - resonance bonded molecular structures.

One expects crystal growing rates will have to be slow and growing times long to achieve good crystals, since molecular orientation and alignment tends to be relatively sluggish when the bonding forces are relatively weak.

The nature of the materials of interest is such that the molecular development, as the material freezes, will tend to eject all atoms with incompatible bonding capabilities, (unless the atoms are in the anion class material above). Hence a concentration of excesses and non-bonding impurities will tend to build up between molecular planes and at the surface of microscopic crystal regions. It is characteristic of these materials that they have strong tendencies to develop mixed types of second phases. In the event the second phase has a structure and properties like that of the major phase; the second phases will be tolerable and may even be desireable if some molecular resonance is possible between the molecules comprising the phases. However, unless the starting elements are extremely pure, the starting chemical formulation favorable, and the preparation extremely clean, development of such a preferred type of second phase is improbable.

Therefore specific processing methods to use in preparing higher Z materials become a basic research problem.

During the course of this project effort, the development of a new improved processing technique was not possible. However, it is to be stressed that basic research on compatible processing methods may prove to be the required answer for achieving improved Z materials.

Bi and Bi-Alloy Crystals

Background Information on Methods of Growing Bi and BiSb Crystals

Growing single crystals of bismuth and its alloys has gradually progressed from an art toward a science. This has been a necessity in view of the stringent requirements placed on these crystals if they are to be used for Peltier-Seebeck or Nernst Ettingshausen cooling.

There have been several methods proposed in the literature for growing these crystals with claims and disclaims for each. In the case of the bismuth-antimony crystal growth processing, there are two schools of thought - one claiming better results using a fast rate of growth, 13 to 76 mm/hr, or higher, and the other a low rate, 0.4 to 2mm/hr.

In comparing the methods, one must consider the size as well as the perfection (e.g. minimum striations) of the grown crystals. The degree of alloying of other elements with the bismuth must also be considered. Bismuth is far easier to grow as a single crystal having a high perfection, than is the case with bismuth-antimony. The larger the desired size of crystal and with a preferred orientation, the more formidable is the task.

In general, all reported techniques for

crystal growing are by horizontal zone or gradient freezing as opposed to the vertical methods, such as Czochralski pulling or Bridgeman casting used for semiconductor crystals.

Jain[38], in the preparation of Bi-Sb alloys for his studies, was able to get large crystals approximately 8 in x 1/2in x 1/2 in by zone leveling an ingot for several passes at a rate of 2 in/hr (5cm/hr) using 450 kc induction heating. Melting was carried out under a helium atmosphere or vacuum. Chemical analyses showed these crystals to have a variation of 3% of the mean value at the center of the ingot.

Smith[39] used samples of bismuth taken from a zone refined ingot. Later he and Wolfe[1] prepared their BiSb alloys essentially as Jain had done except that dry hydrogen was used as the atmosphere. They made six zone leveling passes using a 1/2 inch long zone at 13 cm/hr.

Kooi and his coworkers[40] of Lockheed Missiles and Space Co. in their thermomagnetic cooling investigations also used the zone leveling process for Bi-Sb single crystals. The ingot, sealed under hydrogen, was zone leveled either in a resistance-wound heater or in an induction heater. The zone length was maintained at about one-tenth of the length of the charge. The zone speed was 0.7 to 5 in/hr (1.8 to 12.7 cm/hr)and the temperature gradient was approximately 11°C/cm. Metallographic studies of these BiSb alloys indicated that they were characterized by a cellular structure regardless of the freezing rate and number of passes of the molten zone. They proved the existence of the coring phenomena or variation in composition during growth. This was to be expected since bismuth and antimony are completely soluble in the solid state and their melting points are different. The interior of the cell was richer in antimony and the cell boundary was richer in bismuth.

Fischler[41] used a unique rapid freeze method for growth of bismuth single crystals. Essentially bismuth in a graphite boat lined with smooth quartz plates is heated from one end with a propane torch and melted in air. The torch is then withdrawn so as to allow the bismuth to commence freezing at the opposite end of the boat which has a constriction. Crystallization then proceeds as the flame is gradually withdrawn. The whole crystallization requires only a few minutes. According to Fischler, the method may be used to obtain crystals of any desired orientation using oriented seeds. Doping of the bismuth may also be carried out. Bi crystals used in obtaining 101°C ΔT for T_h = 302°K [41] were grown in this manner.

Brown and Heumann[42] have carried out an extensive study on the growth of bismuth-antimony single crystal alloys. They contend that in the Bi-Sb crystal growing procedure, wherein rather rapid multipass zone-leveling (1.3 cm/hr or greater) is used, very extensive constitutional supercooling takes place in the liquid zone. This problem has been discussed in the literature by several investigators, such as Tiller[43]. As summarized by Brown and Heumann constitutional supercooling must be sufficiently reduced to (1) prevent nucleation of new crystals in the layer of supercooled liquid adjacent to the interface; (2) prevent extensive macrosegregation by fractional crystallization and precipitation within the supercooled layer; and(3) minimize or eliminate microsegregation or cellular substructure.

Using an equivalent expression to that of Tiller for estimating the maximum growth rate without appreciable supercooling, Brown and Heumann calculated a required growth rate of 1mm/hr, even with liquid stirring. After the preparation of the ingot for crystallization, they placed the polycrystalline charge into a horizontal zone-melting apparatus for single crystal growth. The temperature gradient in the molten zone was maintained at 60°C/cm and the growth rates used were between 1.6 and 0.4mm/hr.

Komarov and Regel[43] found that with bismuth the crystallization front goes into oscillatory motion at temperature gradients larger than 40-60°C/cm. At lower temperature gradients the oscillatory motion stops. This motion then could easily disrupt uniform crystallization.

The main problem of the actual crystallization itself resolves into the dissipation of the latent heat of crystallization in the right direction from the interface. In the case of alloys macrosegregation and microsegration must be avoided. Of course, the materials must not be contaminated in the processing.

Preparation of Crystals

The starting materials, Bi and Sb were of 99.9999 wt % purity and were brought to this purity level by zone refining 99.999 wt % Bi and 99.999+ wt % Sb.

Several methods, some of which were suggested in the literature, were investigated for the preparation of both Bi and Bi-alloy single crystals. These have been discussed in progress reports [24, 27]. Only the ones which yielded the best crystals are discussed here.

Bismuth

Two methods were used successfully for the preparation of bismuth single crystals. These were as follows:

An outgassed high-purity graphite boat (1" x 1-1/4" x 22" cavity) was charged with the 99.9999 wt % bismuth. The stainless steel

liner used in the modified Fischler technique for bismuth crystal preparation [27] was placed in a graphite boat at approximately the 6 inch position of a 22 inch length of boat. The liner, with its necked-down design, served as a seeding site. The charged boat was inserted into a Vycor tube and pumped down to a forepump vacuum ($\sim 10^{-3}$torr). The tube was then backfilled with hydrogen and pumped down again. This operation was repeated several times. On the final operation, the tube was backfilled with hydrogen to a 1 - 3 psi pressure. The charge was zone leveled in order to obtain a uniform cross-section ingot. This was followed by several passes in one direction (zone refining) at a speed of 1 in/hr. Any additional impurities which could be removed by this zone refining would segregate to the ends of the ingot and it was for this reason that the liner was placed at the 6 inch position rather than at the front end of the graphite boat. A crystal of the order of 3"x1"x1" was obtained. No preferential seeding could be done using this method.

The second method used successfully for the preparation of bismuth single crystals consisted of charging the 99.9999 wt % bismuth into a Vycor boat. The boat was of a trapezoidal shape with a 3/4"x1-1/8" cross section and 6" and 7" bottom and top respectively. The Vycor surfaces were smooth to minimize nucleation sites during the crystallization.

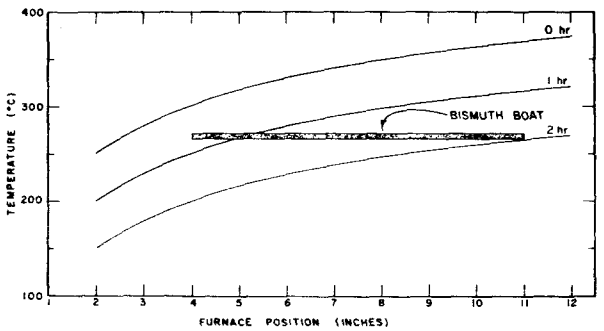

Fig. 38. Temperature profile in horizontal boat during Bismuth crystal growth.

The boat containing the bismuth was placed into a Vycor tube, pumped down and backfilled with argon instead of hydrogen as in the previous method described above. The tube was then placed into a Marshall furnace having a temperature profile as shown in Fig. 38. The temperature was raised so that the charge became molten. Through a saturable reactor type programmer the system was allowed to equilibrate for 4-6 hours and then the temperature was lowered to approximately 200°C over a period of hours. The power to the furnace was cut and the ingot allowed to cool. Actually the rate of temperature drop was very nearly that of the furnace cooling rate. This directional freeze technique yielded bismuth single crystals of good size and quality. No attempt was made to seed the crystal for desired orientation.

Bismuth-Antimony Alloy

The best single crystals of bismuth-antimony alloys were prepared using the directional freeze technique. The problem of obtaining single crystal specimens of the alloys presents more difficulties than does the bismuth.

The pure elements, Bi and Sb, were sealed in an evacuated Vycor tube in the stoichiometric proportions and placed in a rocking type furnace for a period of 24 hours to allow homogenization. The charge was then air quenched. The ingot was then processed as was the bismuth. The crystals obtained were not as large as those of bismuth.

$AgSbTe_2$ and Bi_2Te_3 Alloy Systems

The processing techniques which have been successfully applied in producing known high Z_P extrinsic semiconducting materials are those common to standard Bi_2Te_3 and experimental $AgSbTe_2$ alloys.

Many investigators [8, 9, 12, 43, 45, 46] have contributed to the processing technology for high Z_P materials which is represented in the standard OSD p and n type Bi_2Te_3 alloys. From this fund of historical information and current processing knowhow, methods to use in these studies were developed.

The general types of processing techniques considered for these studies included horizontal and vertical casting in closed systems which provide for vapor pressure control, since most of the materials of interest have volatile components. Thus one usually melts, reacts and homogenizes stoichiometric amounts (if predictable) of high purity elements in evacuated quartz or Vycor tubes followed by s ome form of casting.

There are many methods of casting or crystallization. Using the horizontal technique, the traversal of a molten zone, developed by R.F. or resistance heating, may be used to obtain crystallinity and compositional variations. Gradient freezing can be used. In this case the sealed charge is placed in a furnace with a chosen temperature profile and the material allowed to solidify and crystallize by programming the time-temperature variables.

Using the vertical casting technique, the sealed molten charge is vertically dropped through a hot zone, either resistance or R.F. heated. The material crystallizes as it moves out of the hot zone through the temperature grad-

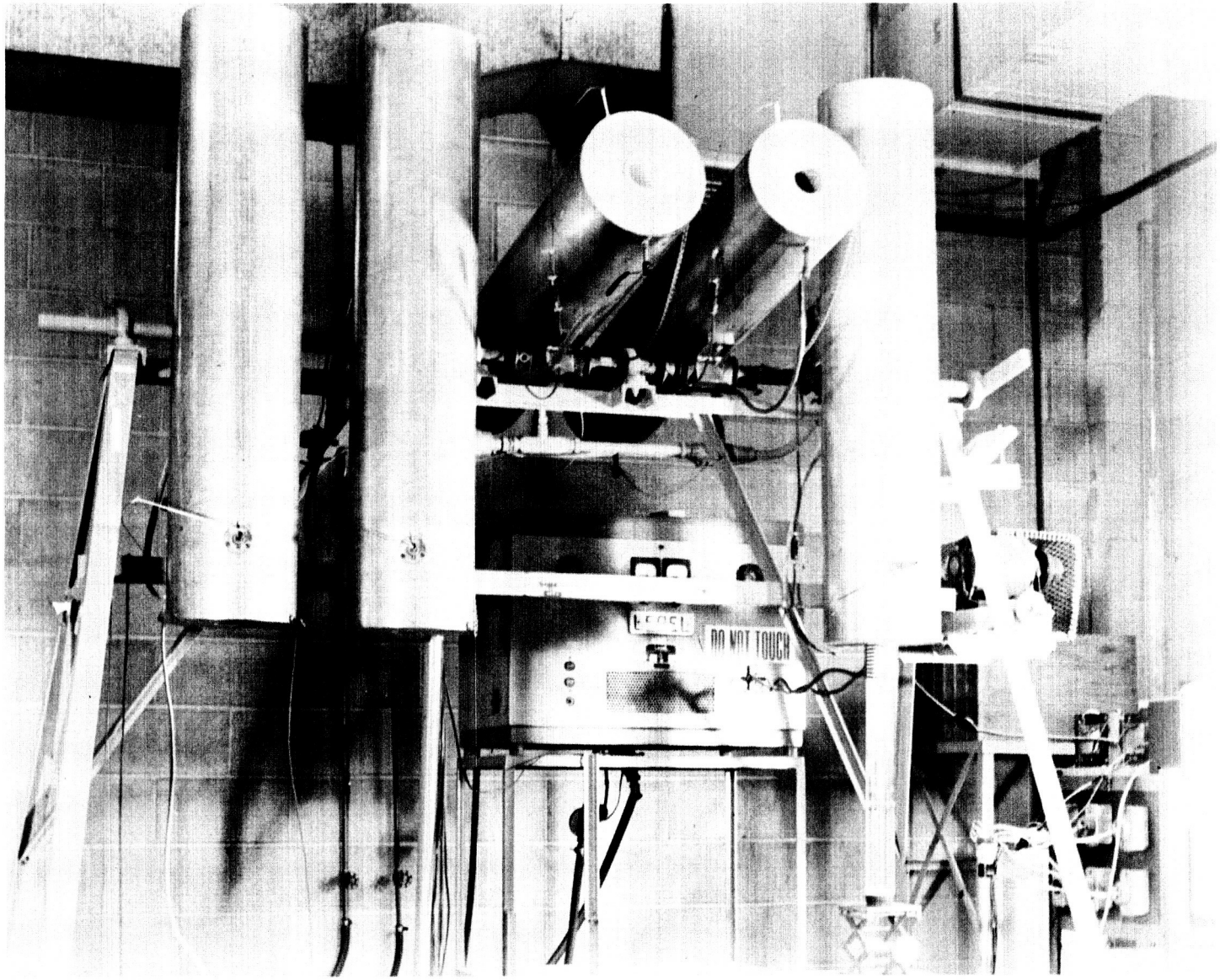

Fig. 39. Rocking autoclave and Bridgeman casting equipment.

ient. R.F. induction heating produces a sharper temperature gradient between the liquid and solid than resistance heating. Also it agitates the melt as it freezes. In contrast, resistance heating allows growth of larger crystallities because of no agitation.

Advantages of this technique are that the dropping speed, diameter of ingot, and furnace temperatures are all controllable for optimizing the characteristics of thecast alloy. Disadvantages are breakage of tubulation if the material expands on cooling and problems in establishing a smooth temperature gradient in a vertical furnace to obtain the desired vapor pressure control.

Figure 39 shows the rocking autoclave and Bridgeman casting unit which was used in preparing the final vertically cast versions of selected alloys.

Choice of Methods

The methods used to process the materials made during this effort were selected to fit the particular requirements of the study.

All the compositions investigated were ternary, quaternary or more complex compounds and alloys. Most of them could not be chemically formulated with certainty that the reaction would proceed according to assumed valences. In general, melting points, dissociation tendencies and other chemical and physical properties were not known. For these reasons and in view of the objective of obtaining material with electrical properties within a specific range, a large number of alloys within one ternary or quaternary system had to be prepared in a rapid exploratory way before a specific alloy could be selected for the slower more sophisticated processing via the best method known today for obtaining high Z material, namely vertical casting.

Therefore a suitable combination of exploratory procedures had to be evolved. These consisted of the quench-anneal process, metallographic analysis and electrical analysis.

The Quench-Anneal Method of Processing

High purity elements are weighed and encapsulated in quartz or Vycor ampoules in a vacuum of 10^{-6} torr. The sealed charge is then melted and reacted. Thereaction time and temperature are varied to suit the nature of the elements being combined.

Usually the molten charges were maintained in the furnace for 24 hours to react and homogenize. After visually ascertaining the apparent melting temperature, the charge was held during this period at about 50°C above the melting point.

The sealed charges are then removed from the furnace and quenched in air. The charges usually solidified in a matter of seconds. If they did not appear completely reacted or homogeneous they were inserted back in the furnace for another 24 hour period.

In this air quenched state, the material is not suitable crystallized. Therefore each charge was subsequently annealed at 50°C below its melting point for 24 hours. If the material was brittle and broken on air quenching, it was usually remelted and then solidified and cooled to 50°C below its melting point and annealed for 24 hours before cooling to room temperature.

Metallographic Analysis

The materials produced by the quench-anneal process are generally expected to be homogeneous in a microcrystalline way even though the formulation inherently is characterized by incongruent melting or freezing. Annealing was expected to cause some crystal growth and relief of stresses.

To preliminarily determine the nature of the resulting alloys, metallographic analyses were used to establish whether they were single or multiphased and the nature of the phase geometry. Alloys showing a single phase nature or very little second phase were selected in this manner.

Exploratory Electrical Analysis

Since the material systems investigated were selected for the compatibility of their elemental ingredients, the possibility that multiphased material with good thermoelectric properties could be obtained was recognized.

Further all promising materials via metallographic and visual analysis, required preliminary thermoelectric and transport property evaluations to ascertain whether the casting method should be now applied to obtain material for detailed analysis as a function of temperature.

Therefore each alloy ingot was subjected to exploratory checking of S, R_H and σ at liquid air and room temperature. Calculations were made of apparent mobility, μ_a and charge carrier concentration, n/cc, from these data.

Vertically Cast Alloys

After establishing the nature of the chemical, metallurgical, structural, and electrical properties of a new alloy system in the above exploratory fashion, a selected alloy was prepared again via the more sophisticated and slower casting method.

The detailed analyses made on the cast alloys selected in this manner are discussed in a later section.

METHODS OF MATERIAL EVALUATION

Hall and Thermoelectric Measurements Apparatus

During the period of this contract, measurement facilities were established, using Ohio Semiconductor Division funds, for determination of (1) Z, S, k and ρ thermoelectric parameters by a modified Z meter technique and (2) R_H, σ, μ_H, and magnetoresistance parameters on experimental materials over a temperature range from 77 to 560°K with reasonable speed and accuracy. This apparatus and its characteristics are described here.

A component and wiring schematic of the measurement installation is shown in Figure 40. The same instrumentation is used for both Hall and thermoelectric measurements. Data are obtained on the samples in vacuum and electrical connections are provided, through two octal feed thru connectors (mounted in individual sample holders), by matching appropriate numbered arrows as indicated in Figure 40.

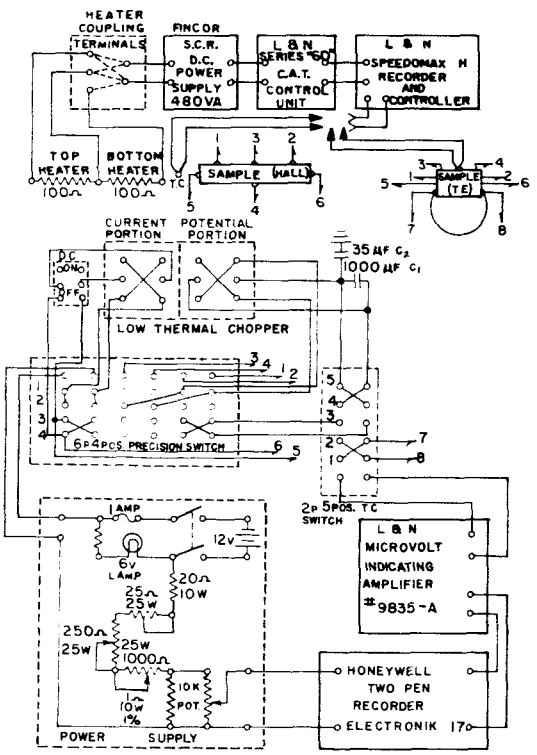

Fig. 40. Component and wiring diagram of Hall and thermoelectric measurements apparatus.

The dc power supply consists of a 12 volt lead-acid storage battery connected in series with three rheostats for current adjustment, a calibrated one ohm standard resistor and a current limiting resistor. The current range is continuously adjustable from approximately 9 to 570 ma. A ten turn 10k-ohm potentiometer is in parallel with the one ohm resistor to serve as a voltage divider for current monitoring by one channel of a Brown Electronic 17, two pen recorder.

This power supply provides ac current to the Hall or thermoelectric sample through the first set of contacts of a Scientific Research Instruments mechanical chopper, having two double pole double throw switches operated by a common shaft, when the 6 pole 4 position precision switch is in positions 1 or 2. In positions 3 and 4 it provides dc current, in both directions, for measurement on the thermoelectric sample. The contacts of the current portion of the chopper were adjusted to make-before-break to prevent oscillation in the recorder pen.

Other functions of the 6 pole 4 position switch are to select ac resistivity potentials on either sample in position 1 and Hall potential or thermoelectric resistivity potential in position 2. These potentials are indicated by the second pen of the recorder through the potential measuring portion of the chopper, the 2 pole 5 position T C switch, and the dc amplifier. The contacts of this second portion are adjusted to break-before-make while the break time occurs during and is slightly longer than the shorting time at the current portion contacts. [47] This arrangement, along with capacitors C_1 and C_2 eliminates excessive oscillations in the potential indicating pen of the recorder. Polarity reversing of the dc signal is necessary in measuring Hall samples since the Hall voltage developed for a given current flow direction, depends on the sign of the majority carrier of the sample, relative position of the Hall probes, and direction of the magnetic field. This is provided for in positions 4 and 5 of the 2 pole 5 position switch. DC resistivity potentials are measured on the thermoelectric sample when the 6 pole 4 position switch is in position 3 or 4 and the 2 pole 5 position switch in position 3. The 2 pole and 2 position dc switch was found necessary in this circuit to eliminate chatter in the recorder pen caused by the chopper when dc measurements were being made.

The differential copper-constantan-copper thermocouple is connected across the thermoelectric sample using epoxy to prevent electrical shorting. This arrangement proved to be satisfactory for ΔT measurements. All electrical leads on the Hall sample and the two current leads on the thermoelectric sample were 30 gauge copper; the remaining leads and thermocouples on the thermoelectric sample were 36 gauge copper and constantan.

The temperature regulation circuit consist of a Leeds and Northrup Speedomax H recorder and controller with an AZAR unit, a current adjusting type, control unit with proportional band, differential and integral functions, and a Fidelity S.C.R. dc power supply. The AZAR unit provides for zero and full scale range adjustment of the recorder. There is an adjustable thermocouple compensation circuit within the speedomax H which allows continuous temperature control from liquid nitrogen to 300°C. The control unit senses differences between the set temperature and the measured temperature, indicated by the pen, and gives an output dc signal, proportional to the desired increase or decrease in power input to the heaters on the sample holder. This signal controls the output level of the dc power supply to the heaters. These may be connected to the power supply in series, parallel, or individually, depending on the different power requirements at various portions of the temperature range.

The amplifier and recorder were calibrated against a K-3 potentiometer. The accuracy of the circuit including the amplifier and recorder was measured experimentally by placing a low resistance standard at the sample position. In this way the systematic errors in the measurement were reduced. Random error associated with instrument drift was not noted. However, the manufacturers' specifications on the recorder and amplifier were used in the error analysis of data. The major contribution of error in this circuit depends upon the magnitude of the value being measured. The error generally falls between 0.72 and 3.4 percent. Larger error results when low value readings are taken on the most sensitive scale of the amplifier (0-50μV) and is independent of the absolute potential being recorded. This is slightly higher than 0.5μV +0.15 percent of reading, as specified error on the low range of a K-3 potentiometer. Error from thermoelectric sample preparation has been considered elsewhere [48, 24] and shown to be approximately 1%. The major contribution comes from the diameter and length of the lead wires.

The sample arrangement for Hall measurements is shown in Figure 41. The use of lavite as the insulating mounting block in the sample holder has proven satisfactory for the operation over the wide temperature range. All leads to the measuring and temperature control circuits are soldered to the inside pins of two octal feed throughs located in the header. All other connections are a permanent part of the apparatus wiring. This arrangement is placed in a Hofman liquid helium magnet dewar positioned with its narrow tail section between the pole faces of a Varian magnet: these have not been shown in Figure 41. The sliding thermal contacts were found necessary for fast initial cooling of the sample chamber and to serve as a heat path which becomes necessary for temperature regulation.

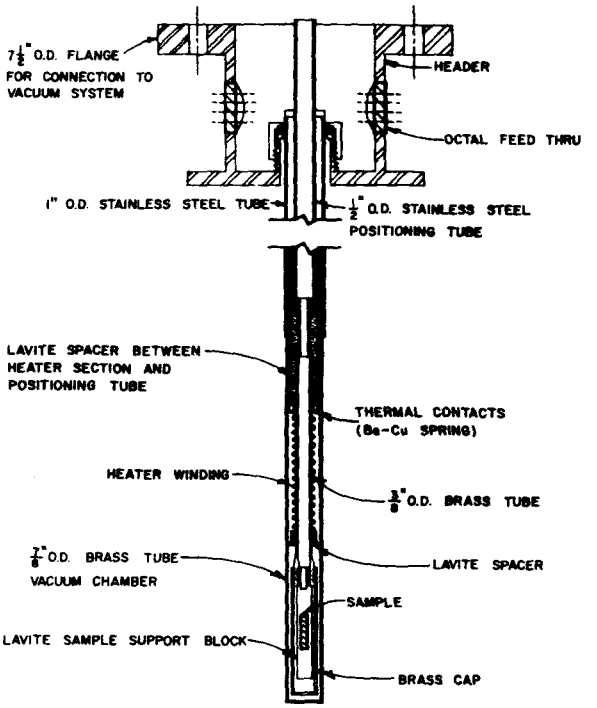

Fig. 41. Design of sample holder for Hall and related effects.

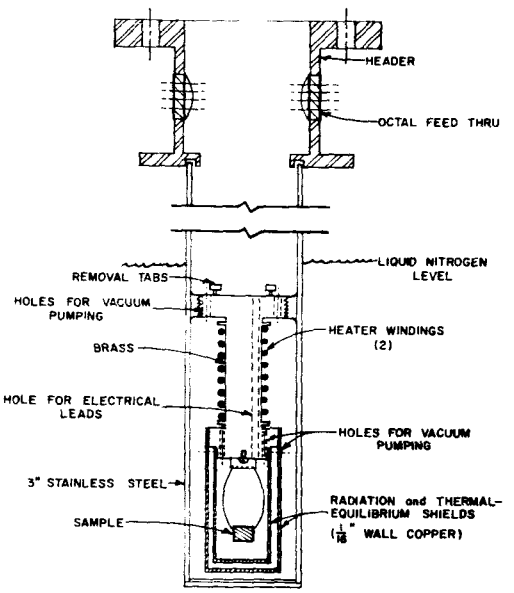

Fig. 42. Design of sample holder for thermoelectric measurements.

The sample arrangement for thermoelectric measurements is shown in Figure 42. The sample is suspended by its lead wires (only two of these are shown) in a chamber of constant temperature provided by two concentric copper envelopes screwed to the base of a massive heater. The outer jacket serves as a heat conductor and radiation shield and the inner jacket,

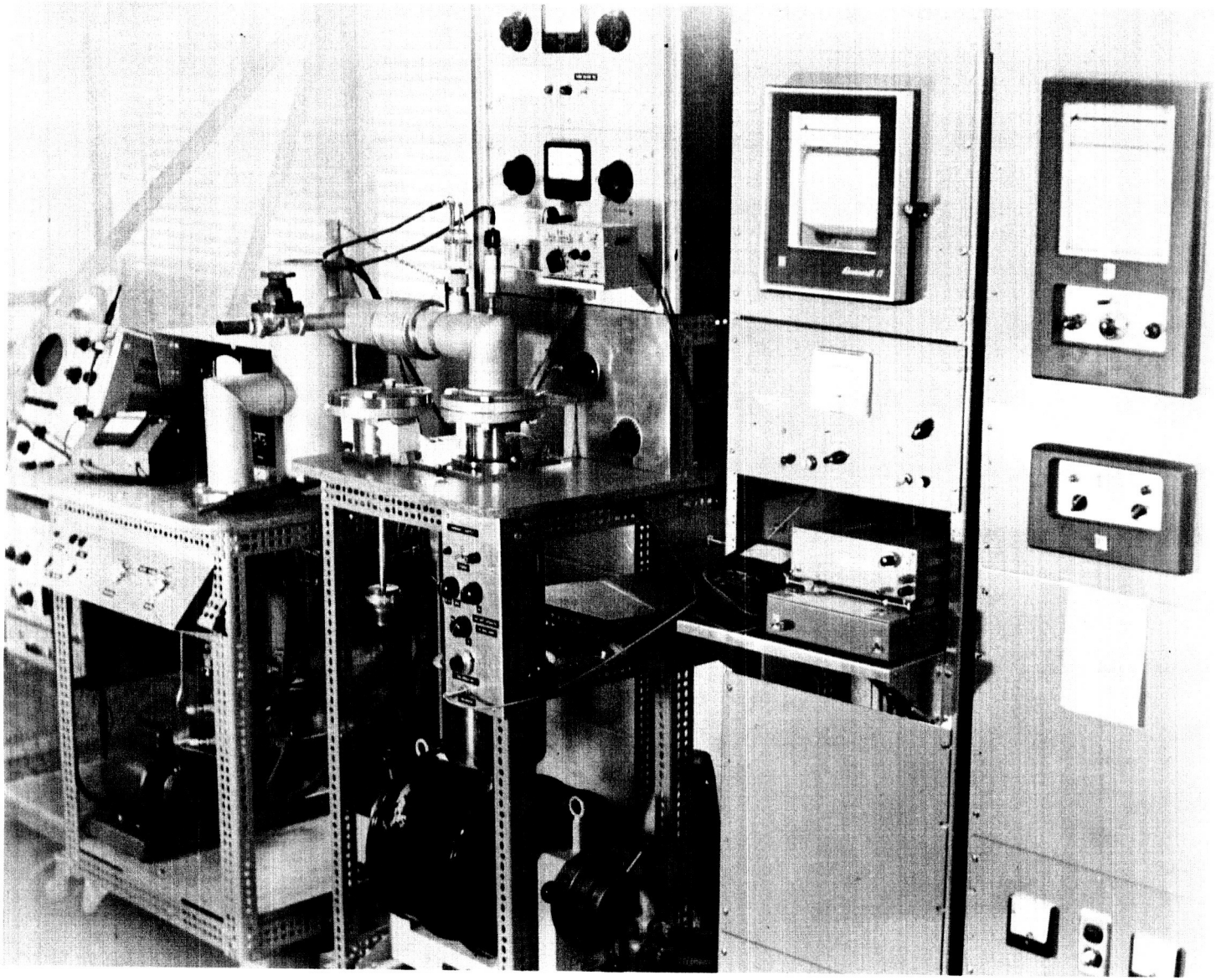

Fig. 43. Photograph of wide temperature range test equipment.

because of its high thermal conductivity allows thermal equilibrium to be reached between its walls and the heater base. The two windings on the heater section are non-inductively wound and may be connected in series, parallel, or individually. The heater and shield assembly is screwed into a brass ring welded to the stainless steel outer jacket. This metallic connection to the surrounding liquid nitrogen provides initial rapid temperature lowering of the sample and chamber and a heat flow path for temperature regulation above 77°K.

A picture of the evaluation apparatus is shown in Figure 43. The vacuum system, capable of obtaining 10^{-6} torr, is shown connected to the mobility measurement apparatus. The flange to the left of this connection is where thermoelectric measurements are made; part of the sample jig extends below the table top. The magnet and power supply is a remounted Varian system with 4" pole faces. With the helium dewar in place, the maximum magnetic field is 8.1Kg and is adjustable down to approximately 130 gauss. The residual field in this magnet is 25 gauss.

Technique and Method of Data Presentation

Hall and Related Effects

In making Hall measurements it was, in general, found necessary to adjust the current through the sample in order to obtain maximum recorder sensitivity and to keep the values of developed potentials within the instrumentation range at various temperatures and magnetic field intensities. Further in order to directly compare and plot individual sample Hall field data as a function of magnetic field intensity, it was necessary to normalize the Hall field to some constant current density. (This was selected to be 1 amp/cm^2 and was approximately the mean current density used in the measurements). The Hall voltage and resistance probe potentials were checked for linearity as a function of current through the sample at 77°K and 300°K at some constant field value. Linearity was found for all measurements reported here.

Frequency effects have been observed in ac Hall measurements [49] where mixed conduction was involved. For this reason the Hall voltage was checked for variations as a function of chopper frequency on samples in which mixed conduction was known or suspected. No variation was noted for the measurements presented in this report.

Where weak magnetic field Hall mobility as a function of temperature is of interest, it is necessary that the low field approximation to the Hall coefficient be met over the temperature range of measurement. The prescription relating the Hall coefficient R_H to the measured parameters is given by

$$R_H = \lim \left(\frac{E_H}{BJ} \right) \quad B \longrightarrow 0 \qquad 47)$$

Where E_H is the measured Hall field for a given magnetic field intensity B and current density J. E_H vs B data for J = 1 amp/cm^2 were plotted for all samples to determine the maximum magnetic field to be used (and held constant) over the temperature range of investigation. The maximum is found where the curve deviates from a straight line extrapolation through B = O. In all cases the saturation curves for liquid nitrogen temperature were obtained to define $B_{(max)}$. However, room temperature data were also taken.

The Hall coefficient R_H^T at a particular temperature T was then obtained as follows:

$$R_H^T = \left(\frac{E_H^T}{BJ \times 10^{-8}} \right) \quad B \leq B_{(max)} \quad \text{cm}^3/\text{coul} \qquad 48)$$

B (in Gauss) was chosen at some value below or equal to $B_{(max)}$ depending on the measured values of E_H or instrument sensitivity.

The Hall mobility μ_H as presented in this report unless otherwise noted has been defined as

$$\mu_H^T = R_H^T \, \sigma_o^T \quad \text{cm}^2/\text{volt sec} \qquad 49)$$

where σ_o^T is the measured conductivity with B = O.

The magnetoresistance data are obtained on experimental samples at the same time Hall measurements are made. The defining equation relating the magnetoresistance $\Delta \rho / \rho$, to measured quantities is

$$\Delta \rho / \rho \Big|_T = \frac{V_{ac}(B) - V_{ac}(o)}{V_{ac}(o)} \Big|_T \qquad 50)$$

This shows the magnetoresistance as the change in the resistivity upon applying a field divided by the resistivity for the zero field case and it is determined by the measured ac potentials at constant current.

The magnetoresistance coefficient M is defined by

$$M^T = \lim \left(\frac{\Delta \rho}{\rho B^2} \right) \quad B \longrightarrow o \quad \text{Gauss}^{-2} \qquad 51)$$

and the above equation is used in its evaluation.

Thermoelectric Measurements

The Seebeck coefficient was determined from

$$S^T = \frac{\frac{1}{2}\left(\left|V_{dc}(I+)\right| + \left|V_{dc}(I-)\right|\right) - V_{ac}}{\Delta T}\Bigg|_T \quad \frac{\text{Volts}}{^oK} \qquad 52)$$

where V_{dc} (I+), V_{dc} (I-) and V_{ac} are the measured potentials for the two directions of current and the chopped dc, respectively. The numerator of this expression is just the Seebeck potential V_s. The temperature difference ΔT is also a directly measured quantity.

The figure of merit at temperature T is determined through the familiar Z - meter expression,

$$Z^T = \frac{V_s}{V_{ac}\,T}\Bigg|_T \quad ^oK^{-1} \qquad 53)$$

and needs no further discussion.

The resistivity was determined from sample dimensions, value of chopped current, and measured V_{ac}. After several attempts to measure the contribution of contact resistance to the sample resistance it was found that the instrumentation and dimension measurement error would not allow resolution of this quantity. For this reason the two additional potential probes on the side of the sample were eliminated since they would then serve only to decrease the the accuracy of the other measurements because of loading.

The thermal conductivity was calculated from the values determined above and the prescription given earlier.

PREPARATION AND EVALUATION OF STATE-OF-THE-ART MATERIALS AND DEVELOPMENT OF TECHNIQUES

The previous sections summarize the nature of methods and equipment used in material preparation and evaluation.

In application of any selected and preferred material preparation method, sophisticated consideration of detail is required for achievement of optimized high Z specimens. These requirements arise because the relatively weakly bonded complex molecular structures common to the highest Z thermoelectric cooling materials, balancing of vapor pressures of the constituents above the melt, temperature gradients at the liquid-solidus interface, rates of solidification, segregation forces, incomplete elimination of elements such as O, N, P, S, Cl, C and Na from the closed reaction vessel etc.

Therefore, reproduction of state-of-the-art materials matching the best properties noted in the literature is in itself a time consuming effort. Considering the objectives of this project, we did not attempt to completely optimize either Bi and $Bi_{88}Sb_{12}$, or $AgSbTe_2$ and $AgSbTe_2$-PbTe alloys at this stage in the program.

In the case of Bismuth telluride n or p type alloys, the standard OSD alloys are represented here as state-of-the-art.

Bi and BiSb

Bi crystals up to 3 inches in length with 1"x1.25" cross-sections were grown from 99.9999+% pure starting material by a horizontal directional freeze technique using resistance heating as described in a previous section.

$Bi_{88}Sb_{12}$ crystals proved more difficult to grow. The chief problem is fractionation of the Bi and Sb. Crystals of smaller size were obtained after considerable effort.

Bi and BiSb alloy crystals were cut from the ingots and optically oriented by the light figure technique [50]. The longitudinal axis of the crystal bar was oriented parallel to the trigonal axis. Bi crystal sample sizes were 2.5x2.5x20 mm and $Bi_{88}Sb_{12}$ samples were about 2x2x5 mm. Electrical leads were soldered directly to the sample with a $Bi_{75}Sn_{23}Sn_2$ solder (lead wires were No. 30 gauge copper) using stannous fluoroborate flux.

In the data presented, the identification of the crystal axes is as follows:

1. refers to the binary axis
2. the bisectrix
3. the trigonal

The thermoelectric and Hall effect jigs and equipment described in the previous section were used to obtain evaluations of the Z, S, k_T, σ, R_H, vs temperature from 78°K to 400°K. Since measured Hall mobility in Bi and Bi alloy crystals is not only a function of crystallographic orientation but also magnetic field, Hall field vs. magnetic field determinations at 300°K and 77°K were made to determine a magnetic field within the weak magnetic field region for which $R_H = \lim\left(\frac{E_H}{BJ}\right)_{B \to O}$ is constant for a given current density and temperature over a range of B.

Bismuth

From E_H vs B plots (e.g., see Figure 44) a field B was selected for use in determining R_H vs temperature. The B field used in R_H determination on Bi was 335 gauss when $E_H \parallel 1$.

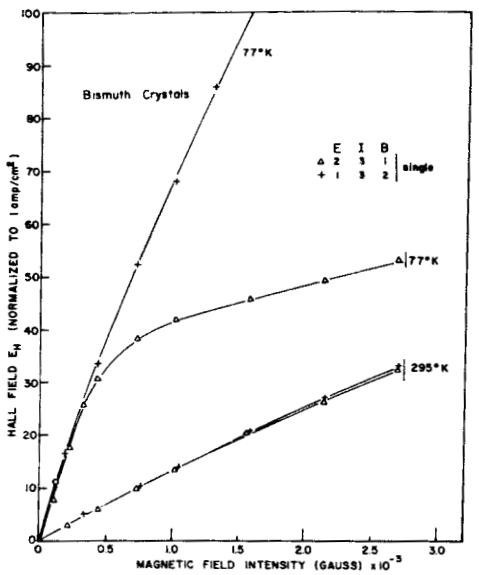

Fig. 44. Typical Hall field vs magnetic field plot for Bi crystals as a function of orientation and temperature.

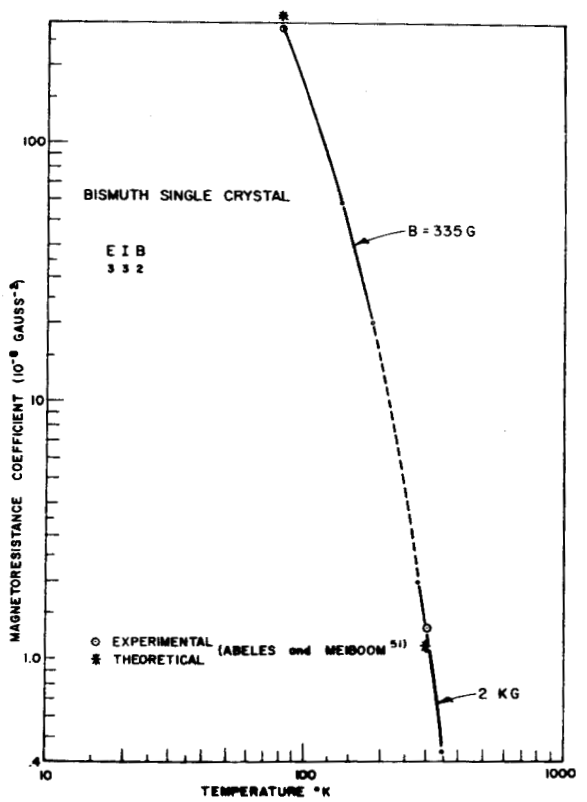

Fig. 45. Magnetoresistance coefficient vs temperature for OSD Bi crystals.

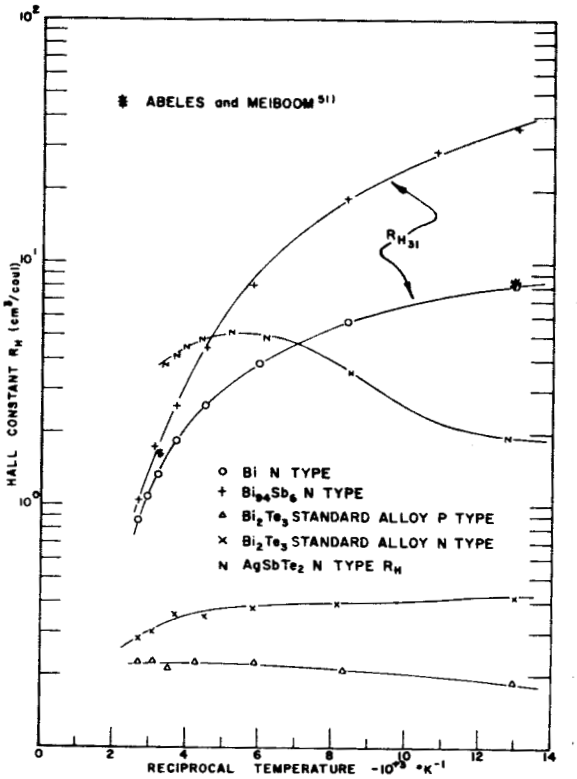

Fig. 46. R_H vs $\frac{1}{T}$ for Bi and $Bi_{94}Sb_6$ crystals ($R_{H_{31}}$), OSD standard n and p type Bi_2Te_3 alloys, and $AgSbTe_2$ with $-R_H$ and $+S$.

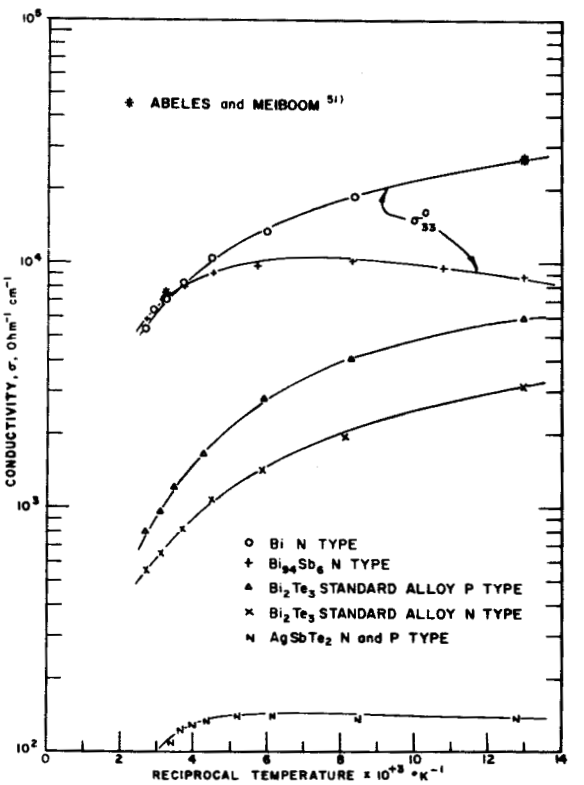

Fig. 47. σ vs $\frac{1}{T}$ for Bi and $Bi_{94}Sb_6$ crystals (σ°_{33}), OSD standard n and p type Bi_2Te_3 alloys, and $AgSbTe_2$ with $-R_H$ and $+S$.

Since the thermomagnetic Z_{NE} is directly proportional to the magnetoresistance, $(\rho_H - \rho_o)/\rho_o$, the magnetoresistance coefficient $(\rho_H - \rho_o)/\rho_o B^2$, was also determined to characterize the Bi crystals for thermomagnetic cooling. In Figure 45, the magnetoresistance coefficient measured on our Bi crystals is shown compared to Abeles' and Meiboom's data [51].

In Figure 46, R_H vs. $\frac{I}{T}$, and in Figure 47, σ_{33} vs. $\frac{I}{T}$ for our Bi crystals for one crystallographic orientation, $E_H \parallel 1$, are shown. Excellent correlation with Abeles' and Meiboom's data [51] is apparent.

In Figure 48 the Hall mobility $(R^o_H \sigma^o)_{31}$ vs. T is shown. Again agreement with Abeles and Meiboom [51] is obtained. The temperature dependence of μ is approximately T^{-3}.

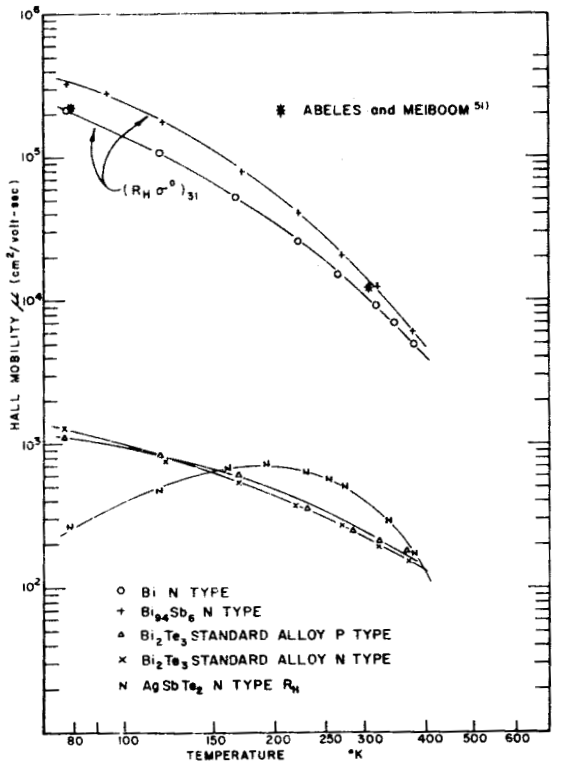

Fig. 48. μ vs $\frac{1}{T}$ for Bi and $Bi_{94}Sb_6$ crystals $(R_H \sigma^o)_{31}$, OSD standard n and p type Bi_2Te_3 alloys, and $AgSbTe_2$ with $-R_H$ and +S.

An adjacent Bi single crystal specimen was used to obtain Z_p, $S_e - S_p$, k_T and σ^o_{33} vs. temperature at zero magnetic field. The current flow was parallel to the trigonal axis. Figure 49 shows these data vs. temperature over the temperature range from 100-390°K. In Figure 50, $Z_p T$ vs temperature is plotted and compared to data obtained by Gallo et al [52] for the same crystal orientation. Good agreement is apparent.

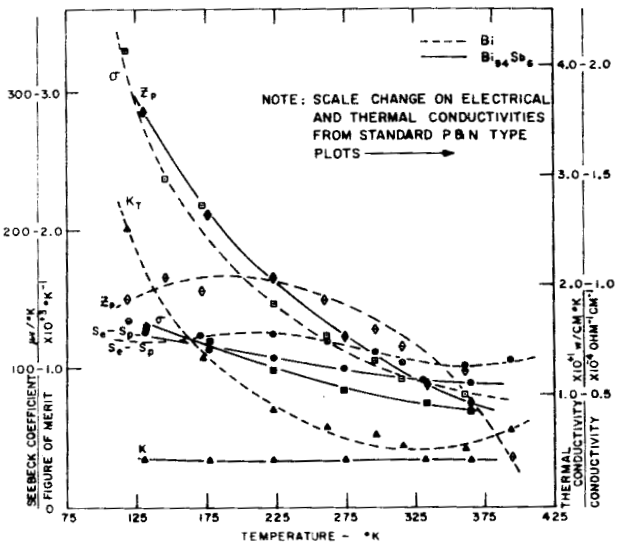

Fig. 49. Z_p, $S_e - S_p$, k_T and σ^o_{33} vs temperature for OSD Bi and $Bi_{94}Sb_6$ crystals.

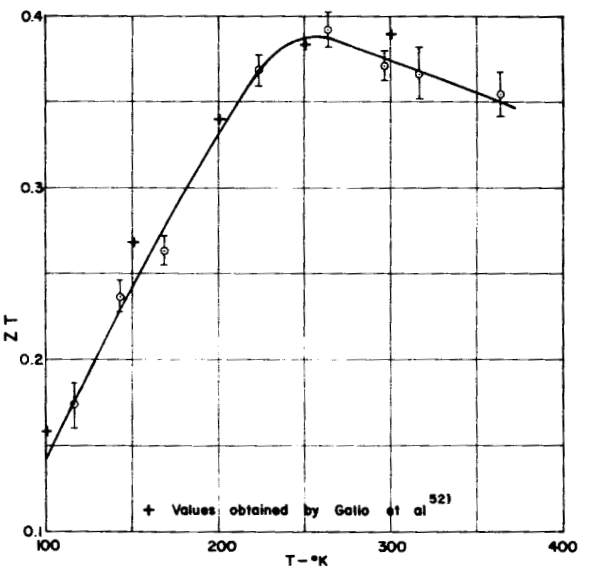

Fig. 50. $Z_p T$ vs temperature for OSD Bi single crystal.

Thermomagnetic Shaped Cooler

Experimental evaluation of a shaped [5], (11 to 1 shape ratio) single crystal of pure bismuth 2 cm long and 0.5 cm^2 in cross section cut from a crystal 2x1.1x1.3 cm was started during the last month of this contract. It had been intended that a detailed evaluation of thermomagnet-

ic cooling at low temperature would be carried out with this speciman. Unfortunately, time did not permit construction of an adequate sample chamber. The temperature at the center of the cooler base increased rapidly when maximized [40] d.c. current density was turned on at high magnetic fields. Because of the way in which the sample was mounted onthe heat sink, the base temperature did not remain uniform. This gave a large error in the measured ΔT established across the device.

In conclusion it is apparent that a technique and a method of Bi crystal growth capable of yielding large crystals of good quality material for thermomagnetic cooling studies and a starting point for Bi alloy development for improved thermoelectric semimetals to use in the low temperature range was achieved.

BiSb Alloy

The BiSb alloy crystals examined for state-of-the-art evaluation purposes were intended to be $Bi_{88}Sb_{12}$. However, owing to fractionation, they were approximately $Bi_{(90-93)}Sb_{(10-7)}$ as indicated by the comparisons with literature data[10, 40] of the resistivity ratio $\rho_{33}(H)/\rho_{33}(o)$ vs. B (Figure 51), relative resistivity $\rho_T/\rho_{300^\circ K}$ vs. $T^\circ K$ (Figure 52), and ρ and $\rho_{33}(H)/\rho_{33}(o)$ vs. antimony concentration (Figure 53).

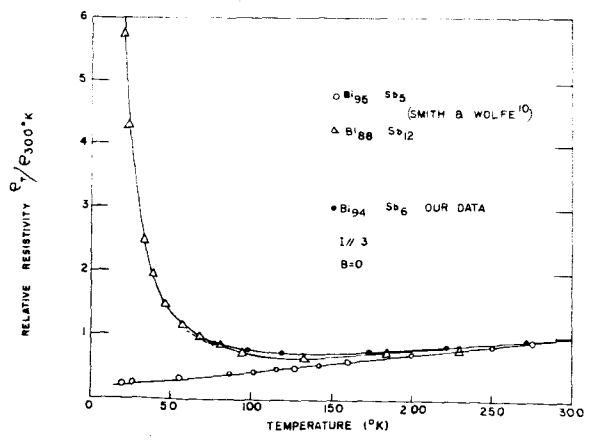

Fig. 51. Comparison of relative resistivity versus temperature for OSD $Bi_{94}Sb_6$ crystals and Wolfe and Smith's[10] $Bi_{95}Sb_5$ and $Bi_{88}Sb_{12}$ crystals.

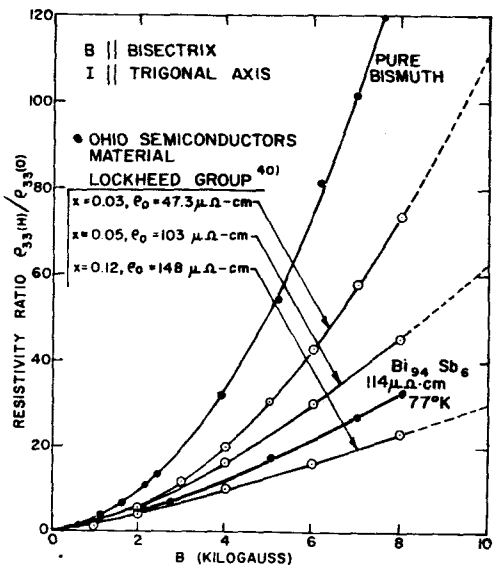

Fig. 52. Resistivity ratio $\rho_{33}(H)/\rho_{33}(0)$, versus magnetic field at 80°K for OSD $Bi_{(94)}Sb_{(6)}$ and Bi compared to Lockheed Group's[40] $Bi_{97}Sb_3$, $Bi_{95}Sb_5$, and $Bi_{88}Sb_{12}$ Crystals.

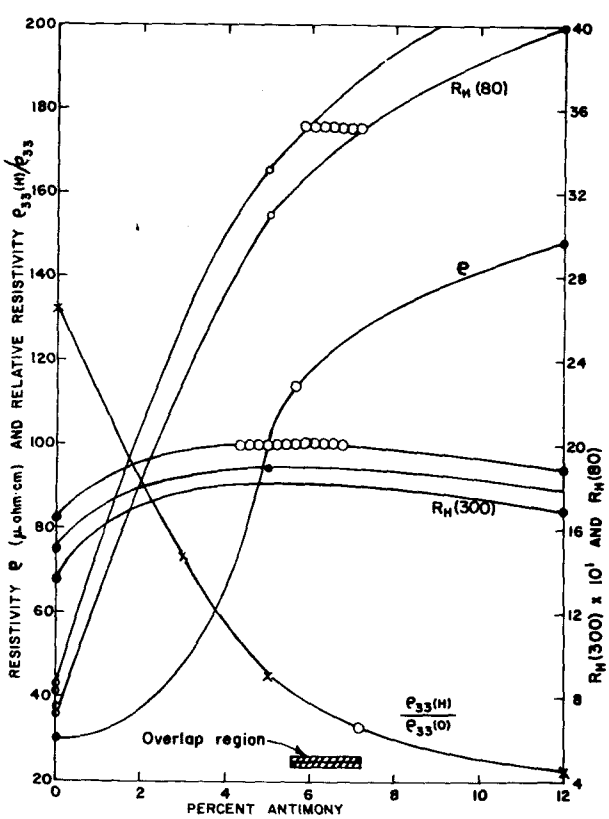

Fig. 53. Comparison of literature data and OSD alloy data on resistivity, ρ, relative resistivity, $\rho_{33}(H)/\rho_{33}(o)$ and Hall coefficient (80°K and 300° K) versus antimony content for $Bi_{1-x}Sb_x$ alloy crystals.

For one crystal E_H vs. B plots revealed 335 gauss was a satisfactory magnetic field to use and still assume weak field approximation equations.

Figure 46 shows $R_{H_{31}}$ vs $\frac{I}{T}$, Figure 47 shows $\sigma_{33}{}^{o}$ vs. $\frac{I}{T}$, and Figure 48: $(R_H{}^{o}\sigma)_{31}$ vs. $T^{o}K$ for the crystal.

An adjacent crystal was used to determine $Z_p, S_e\text{-}S_p, k_T$ and $\sigma^{o}{}_{33}$ without magnetic field in order to evaluate the thermoelectric cooling characteristics of this alloy in the low temperature range (See Figure 49). Table 12 shows our values compared with those of Smith and Wolfe[10]. It is noted a $Z_p = 3\text{x}10^{-3}$ is reached at 125°K for the OSD alloy.

TABLE 12

Comparison of Magnetoresistance, Thermoelectric Power and Figure-of-Merit for O. S. D. $Bi_{.94}Sb_{.6}$ with Published Values

Parameter	Smith and Wolfe[10]		O. S. D.	
$\rho(T)/\rho(300^{o}K)$	150°K		150°K	
	0.7		0.65	
S	300°K	125°K	300°K	125°K
($\mu v/^{o}K$)	-110	-140	-95	-130
Z	300°K	125°K	300°K	125°K
($^{o}K^{-1}\text{x}10^{-3}$)	1.8	4.0	1.08	3.1

In view of these evaluations and comparisons, it was concluded that methods and techniques for growing Bi alloys had been developed to a point that alloy modification studies could be started as specified by the application of the IMWM model for Bi (see Figure 36).

Bi_2Te_3 Alloys

The OSD laboratory production bismuth telluride n and p type alloys were evaluated in the same manner as the other alloys.

The Z_p, S, k_T, and σ vs. temperature, R_H vs. $\frac{I}{T}$, and μ vs. T plots for n and p type OSD bismuth telluride alloys are respectively shown in Figures 54, 46, 47 and 48.

It is noted Z_{max} occurs at $\sim 300^{o}K$ and has a value in these specimens of $2.85\text{x}10^{-3}/^{o}C$.

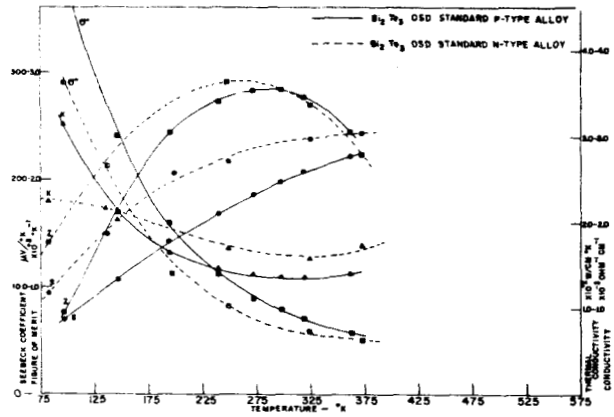

Fig. 54. Z_p, S, k_T, and σ vs temperature for OSD standard n and p type Bi_2Te_3 alloys.

Although these specimens do not represent the highest Z_{max} achieved in Bi_2Te_3 alloys at OSD, they do represent values achievable on a reproducible production basis.

Highest reported and verified values of Z_{max} are $3.1\text{x}10^{-3}/^{o}C$ for p type and $2.9\text{-}3.0\text{x}10^{-3}$ for n type.

$AgSbTe_2$ Alloys

In these state-of-the-art evaluations, the vertical technique of casting silver antimony telluride alloy was adopted.

The elements Ag (99.999%), Sb(99.9999%) and Te (99.9999%), with purity percentages as indicated, were weighed in stoichiometric amounts and sealed in evacuated Vycor tubes. Reaction was carried out at 700°C which was satisfactory for taking the silver into solution. After oscillating charges for 24 hours at this temperature they were cast vertically through a temperature gradient established by two methods and at various speeds. The two methods were 450 kc RF heating and resistance heating. The speeds varied from 3 in to 0.178 in/hr.

$AgSbTe_2$ made in all these ways exhibited two phases (metallographically). $Ag_{19}Sb_{29}Te_{52}$, suggested by Stevenson and Burmeister[54], showed very little second phase. Whereas S and σ vs temperature determined on $AgSbTe_2$ showed a transition at about 125°C, it was not apparent for $Ag_{19}Sb_{29}Te_{52}$. Also the electrical contacts showed a change and internal fracturing of the sample was observed at this temperature for $AgSbTe_2$.

Table 13 shows Z_p, S, k_T, and σ data obtained at room temperature on one specimen of

the $AgSbTe_2$. k_{ph} was calculated from $k_T - k_e$. k_e was determined using the Wiedemann Franz relation. Table 14 shows a comparison of σ, R_H, μ, n, and S at room temperature for $Ag_{19}Sb_{29}Te_{52}$ and $AgSbTe_2$. Note the change from $-R_H$ to $+R_H$ and the large drop in μ_a (the apparent mobility).

TABLE 13

ROOM TEMPERATURE THERMOELECTRIC PARAMETERS FOR OSD $AgSbTe_2$

$Z = 1.25 \times 10^{-3}\ ^{\circ}C^{-1}$

$\rho = 6.94 \times 10^{-3}$ ohm-cm

$S = +239\ \mu V/^{\circ}C$

$k_T = 0.66 \times 10^{-2}$ watts/cm °C (calc)

TABLE 14

ROOM TEMPERATURE CHARGE TRANSPORT AND THERMOELECTRIC DATA ON TWO Ag-Sb-Te ALLOYS

	ρ ohm cm	R_H cm^3/coul	μ_a cm^2/volt sec.	n $(cc)^{-1}$	S μV/°C
$Ag_{19}Sb_{29}Te_{52}$	1×10^{-2}	+0.14	.13	4.4×10^{19}	+220
$AgSbTe_2$	9.6×10^{-3}	-4.87	508	1.2×10^{18}	+235

Figure 55 shows the Z, S, k and σ as a function of temperature. Figure 46 shows the R_H vs $\frac{I}{T}$, Figure 47, the σ vs $\frac{I}{T}$, and Figure 48, μ as a function of temperature for another sample of $AgSbTe_2$ (with lower Z) from these cast rods. The anomalous negative R_H and positive thermoelectric power are noted. These data are discussed later in the alloy modification research section.

Fleischmann's [12] data on Z_p for $(AgSbTe_2)_{0.4}(PbTe)_{0.2}$ are represented in Figure 1 as the maximum achieved to date in this system. He indicated obtaining $Z = 3 \times 10^{-3}/^{\circ}K$ at 500-600°K. Attempts to reproduce this state-of-the-art level mark were made using the vertical technique described previously. Fleischmann [12] used a horizontal technique with multiple zone passes and he extracted a reportedly single phase specimen from the center of the resultant ingot.

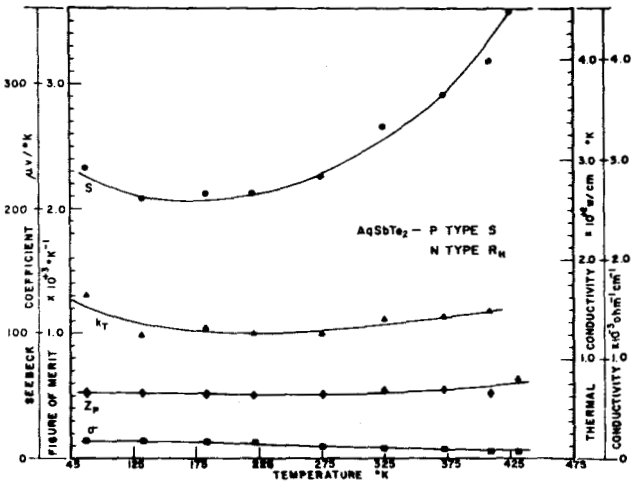

Fig. 55. Z_p, S k_T, and σ vs temperature for OSD $AgSbTe_2$.

Our data at room temperature on this alloy are summarized in Table 15 where they are compared to Fleischmann's [12] values. Our specimens appeared structurally identical to his except a slight second phase was apparent which may account for the differences in Z_p, S, k_T and σ values indicated in Table 15.

TABLE 15

ELECTRICAL PROPERTIES OF $(AgSbTe_2)_{0.4}(PbTe)_{0.2}$ AT 300°K

Properties	Literature Values (from Charts) [16]	Observed Values: Independent measurements	Observed Values: Harman Z-Meter measurements
Resistivity, ρ (ohm-cm)	1.26×10^{-2}	1.90×10^{-2}	1.83×10^{-2}
Seebeck Coeff, S (μ V/°K)	350	278 (∥)	232
S-Meter		280-310 (∥)	280-310 (∥)
		340-360 (⊥)	340-360 (⊥)
Thermal Conductivity, k (watts/cm. °K)	0.55×10^{-2}	0.62×10^{-2}	0.55×10^{-2} (calculated)
Figure-of-Merit, Z $^{\circ}K^{-1}$	1.76×10^{-3}	0.66×10^{-3} (∥) 1.10×10^{-3} (⊥) (calculated)	0.53×10^{-3}

where (∥) = measurement parallel to growth axis
(⊥) = measurement perpendicular to growth axis

At this point we recognized the nature of the material preparation and control problems presented by this $(AgSbTe_2)_{.4}(PbTe)_{.2}$ alloy, as well as its structural instability and concluded it would be desirable to find an improved alloy in this system. Therefore, further optimization attempts were not conducted.

Discussion

A comparison of the Z_p values vs temperature with optimized or maximum Z values reported in the literature, for the state-of-the-art investigation phase of the project effort is presented in Figure 56.

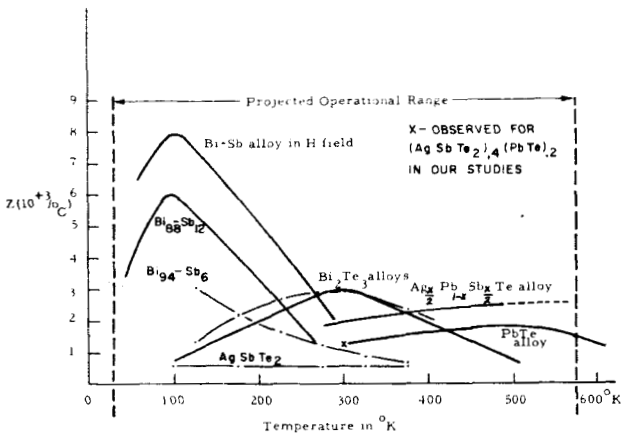

Fig. 56. Comparison of Z_p values vs temperature for OSD $Bi_{94}Sb_6$ crystals (zero H field), n and p type Bi_2Te_3 alloys, and $AgSbTe_2$ with maximum Z_p values revealed in the literature for $Bi_{88}Sb_{12}$ crystals, n and p type Bi_2Te_3 alloys, $(AgSbTe_2)_{0.4}(PbTe)_{0.2}$ and p type PbTe alloys.

The BiSb, Bi_2Te_3, and $AgSbTe_2$ alloys were characterized as summarized in Tables 1, 2, and 3, with the insertion of the electrical and thermoelectric data presented above.

These efforts effectively provided the basic material preparation and evaluation methods for the alloy modification interdisciplinary study which was then initiated.

ALLOY MODIFICATION STUDIES

Introduction

Subsequent to the state-of-the-art investigations, the alloy modification studies essentially developed into:

1. Efforts to devise a more satisfactory crystal growth technique for Bi alloys and initiating attempts to alloy Bi with selected elements other than Sb.

2. Attempting to determine how Fe, Tl, and Au substitutions in the $AgSbTe_2$ compound influenced the thermoelectric, transport and structural properties of this compound using the principles, correlations, and IMWM which evolved from the interdisciplinary theoretical and analytical identification study.

Approximately 100 N-M-X alloy variations were made during this phase of the program. Many of these were made by the Quench-Anneal process (see section on Methods of Material Preparation) which was not considered satisfactory for optimization of the D^5_{3d}-R-$_{3m}$ structure and modifications thereof in which p orbital half bonds and resonance bonds dominate the chemical bonding, and molecular net structures are basic building blocks. As discussed previously, this process consisted of direct reaction of the elements, in a controlled vapor pressure environment (commonly carried out at 550-750°C) quenching to room temperature and annealing for 24 hours at a temperature about 50°C below the melting point. This process is however faster than casting but it yielded specimens with somewhat questionable charge carrier mobility values. On the other hand its adaptability to alloys with unknown melting points was decidedly advantageous in these exploratory efforts.

Each alloy, screened by this process, assisted by metallographic visual observation and R. T. and L. A. T. R_H, σ, and S check tests, which was considered of interest, was then remade using the more compatible vertical casting process. Much of the exploratory data which were gathered will not be discussed here. The reader is referred to the quarterly progress reports for such detailed data.

Sample alloys which were selected through the exploratory evaluation tests were subjected to Z_p, S, k_T, σ, R_H, μ vs. temperature measurements, and in especially interesting cases, to X-ray structure identification.

The experimental work can best be presented in a logical relationship to the postulates and predictions of the theoretical and analytical identification sections of this report.

N-M-X Alloy Research

The D^5_{3d}-R-$_{3m}$ structure, p-orbital half bonds, molecular nets, resonance between molecular units, multiple independent "wells", as defined in the identification section, and some unknown anisotropy of lattice spacings, were all assumed as basically characterizing any experimental alloy of interest. The experimental alloys were evaluated from the view-points of did they

deviate from these assumed characteristics and if so, how. This basic research posture was assumed since the complexities of the structures sought are so great and Z_{max} is expected to be so very sensitive to minor variations in alloy constituents that any empirical metallurgical or chemical approaches would miss the mark.

Since our IMWM tells us an improved alloy can be expected to be characterized by a superstructure, with large lattice parameters and a crystal structure with more complexity than D^5_{3d}-R-$_{3m}$, but still maintaining the basic molecular nature of the C_{33} structure type, detailed structure identifications of promising material systems are important. However they also are time consuming.

More basically we postulate according to our IMWM that the character of the "wells" is of vital importance. Essentially in the studies possible during this period we have attempted to examine how the band structure associated with the "wells" is affected by substitutions into the N-M-X alloy system.

$AgSbTe_2$

For this purpose the $AgSbTe_2$ structure was considered. Figure 57 shows an approximation of its distorted NaCl[55] structure. In Figure 58, a two dimensional molecular net, roughly representing the distorted molecular form of the structure, is shown.

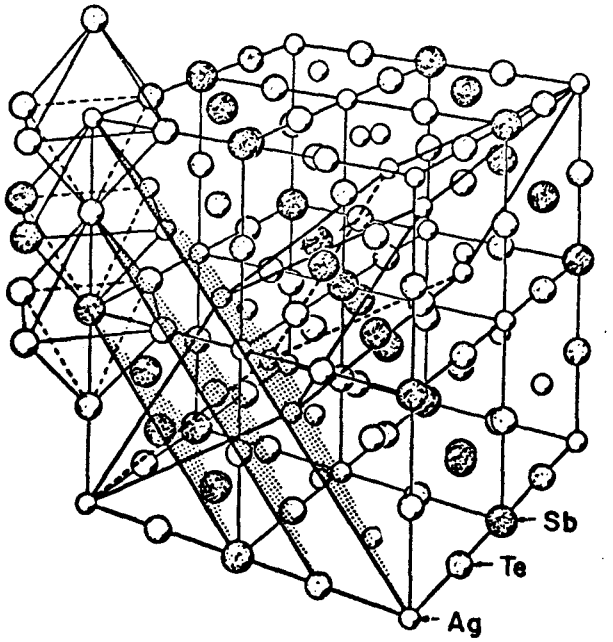

Fig. 57. Relation between ordered $AgSbTe_2$ rhombohedral (idealized) and cubic lattice of the disordered NaCl structure.

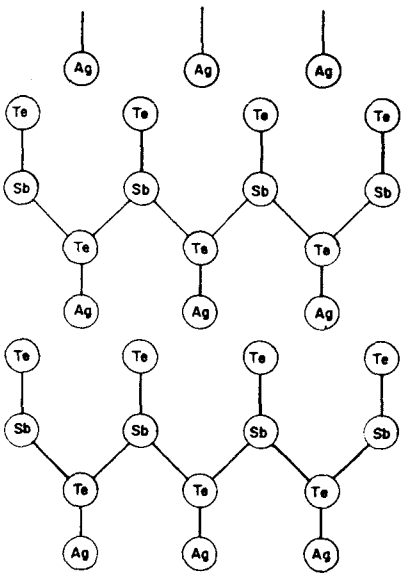

Fig. 58. Pictorial representation of a possible molecular net structure for $AgSbTe_2$ crystals.

Ag in this structure is postulated to be covalently and single S electron bonded. According to the assumed molecular net, (see Figure 58), Ag terminates a partially complete molecular net and sits interstitially in the resonance bonded portion of the structure. Because of the Ag lone s bond, and owing to Ag's low internal pressure and sublimation enthalpy, it is expected that the Te_{II}-Te_{II} resonance bonds primarily hold the structure together. This is consistent with the fact that its melting point is about the same as that of Bi_2Te_3.

The reduction in number of bonds (two half bonds for Ag and 6 for Bi) obviously interrupts phonon conduction and it is assumed this is largely responsible for the k_{ph} = .0046 watts/cm°C, while in Bi_2Te_3, k_{ph} = .01 watts/cm°C. The alternate hexagonal structure for the rhombohedral cell one can assume for $AgSbTe_2$ has a_{hex} = 4.3-4.4 and c_{hex} = 19-20 A°. We note the a_{hex} distance is very close to that in Bi_2Te_3 (4.37A°).

In terms of the molecular well model, it appears at least three of the "wells" of the Bi_2Te_3 structure could be present and contributing to hole conduction. In addition the Ag atom with its first ionization potential of 7.53 ev vs. 8.5 ev for Sb, because of its assumed s half bond, provides at least another well. However because the ionization potential of Ag is lower, it is expected that the valence band due to Ag bonds in this resonance bonded structure may be above that for the Te_{II}-Sb-Te_I wells and therefore it could control conduction.

It is reasonable to assume that the conduction and valence band associated with the Ag "well" will overlap, but because of large atomic ionicity, λ_o, mobility in the conduction band will be much larger than in the valence band. We expect this "well" acts basically like those in BiSb alloys (slight band gap or overlap).

If the Fermi level of these two bands is coincident with the top of the overlapping 3 Te_{II}-Sb-Te_{I} independent valence bands, one could obtain a situation in which the number of electrons in the conduction bands is less than the holes in the valence bands, but the $\frac{\mu_e}{\mu_p}$ would be very large. These assumptions allow rationalizing the $-R_H$ and +S, the measured n/cc = 1.2×10^{18}/cc and electron mobility of ~ 500 cm^2/volt sec (see Figures 59, 60, and 61 observed for this material). These data suggest the action of only one "well" but the high S value, being positive, must be a result of the simultaneous hole conduction by very low mobility, high effective mass holes characteristic of the other molecular wells.

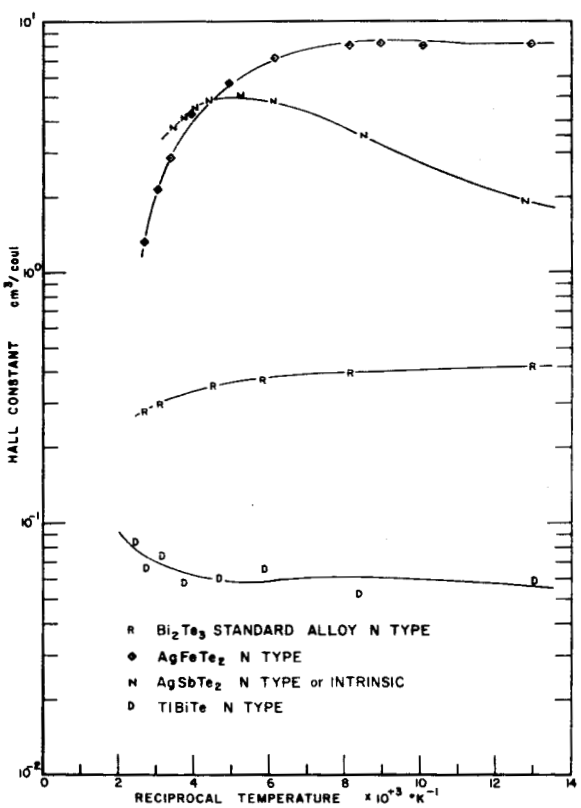

Fig. 59. R_H vs $\frac{1}{T}$ for $AgSbTe_2$, $AgFeTe_2$ and TlBiTe compared to OSD standard n type Bi_2Te_3 alloy.

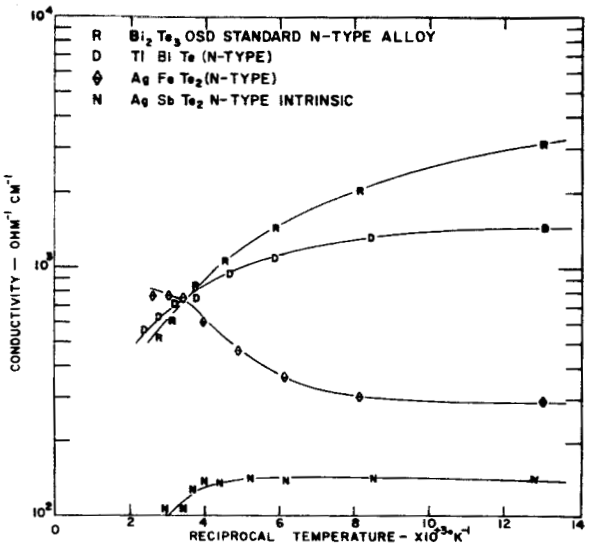

Fig. 60. σ vs $\frac{1}{T}$ for $AgSbTe_2$, $AgFeTe_2$ and TlBiTe compared to OSD standatd n type Bi_2Te_3 alloy.

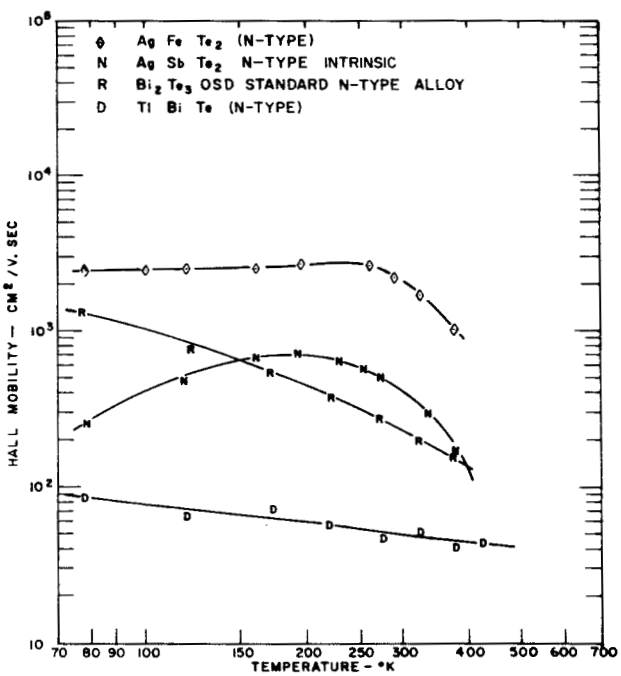

Fig. 61. μ vs T for $AgSbTe_2$, $AgFeTe_2$, and TlBiTe compared to OSD standard n type Bi_2Te_3 alloy.

The data on $Ag_{19}Sb_{29}Te_{52}$ shown in Table 14 indicate the holes dominate conduction.

To interpret these data correctly, one

should probably apply

$$R_H = \frac{n_e \mu_e^2 - n_p \mu_p^2}{(n_e \mu_e + n_p \mu_p)^2} \qquad 54)$$

to obtain the mobilities. These data, however, suggest large $\frac{\mu_e}{\mu_p}$ but a larger concentration of holes than electrons.

On the other hand, it must be recognized that the presence of an Ag_2Te phase and an $Ag_{19}Sb_{29}Te_{52}$ phase could be treated by a double band model to explain the data.

The nature of our specimens were not such that a conclusive assignment of a single phase or two phase treatment was possible.

In Figure 62 we note the constant value of $Z \cong 0.6 \times 10^{-3}/^{\circ}C$ from $75^{\circ}K$ to $300^{\circ}K$ with a tendency to increase at a higher temperature. This is remarkable and a cause for continuing scientific interest in this material.

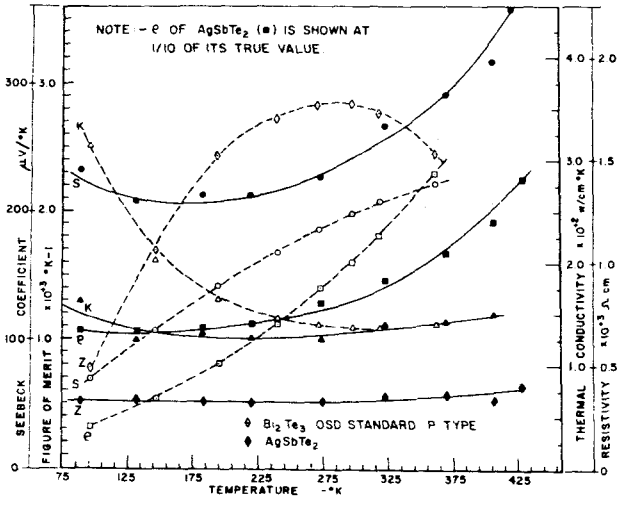

Fig. 62. Z_p, S, k_T and ρ vs temperature for $AgSbTe_2$ compared to standard p type Bi_2Te_3 alloy.

Because of the low k_T (see Table 15), not reflected in our data in Figure 62, it is not necessary that the large number of wells characterizing Bi_2Te_3 alloys be active in this material to obtain a reasonable high Z_p at R. T.

However any increase in the number of wells without increasing k_{ph}, (if possible) would be expected to yield a superior Z_p material. The chances of increasing the number of wells without increasing k_{ph} appear reasonably good despite the expected correlation between lattice phonon conduction and the number of single electron bonds.

The $(AgSbTe_2)_4(PbTe)_2$ alloy is believed to be representative of such an increase in number of wells.

$TlSbTe_2$

Because of the excessively weak bonding in $AgSbTe_2$, and the large atomic ionicity characterizing the Ag-Te bond, the desirability of replacing Ag with a heavier atom characterized by greater polarizibility led to the incorporation of Tl in the Ag position in the $AgSbTe_2$ structure.

Tl, because of being an "inert pair" element and because it is able to exhibit both a one and three valence, was a logical choice. On the assumption that it might half bond with its one p-orbital, an alloy series, $Ag_{1-x}Tl_xSbTe_2$, and several other versions, were prepared to test for its ability to act as Tl^{3+}.

Table 16 summarizes the exploratory data from this series.

TABLE 16

EXPLORATORY EVALUATIONS OF $Ag_{1-x}Tl_xSbTe_2$ ALLOYS

No.	Composition System: $Ag_{1-x}Tl_xSbTe_2$	°K	ρ x10³ ohm·cm	μ cm²/v-sec	R cm³/coul	n x10⁻¹⁸ cm⁻³	S μV/°C	Remarks
68	$AgSbTe_2$	300	9.59	508	-4.87	1.28	+235	Air Quenched annealed 24 hrs. @ 500° C
		78	7.99	178	-1.42	4.40		
80	$Ag\ Tl\ Sb\ Te_2$ 0.9 0.1	300	90.2	11	+0.99	6.31	+360	ditto
		78	250	23	+5.75	1.09		
81	$Ag\ Tl\ Sb\ Te_2$ 0.8 0.2	300	13.5	167	+2.25	2.78	+170	Air Quenched annealed 24 hr. @ 450°C
		78	9.52	323	+3.07	2.04		
82	$Ag\ Tl\ SbTe_2$ 0.6 0.4	300	2.18	273	+0.60	10.4	+76	ditto
		78	0.94	471	+0.44	14.2		
83	$Tl\ Sb\ Te_2$	300	0.96	562	+0.54	11.6	+72	ditto
		78	0.24	1380	+0.32	19.5		

Table 17 summarizes data on an associated $TlSbTe_x$ series where x varied from 0 to 3. The other series, wherein Tl was substituted for Sb, revealed $n = 10^{20}$/cc and will not be discussed here.

At first it was considered that Tl was acting with a 1^+ valence in Ag positions. However X-ray structure identification revealed a D_{3d}^5-$R\bar{3}m$ structure of the C_{33} structure type. This suggested it was apparently being incorporated in a Sb_2Te_3 molecular lattice.

TABLE 17

Evaluations of $TlSbTe_x$ System Processed by Quench-Anneal Process

for x = 1 to 3

No.	Composition System: $TlSbTe_x$	°K	$\rho \times 10^3$ ohm-cm	μ cm²/v-sec	R cm³/coul.	$n \times 10^{-18}$ cm⁻³	S μV/°C	Remarks
OSD 1259	$TlSbTe$	300	1.15	211	0.24	25.7	100	Air Quenched Annealed 24 hrs at 370°C
		78	.25	1160	0.29	21.7		
OSD 1233	$TlSbTe_{1.5}$	300	1.00	483	0.48	13.0	85	at 385°C
		78	0.21	2320	0.49	12.8		
OSD 1232	$TlSbTe_{1.625}$	300	1.11	583	0.65	9.6	70	at 385°C
		78	0.24	2560	0.61	10.2		
OSD 1231	$TlSbTe_{1.75}$	300	1.72	412	0.71	8.8	85	at 425°C
		78	0.43	1180	0.50	12.5		
83	$TlSbTe_2$	300	0.96	562	0.54	11.6	72	at 450°C
		78	0.24	1380	0.32	19.5		
OSD 1222	$TlSbTe_{2.25}$	300	0.66	287	0.19	32.9	80	at 430°C
		78	0.20	502	0.10	62.5		
OSD 1223	$TlSbTe_{2.50}$	300	0.82	226	0.18	34.7	80	at 440°C
		78	0.27	682	0.18	34.7		
OSD 1224	$TlSbTe_{2.75}$	300	1.11	158	0.18	34.7	80 to 90	at 440°C
		78	0.51	445	0.23	27.2		
OSD 1212	$TlSbTe_3$	300	1.03	223	0.23	27.2	80 to 100	at 375°C
		78	0.42	876	0.37	17.1		

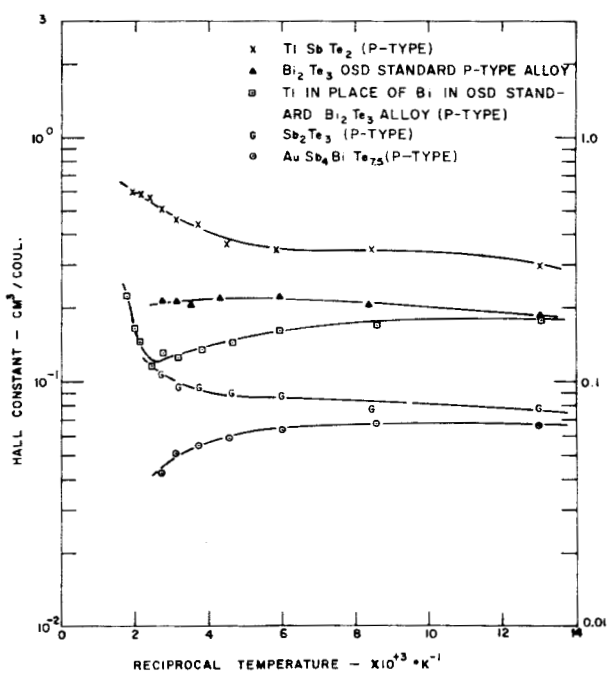

Fig. 63. R_H vs $\frac{1}{T}$ for $TlSbTe_2$, Tl in place of Bi in p type Bi_2Te_3 standard alloy, Sb_2Te_3, and $AuSb_4BiTe_{7.5}$ compared to OSD standard p type Bi_2Te_3 alloy.

R_H, σ, and μ vs. temperature data shown in Figures 63, 64 and 65 and compared to that for a p type standard Bi_2Te_3 alloy confirmed that the transport properties were practically identical (at low temperatures) with those of our optimized standard p type Bi_2Te_3 alloy.

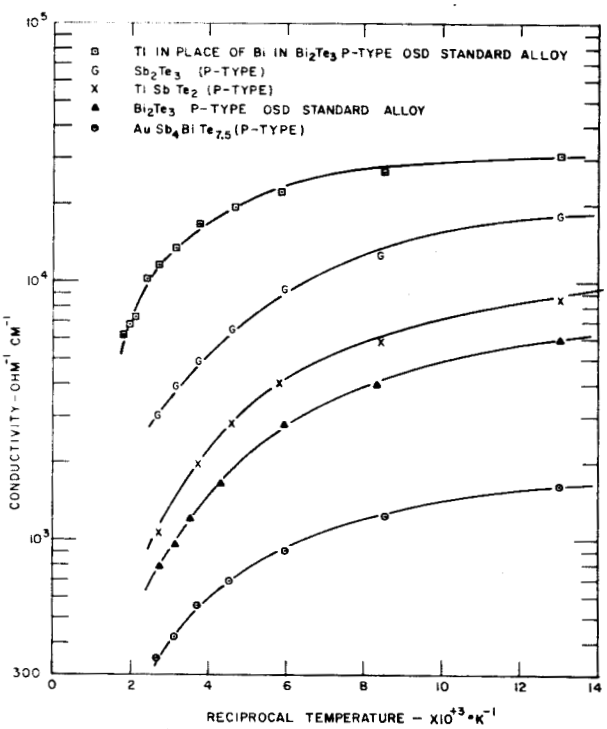

Fig. 64. σ vs $\frac{1}{T}$ for $TlSbTe_2$, Tl in place of Bi in p type Bi_2Te_3 standard alloy, Sb_2Te_3, and $AuSb_4BiTe_{7.5}$ compared to OSD standard p type Bi_2Te_3 alloy.

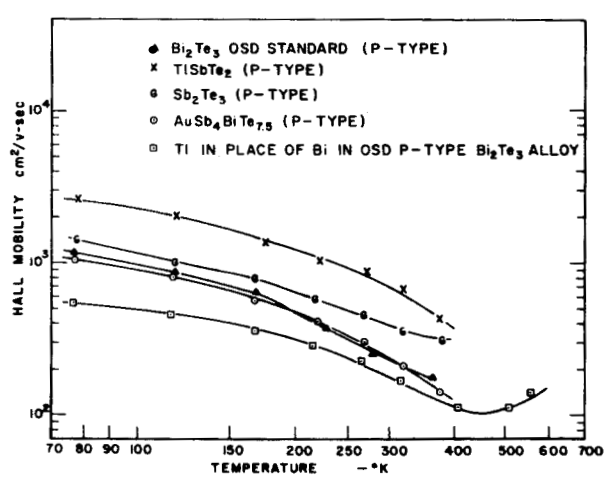

Fig. 65. μ vs T for $TlSbTe_2$, Tl in place of Bi in p type Bi_2Te_3 standard alloy, Sb_2Te_3, and $AuSb_4BiTe_{7.5}$ compared to OSD standard p type Bi_2Te_3 alloy.

However Z_p, S, k_T and σ data shown in Figure 66 and the S data in Tables 16 and 17 revealed that S was strongly suppressed. Preliminary interpretation of the data suggested degeneracy of the charge carriers owing to reduction in the number of active wells.

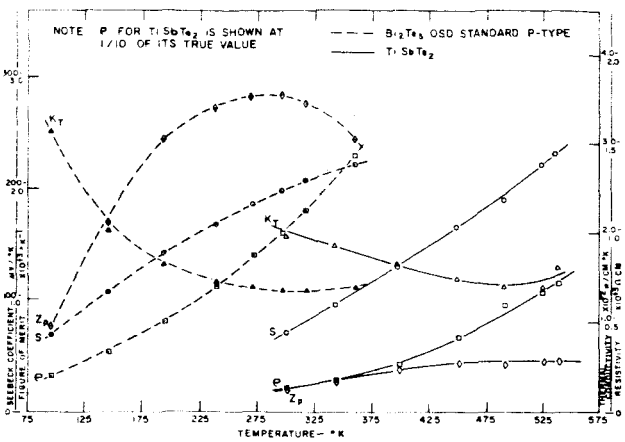

Fig. 66. Z_p, S, k_T and ρ vs temperature for $TlSbTe_2$ compared to OSD standard p type Bi_2Te_3 alloy.

The high temperature end of the Z, S, k, and σ, R_H and μ vs. temperature curves revealed a new phenomenon, reminiscent of that observed in SnTe, by Brebrick and Strauss[56], Allagaier and Sheie[57], and Sagar and Miller[58] and also in p-PbTe, n-GaAs and n-GaSb. The Hall constant increased rapidly with rising temperature.

Experiments on Anomalous Effects of Tl

At this point we assumed that perhaps Tl was sitting in an Sb position in the molecular lattice without disrupting resonance bonding nor the C_{33} structure (confirmed by X-ray identification later). We assumed Tl was bonding with 1 p-orbital half bond and because its non bonding s orbitals in this high dielectric constant medium were separated by a very small gap from the top of the valence bands, they could be thermally excited to fill the p-orbitals. When thermally excited they would fill the excess hole states which the Tl introduced into the valence band structure and subsequently the Tl cations would act as ionized impurity centers.

To confirm these hypotheses, two experiments were conducted. Tl was substituted into our standard p-type Bi_2Te_3 alloy in place of the Bi. Since this would be expected to change the anisotropy of the Te_{II}-(BiSb) and (BiSb)-Te_I lattice spacings, it was expected that the structure would act now like a modified Sb_2Te_3 alloy. Therefore Sb_2Te_3 was made by the same processing technique.

In Figures 67, 64, 63 and 65, the Z_p, S, k_T, σ, R_H, and μ versus temperature curves for the standard p-type Bi_2Te_3 alloy with Tl substitution are shown. In figures 68, 64, 63 and 65 the Z, S, k, σ, R_H, and μ versus temperature curves for the Sb_2Te_3 are shown. X-ray structure data revealed both specimens had the C_{33} structure characteristic of the high Z alloy.

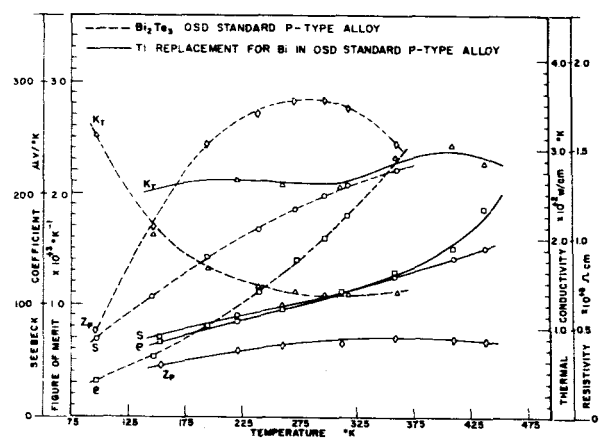

Fig. 67. Z_p, S, k_T, and ρ vs temperature for Tl substitution for Bi in p type Bi_2Te_3 standard alloy compared to p type standard Bi_2Te_3 alloy.

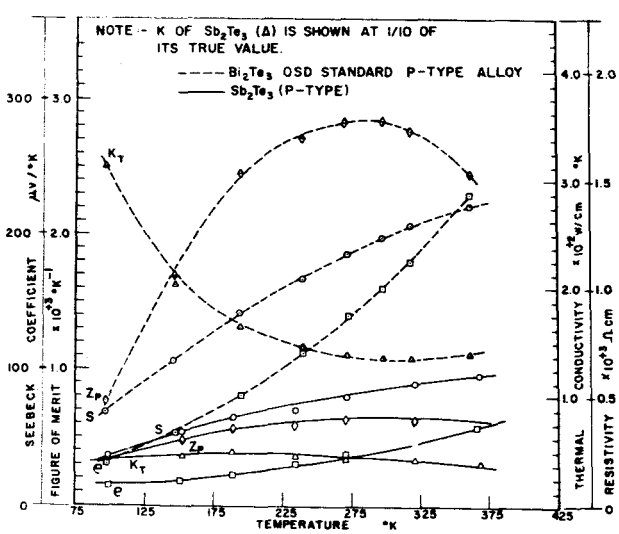

Fig. 68. Z_p, S, k_T, and ρ vs temperature for Sb_2Te_3 compared to standard p type Bi_2Te_3 alloy.

Examining these curves reveals:

1. Tl in the standard alloys results in the same drastic reduction in Z as observed for $TlSbTe_2$ (See Figure 67). Note, Z_{max} occurs at higher temperature and has a value of about $0.65 \times 10^{-3}/^{\circ}C$.

2. The R_H vs $\frac{1}{T}$ curve (See Figure 63) shows a very sharp increase in value with increasing temperature.

3. The μ vs. temperature (See Figure 65) shows an actual reversal in trend to a positive dependence of μ on temperature.

4. Compared to the standard p-type alloy at R. T., σ is increased and S decreased by a factor of about 2, suggesting degeneracy of the hole distribution has been introduced due to introduction of new hole states in the valence band and/ or decrease in lattice anisotropy and consequent decrease in E_g of the "wells".

5. The Z_p, S, k_T, σ, R_H, and μ vs. temperature data for Sb_2Te_3 are related to the similar data for the Tl in the standard p-type alloy. The anomalous μ vs. T trend for the Tl in standard p-type alloy appears asymptotic to the μ vs. temperature trend for Sb_2Te_3 at higher temperatures. The Z_p vs. temperature trend is closely similar to that for the Tl in standard p-type alloy.

The results of these experiments support the assumption that the increasing R_H with temperature is caused by Tl non bonding s orbitals being thermally excited into the empty p-orbital bonds thus reducing the number of hole states. The anomalous positive temperature coefficient of μ is due to the superposition of self developed ionized impurity scattering on the $\mu \alpha T^{-\frac{3}{2}}$ accoustic scattering.

In addition, it is postulated more anharmonicity of the lattice bonding forces characterizes this structure than the p-type Bi_2Te_3 alloy and effects resulting from this condition may also be present.

The similar Z_p values and also the rising R_H with temperature for Sb_2Te_3 also suggest that some excitation of the Sb nonbonding s-orbitals may also be occurring to reduce the number of hole states in the valence band.

In summary, these data confirmed the self ionized impurity scattering proposal, justified the empty orbital concept for accounting for the increased number of hole states in the valence band, and substantiated that the E_g of the "wells" has indeed been decreased by a radical change in anisotropy of lattice spacings for Te_{II}-(SbTl) and (SbTl)-Te_I from that for Te_{II}-(BiSb)-Te_I. It seems reasonable in view of these changes that the number of active wells in these structures may be the same as in Bi_2Te_3 high Z alloys.

Au Substitution in $AgSbTe_2$ and $BiSb_4Te_{7.5}$

Since Au is heavier than Ag, and has a higher electronegativity[5] than either Sb or Te, additions of Au to the D_{3d}-R-$_{3m}$ system and substitutions of Au in $AgSbTe_2$ were not expected to bond in the structures.

However since compatible second phases can be expected to be tolerated on cleavage planes, the effect of Au in small quantities was considered of interest. Of the three (Cu, Ag and Au), Au would be expected to be least mobile owing to size.

In Tables 18 and 19 the exploratory data on Au substitutions in the $AgSbTe_2$ lattice and as an addition to $Sb_4BiTe_{7.5}$ are shown. In very small quantities, less than $x = .05$ in $Ag_{1-x}Au_xSbTe_2$, and $x = 1$ in $Au_xSb_4BiTe_{7.5}$, it appears Au is not harmful to the S and σ, but it is to k_T, and therefore, Z.

TABLE 18

Exploratory Evaluations of $Ag_{1-x}Au_xSbTe_2$ Alloys

No.	Composition System: $Ag_{1-x}Au_xSbTe_2$	°K	$\rho \times 10^3$ ohm-cm	μ cm²/volt-sec	R cm³/coul.	$n \times 10^{-18}$ cm⁻³	S μV/°C	Remarks
105	$Ag_{0.9}Au_{0.1}SbTe_2$	300	6.11	1.85	+0.011	553	+205	Air Quenched Annealed 24 hrs at 500°C
		78	4.40	2.6	+0.011	548	——	
106	$Ag_{0.8}Au_{0.2}SbTe_2$	300	0.618	48	+0.03	210	+38	ditto
		78	0.193	138	+0.027	235	——	
107	$Ag_{0.6}Au_{0.4}SbTe_2$	300	0.376	47	+0.018	353	+24	ditto
		78	0.129	156	+0.02	311	——	
108	$AuSbTe_2$	300	0.188	77	+0.015	431	+34	ditto
		78	0.068	427	+0.029	216	——	
105 R	$Ag_{0.9}Au_{0.1}SbTe_2$ Reprocessed	300	7.05	16	+0.11	56.8	+100 to +170	Heated by RF 40 hrs. Air Quenched-Annealed 24 hr. at 500°C
		78	3.21	44	+0.14	44.6	——	
106 R	$Ag_{0.8}Au_{0.2}SbTe_2$ Reprocessed	300	1.07	40	+0.04	146	+50	Heated by RF 94 hr. Air Quenched-Annealed 24 hr at 500°C
		78	0.44	36	+0.016	393	——	
107 R	$Ag_{0.6}Au_{0.4}SbTe_2$ Reprocessed	300	0.24	78	+0.019	334	+26	Heated by RF 72 hrs-Zone leveled
		78	0.085	218	+0.019	334	——	
108 R	$AuSbTe_2$ Reprocessed	300	0.092	119	+0.011	573	+24	Heated by RF 37 hrs.-Zone leveled
		78	0.034	423	+0.015	428	——	

TABLE 19

Exploratory Evaluations of $Au_xSb_4BiTe_{7.5}$ Alloys

No.	COMPOSITION System: $Au_xSb_4BiTe_{7.5}$	°K	$\rho \times 10^3$ ohm-cm	μ $cm^2/V\text{-}sec$	R $cm^3/coul.$	$n \times 10^{-18}$ cm^{-3}	S $\mu V/°C$	REMARKS
1243	$Sb_4BiTe_{7.5}$	300	0.334	222	+0.074	84.4	+120	R.F. Cast at 0.5°/hr.
		78	0.0819	1220	+0.10	62.5		
1245	$Au_{0.2}Sb_4BiTe_{7.5}$	300	0.334	225	+0.075	83.3	+125	ditto
		78	0.0858	769	+0.066	94.7		
1246	$Au_{0.3}Sb_4BiTe_{7.5}$	300	0.261	215	+0.056	112	+140	ditto
		78	0.0605	926	+0.056	112		
1247	$Au_{0.5}Sb_4BiTe_{7.5}$	300	0.220	214	+0.047	133	+140	ditto
		78	0.0574	976	+0.056	112		
1227	$Au\ Sb_4BiTe_{7.5}$	300	0.269	245	+0.066	94.7	+140	ditto
		78	0.067	992	+0.066	94.7		

In Figures 69, 64, 63 and 65, the Z_p, S, k_T, σ, R_H, and μ vs temperature for $AuSb_xBiTe_{7.5}$ are shown. We note $Z \cong 0.9 \times 10^{-3}$ at near room temperature. k_T is increased somewhat above that observed for $Sb_4BiTe_{7.5}$.

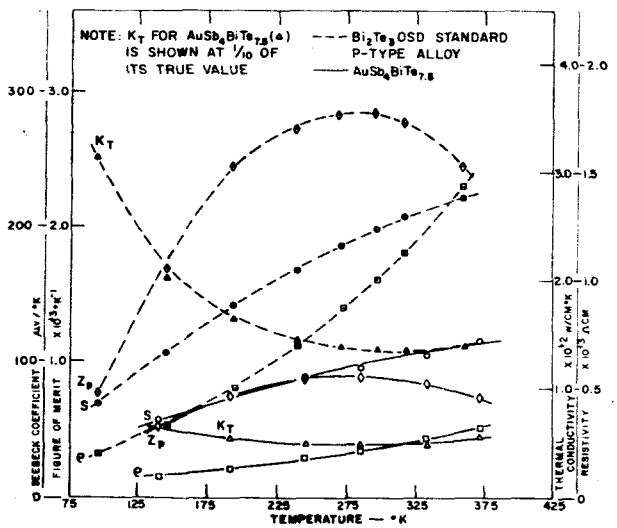

Fig. 69. Z_p, S, k_T and ρ vs temperature for $AuSb_4BiTe_{7.5}$ compared to standard p type Bi_2Te_3 alloy.

Fe Substitution in $AgSbTe_2$

The closely similar electronegativity of Fe to that of Sb, the challenge of exploring effects of d orbitals, the low internal pressure and sublimation enthalpy of Fe and its known effect in Ag_2Te of anomalously increasing mobility[53] led to exploring Fe as a means of decreasing the resistivity of $AgSbTe_2$, and thus providing a possible way of developing an n-type higher temperature thermoelectric cooling material.

A series of alloys were made represented by $AgFe_xSb_{1-x}Te_2$. The exploratory results are shown in Table 20. As expected according to IMWM this alloy persisted in showing an n-type R_H and p-type high S even at x = .2. The $AgFeTe_2$ alloy properties, compared to those given by Wernick and Wolfe[53]; are shown in Table 21.

TABLE 20

EXPLORATORY EVALUATIONS OF $AgSb_{1-x}Fe_xTe_2$ ALLOYS

No.	COMPOSITION System: $AgSb_{1-x}Fe_xTe_2$	°K	$\rho \times 10^3$ ohm-cm	μ $cm^2/V\text{-}sec$	R $cm^3/coul.$	$n \times 10^{-18}$ cm^{-3}	S $\mu V/°C$	REMARKS
68	$AgSbTe_2$	300	9.59	508	-4.87	1.28	+235	Air Quenched annealed 24 hrs. at 500°C
		78	7.99	178	-1.42	4.40		
69	$AgSb_{0.95}Fe_{0.05}Te_2$	300	6.58	582	-3.84	1.63	+190	ditto
		78	5.50	296	-1.63	3.83		
70	$AgSb_{0.9}Fe_{0.1}Te_2$	300	6.78	411	-2.79	2.24	+200	ditto
		78	5.90	102	-0.60	10.4		
72	$AgSb_{0.8}Fe_{0.2}Te_2$	300	6.44	424	-2.73	2.29	+170	ditto
		78	7.44	126	-0.94	6.65		
73	$AgSb_{0.6}Fe_{0.4}Te_2$	300	4.50	772	-3.47	1.80	+100	ditto
		78	7.36	168	-1.24	5.04		
75	$AgFeTe_2$	300	1.73	772	-3.75	1.67	-65	ditto
		78	10.6	2170	-22.4	0.28		

TABLE 21

ELECTRICAL PROPERTIES OF SILVER IRON TELLURIDE

Properties	Measured Values		Literature Values[53]	
	293 °K	77 °K	293 °K	77 °K
Resistivity, ρ (ohm-cm)	1.15×10^{-3}	3.24×10^{-3}	1.8×10^{-3}	10.4×10^{-3}
Hall Coeff., R (cm^3/coul.)	-3.2	-10.9	-3.6	-0.5
Hall Mobility, R/ρ (cm^2/V.sec)	2,790	3,360	2,000	810 (?)
Seebeck Coeff, S (μV/°K)	-51	-----	-70	-------

In Figures 70, 60, 59, and 61 the Z_p, S, k_T, σ, R_H and μ vs. temperature trends are shown for $AgFeTe_2$. We note the Z_p value is very low. However, the confirmation of high electron mobility in this material is noteworthy.

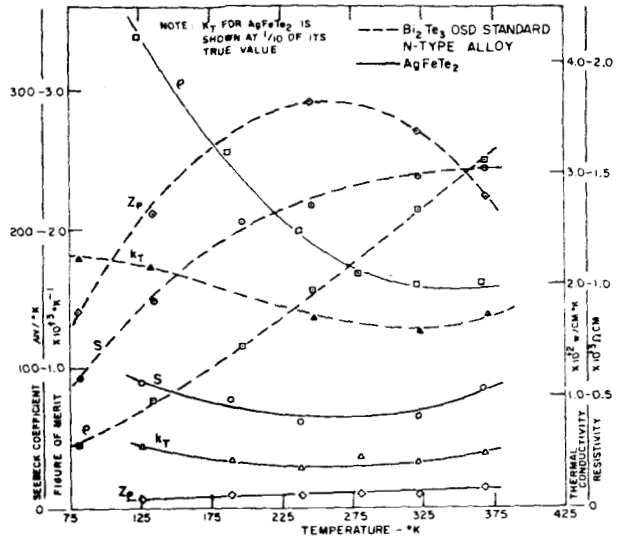

Fig. 70. Z_p, S, k_T, and ρ vs temperature for $AgFeTe_2$ compared to standard n type Bi_2Te_3 alloy.

No identification was made of its structure. However Shtrum[60] substantiated that its structure is one of considerable complexity. Zaslowskii and Zhukova[60] showed that it has a trigonal lattice and an interesting superstructure. Its structure resembles NiAs in the first approximation.

TlBiTe

Since $Ag_{1-x}Fe_xSbTe_2$ alloys seemed to have doubtful promise in seeking an n-type material for higher temperatures, TlBiTe was considered. This material appeared at first to have some possibility. (See Table 22). However X-ray identification showed it to be two phased. No readily identifiable fit of its observed pattern to established X-ray patterns could be found.

TABLE 22

Comparison of Properties of $TlBiTe_x$ Alloys Prepared by Quench-Anneal and R. F. Casting

No.	Composition System: $TlBiTe_x$	°K	$\rho \times 10^3$ ohm·cm	μ $cm^2/volt\text{-}sec$	R $cm^3/coul$	$n \times 10^{-18}$ cm^{-3}	S $\mu V/°C$	Remarks
OSD 1219	TlBiTe	300	1.04	96	-0.10	62.5	-90 to -110	R. F. cast at 0.5"/hr VP → 750°C
		78	.524	120	-0.063	99.2		
OSD 1242	$TlBiTe_2$	300	.745	25	-0.018	340	-52	R. F. cast at 0.5"/hr. VP-750°C
		78	.633	32	-0.021	305		
OSD 1213	$TlBiTe_2$	300	1.26	283	-0.357	17.5	-70	Air Quenched annealed 24 hrs. at 375°C
		78	.783	738	-0.578	10.8		
OSD 1214	$TlBiTe_3$	300	1.37	92	-0.126	49.6	-40	Air Quenched Annealed 24 hrs. at 375°C
		78	.941	390	-0.367	17.0		

In Figures 59, 60, and 61, R_H, σ, and μ versus temperature are shown. Z_p was too low to measure.

DISCUSSIONS AND CONCLUSIONS

The $AgSbTe_2$ alloy modification efforts along with the supporting basic research investigations on this system in conjunction with the progress made in interdisciplinary identification and characterization of the highest Z alloys known for thermoelectric cooling, has considerably clarified the advantages and disadvantages of the D^5_{3d}-R-$_{3m}$ and distorted forms of this structure.

As a result of this work, we now know of 5 ways in which Z_p can be suppressed in D^5_{3d}-R-$_{3m}$ structures:

1. Cause insufficient anisotropy of lattice spacings and difference in bonding energy between Te_{II} and Te_I positions. This results in reduction in E_g and development of degeneracy of the electron or hole distribution at R. T. when the optimum concentration of charge carriers of $n = 10^{19}$/cc is present.

2. Introduce energy bands by alloying atoms which suppress the number of active wells and owing to atomic ionicity strongly maximize $\frac{\mu_e}{\mu_p}$. The latter effect is not undesirable except when coupled with the former one.

3. Introduction of excessive ionicity which destroys resonance bonding by excessive polarization effects. This amounts to elimination of p-orbital half bonds.

4. Add elements which have markedly different ionization potentials compared to those of Bi or Sb.

5. Introduce cations of similar electronegativity but a smaller number of p-orbitals without compensation for the hole states thus introduced in the "wells".

We conclude the experimental data on modifications of the D^5_{3d}-R-$_{3m}$ structures qualitatively and in some cases quantitatively support the IMWM for D^5_{3d}-R-$_{3m}$ p-orbital half bonded, resonance bonded materials.

We conclude p-orbital half bonded rhombohedral structures with optimized resonance bonds are required for high Z_p thermoelectric cooling materials.

These investigations led to recognizing a new method of doping for p-type bismuth telluride, that is the substitution of Tl for Bi or Sb in the D^5_{3d}-R-$_{3m}$ lattice of Bi_2Te_3 or Sb_2Te_3 alloys.

A new D^5_{3d}-R-$_{3m}$, C_{33} structured alloy, namely $TlSbTe_2$, was discovered.

RECOMMENDATIONS

Further study of designed alloys which incorporate (a) p-orbital half bonds, and perhaps s half bonds, (b) exacting controls on anisotropy of lattice spacings, and size and electronegativity of terminating anions for p-orbital half bonded cations, and (c) major proportions of Bi, Sb, and Tl, with or without major amounts of Te and Se, and also with minor amounts of compatible (in the sense defined in this report) elements, are the most promising routes to the goals of this project.

The proper balancing of charge carrier excess and deficiency with due consideration of antistructure development can be expected to increase Z_p at R. T. in the C_{33}, D^5_{3d}-R-$_{3m}$ structure if the number of active "wells" is not reduced in the process.

It is believed that new methods of processing p-orbital half bonded, molecular-net-structured compounds and semimetals are necessary to enable the ultimate maximization of Z_p and Z_{NE} to be achieved. The melt technique suffers from disadvantages, such as antistructure, which might be overcome through new and novel processing methods. The design of new processing methods should strongly reflect consideration of the idiosyncrasies of the molecular habits of the high Z thermoelectric cooling materials. Especially important will be the institution of long time annealing or crystallization treatments to develop the desired complex "multi-welled" molecular crystal structures.

The molecular well model (IMWM) should be developed, if possible, on a more quantitative basis. Characterization of the hole and electron state occupation and excitation rules for the band structure, which arise from the coexistence of the two valence bonds in the "wells", should be a specific objective.

BIBLIOGRAPHY

1). G. E. Smith and R. Wolfe — "Thermoelectric Properties of Bi-Sb Alloys" J. A. P. 33, 841, (1962).

2). G. F. Boesen, A. D. Reich, and E. E. Rufer — "Infrared Cell Electronically Refrigerated", ASD technical Report 61 - 369, Sept. 1961.

3). C. F. Kooi, K. F. Cuff, and R. B. Horst — (Private Communication).

4). T. C. Harman et al, — Appl. Phys. Letters 4, 77 (1964).

5). J. R. Madigan — "A Hybrid Peltier-Ettingshausen Cooler for Cryogenic Temperature" (to be published in Journal of Solid State Electronics).

6). A. F. Ioffe — Semiconductor Thermoelements and Thermoelectric Cooling, Infosearch, London (1957).

7). H. J. Goldsmid — Proc. Phys. Soc. 68, 218 (1955) Brit. Jour. App. Phys. 5, 386, (1954).

8). F. D. Rosi, R. Abeles, and R. Jensen — Jour. of Phys. Chem. Solids, 10, 191, (1959).

9). J. B. Conn, E. J. Sheehan, and R. C. Taylor — Adv. Energy Conv. 1, 119, (1961).

10). R. Wolfe and G. E. Smith — App. Phys. Letters, 1, 5 (1962).

11). J. H. Wernick et al. — J. Phys. Chem. Solids 4, 154 (1958).

12). H. Fleischmann — Z. Naturforshung 16a, 765 (1961).

13) J. H. Dennis — Adv. Energy Conversion 1, 99 (1961).

14). C. J. Smithells — Metals Reference Book p 169, Butterworths (1949).

15). F. Seitz — Modern Theory of Solids, McGraw-Hill, (1940).

16). A. F. Wells — Structural Inorganic Chemistry, Oxford (1945).

17). R. G. Wyckoff — Crystal Structures Interscience, (1948).

18). J. Blakemore — Semiconductor Statistics Pergamon, (1962).

19). H. Krebs — Angewandte Chemie 70, 615, (1958).

20). H. Krebs — Zeitschrift fur Electrochemie 61, 925 (1957).

21). H. Krebs — Acta Crystallographica 9 (part 2), 95 (1956).

22). E. Mooser and W. B. Pearson — Phys. Rev. 101, 1608 (1956).

23). O. G. Folberth — Compound Semiconductors p. 28, Reinhold, (1962).

24). A. E. Middleton, et al. — 2nd Quarterly Progress Report. NAS8-11075, Jan., (1964).

25). J. P. Suchet — J. Phys. Chem. Solids 21, 156, (1961).

26). H. Gatos and A. J. Rosenberg — "The Chemical Approach to Semiconductors" Science Publishers, Inc. p. 196, (1963).

27). A. E. Middleton — 1st Quarterly Progress Report. NAS8-11075, Oct., (1963).

28). E. Mooser — Science 132, 1285 (1960).

29). D. V. Gitsu, G. A. Ivanov, A. M. Popov — Sov. Phys. -Solid State 4, 15, (1962).

30). P. W. Lange — Naturwissenshaften 27, 133 (1939).

31). P. M. Lee and L. Pincherle — Proc. Phys. Soc. 81, 461 (1963).

32). Airapetiants, et al — Soviet Phys. -Tech. Phys. 2, 2009 (1957).

33). J. R. Drabble and R. Wolfe — Proc. Phys. Soc. (London) 69, 1101 (1956).

34). J. R. Drabble, R. D. Groves, and R. Wolfe — Proc. Phys. Soc. (London) 71, 430, (1958).

35). J. R. Drabble — Proc. Phys. Soc. (London) 72, 380 (1958).

36). B. A. Efimova, I. Ya. Korenbilt, and Kovikov — Soviet Phys. - Solid State 3, 2004 (1961).

37). B. A. Efimova, V. I. Novikov, and A. G. Ostroumov — Soviet Phys. - Solid State - 4, 218, (1962).

38). A. L. Jain — Phys. Rev. 114 1518 (1959).

39). G. L. Smith — Phys. Rev. 115 1561 (1959).

40). C. F. Kooi, et al — "Solid State Cryogenics", Final Report A. F. 33 (616) - 8490, ASD-TDR-62-1100, Mar. 1963.

41). S. Fischler — Trans. Met. Soc. AIME 230, 340 (1964).

42). D. M. Brown and F. K. Heumann — J. A. P. 35, 1947 (1964).

43). W. A. Tiller — Thermoelectricity: Science and Engineering p. 181 Interscience 1 1961.

44). G. V. Komarov and A. R. Regel — Soviet Phys. - Solid State 5, 563 (1963).

45) J. J. Gilman — The Art and Science of Growing Crystals John Wiley and Sons, 1963.

46). G. J. Cosgrove, J. P. McHugh and W. A. Tiller — J. A. P. 32 621 (1961)

47). T. M. Dauphinee and E. Mooser — Rev. Sci. Inst. 26 660 (1955)

48). T. C. Harmon, J. H. Cohn, and M. J. Logan — J. A. P. 30 1351 (1959).

49). H. Welker — L'onde Elec. 30, 309 (1950)

50). A. E. Middleton, F. J. Celli, and J. Harpster — 3rd Quarterly progress report, NAS8-11075, Apr. 1964.

51). B. Abeles and S. Meiboom — Phys. Rev. 101, 544 (1956)

52). C. F. Gallo, B. S. Chandrasekhar, and P. H. Sutter — J. A. P. 34, 144 (1963).

53). T. C. Harmon — Adv. Eng. Conv. 3, 667, (1963).

54). R. A. Burmeister and D. A. Stevenson — "Prep and Elect. Properties of Ag-Sb-Te alloys" AIME Tech Conf. Boston, Aug. 1963.

55). S. Geller and J. H. Wernick — Acta Crystallographica 12, 46, (1959).

56). R. F. Brebrick and A. J. Strauss — Phys. Rev. 131, 104, (1963).

57). R. S. Allgaier and P. O. Scheie — Bull Am. Phys. Soc. 6, 436 (1961).

58). A. Sagar and R. C. Miller — Proc. of International Conference on the Physics of Semiconductors, Exeter, 1962.